Cal Poly Supermileage Electric Vehicle Drivetrain and Motor Control Design

Enyi Liang

Chris McLaughlin

Clarisa Howe

Erik Alvarado

Email: cpesmv@gmail.com

Advisors:

John Fabijanic

Art MacCarley

Sponsored by

Cal Poly

Supermileage Vehicle Club

Spring 2018 – Winter 2019

1 Table of Contents

List of Figures

List of Tables

1 Abstract

The Cal Poly Supermileage Vehicle team is a multidisciplinary club that designs and builds high efficiency vehicles to compete internationally at Shell Eco-Marathon (SEM). Cal Poly Supermileage Club has been competing in the internal combustion engine (ICE) category of the competition since 2007. The club has decided it is time to expand their competition goals and enter their first battery electric prototype vehicle. To this end, a yearlong senior design project was presented to this team of engineers giving us the opportunity to design an electric powertrain with a custom motor controller. This system has been integrated into Ventus, the 2017 Supermileage competition car, bringing it back to life as E-Ventus for future competitions.

The scope of this project includes sizing a motor, designing the drivetrain, programing the motor driver, building a custom motor controller, and finally mounting all these components into the chassis. The main considerations in this design are the energy efficiency measured in distance per power used (mi/kWh) and the whole system reliability. Driven train system reliability has been defined as the car starts the first time every time and can complete two competition runs of 6.3 miles each without mechanical or electrical failure. Drivetrain weight target was less than 25 pounds, and the finished system came in at 20 lbs 4 oz. Due to the design difficulties of the custom controller, three iterations were able to be produced by the end of this project, but there will need to be further iterations to complete the controller. Because of these difficulties our sponsor, Will Sirski, and club advisor, Dr. Mello, have agreed that providing the club with a working mechanical powertrain, powertrain data from the club chassis dynamometer using the programmed TI evaluation motor controller board, and providing board layout for the third iteration design for the custom controller satisfy their requirements for this project.

2 Introduction

The team consists of three mechanical engineers and an electrical engineer, Clarisa Howe, Enyi Liang, Chris McLaughlin, and Erik Alvarado, respectively. The project was broken down into four major parts, vehicle dynamics simulation, electric propulsion system control programming, power electronics design, mechanical drivetrain design and manufacture, components integration and lastly testing and verification of our design. Chris McLaughlin was head of vehicle dynamics simulation and dyno testing. He completed analysis and simulation for powertrain and vehicle dynamics, he also led the mechatronics programming for the motor controller. Erik Alvarado was head of the power electronics design, motor controller interfacing and procurements of electronics parts. Clarisa Howe led mechanical system component design and analysis. Her responsibilities included organizing prototyping and overall project scheduling. Enyi Liang led motor selection, manufacturing, components integration, as well as procurements and budgeting. While each team member was responsible for planning their respective areas, each member was supported by the others in design, manufacturing, and integration of the whole system.

To aid with our analysis and components sizing, a MATLAB and Simulink model was developed to simulate the powertrain performance and subcomponent dependencies. The model considers interactions between the battery, motor, drivetrain, wheel, and vehicle dynamics on order to determine the system power efficiency. The results guided the selection of the drivetrain components and motor, in addition to providing insight into how the system should be run to provide the least power draw. From the simulation, a hybrid driving technique of constant operating speed combined with burn and coast was developed.

A motor controller circuit board was developed specifically for brushless direct current (BLDC) motor which used a combination of a single board computer and custom power and driving stages. The PCB design went through three iterations. In each iteration, the board was sent to be professionally printed, parts were soldered on, the board was tested, and the design modified where necessary. Concurrent with designing and building the custom motor controller, an off-the-shelf motor BLDC controller evaluation board was purchased from Texas Instruments (TI) and used for controller software development and testing motor characteristics in the Electrical Engineering department motor dynamometer lab. The evaluation board was also bought to serve as a benchmark of efficiency for our custom-made motor controller.

The BLY343D-3200 BLDC motor from Anaheim Automation was selected based on road load calculations, speed and torque requirements, and rated efficiency points. The BLDC motor allowed the team to use TI BLDC control software, evaluation board, and tutorials to provide a template for building our own software and PCB which reduced the development time of the software.

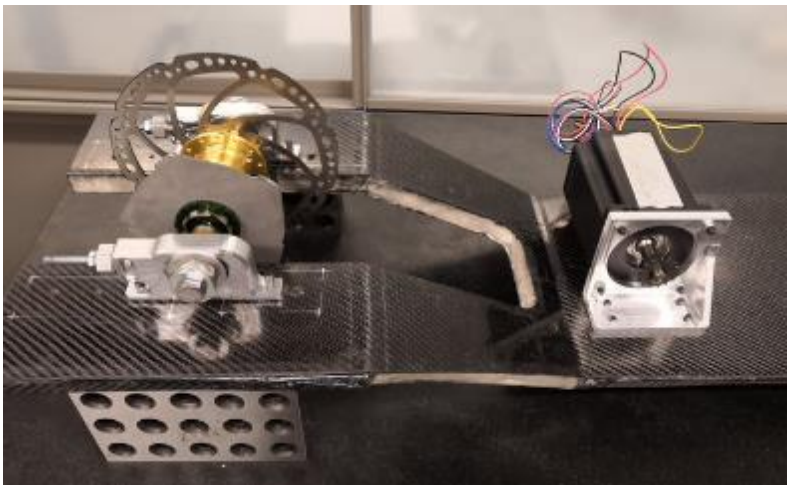

Figure 1. Drivetrain Plate Assembly

Drivetrain design was focused on minimizing frictional loss, increasing alignment reliability and repeatability, lowering center gravity of the vehicle, and ease of assembly and disassembly. A chain and sprocket system using a #25 chain and 1:9 reduction was selected. The #25 chain provides a light weight but highly efficient power transmission and the 1:9 reduction allows the selected motor to run within its highest efficiency power bandwidth while keeping the wheel speed within an operable range of 15-20 MPH. The driven sprocket, custom designed with spline profile to interface with the rear Onyx hub, was waterjet in the Industrial Technologies machine shop to allow for this high ratio of reduction. The design of a single two-tier plate lowered the center gravity of the vehicle and ensured all components including motor-to-drive-sprocket and driven-sprocket-to-wheel are mounted on a self-contained unit for repeatable, accurate chain alignment. Alignment repeatability between the sprockets was ensured by locating pins in the motor mount and wheel dropouts. The rear wheel location alignment between the rear wheel and front two wheels was determined using an alignment jig that located the axle positions of all three wheels. Locating pins were placed between the motor plate and chassis to ensure reliability when taking the drivetrain assembly in and out of the car.

The motor plate with all components assembled was tested on the Supermileage inertial dynamometer completed winter quarter by Chris to provide us with testing data on the powertrain assembly. This data was able to qualify our design without needing a driver or a fully operational vehicle.

This paper provides a detailed report of preliminary background research collected on the main subsystems, selection of design concepts, and full documentation on the system selected. Concepts have been selected based on the needs of the club and requirements of Shell Eco-Marathon rules. Technical specifications and targets are also presented which have guided and validated the design. Basic prototyping for concept validation is included for the motor plate and basic packaging concepts. A basic timeline of the project can be found in Appendix A.

3 Background Research

3.1 Customers and Customer Needs

The main customer of our project was the Cal Poly Supermileage team, advisor Dr. Mello, and project sponsor, William Sirski. For the team to compete in the Shell Eco Marathon the project had to fulfil the technical and safety requirements of Shell Eco-Marathon. Additionally, subsystems on the Supermileage team provided requirement for interfacing with their vehicle domains. Specific needs for each Supermileage subsystems and Shell Eco-Marathon rules as they apply to electric propulsion prototype vehicles have been delineated in Appendix B.

The driving needs for this project are

- Energy efficiency of 250 mi/kWh to place within the top three teams
- Design and build custom made motor controller board
- Develop software that controls the motor with average speed of 15 mph
- Size and selection of an electrical motor along with battery specification
- Selection and design of drivetrain and components mounting
- Repeatability of accurate chain alignment
- Ease of drivetrain assemble and disassemble
- System reliability defined by completing a 13-mile run before the need to replace or fix any mechanical or electric parts (equivalent to 2 competition runs)

While the primary need of the club was to design a car that can be brought to competition, the secondary need was providing the team with a well-documented design that creates a solid foundation for future improvements of the Supermileage electric vehicle. This paper provides that foundation.

3.2 Design Observations at Shell Eco-Marathon 2018

There were multiple teams that attended the Shell Eco-marathon in 2018 and competed with a variety of electric vehicle designs. Many teams prefer brushless DC motors rather than brushed motors for their greater efficiency, yet not many were able to program and control a brushless DC motor. The motor controller designs typically included a motor driver with supplemental circuitry to control the vehicle speed. Additionally, many teams used a sprocket and chain drivetrain or hub motors. Teams with chain and sprockets performed better than those with hub motors. Our research into different drivetrains and motors will be discussed.

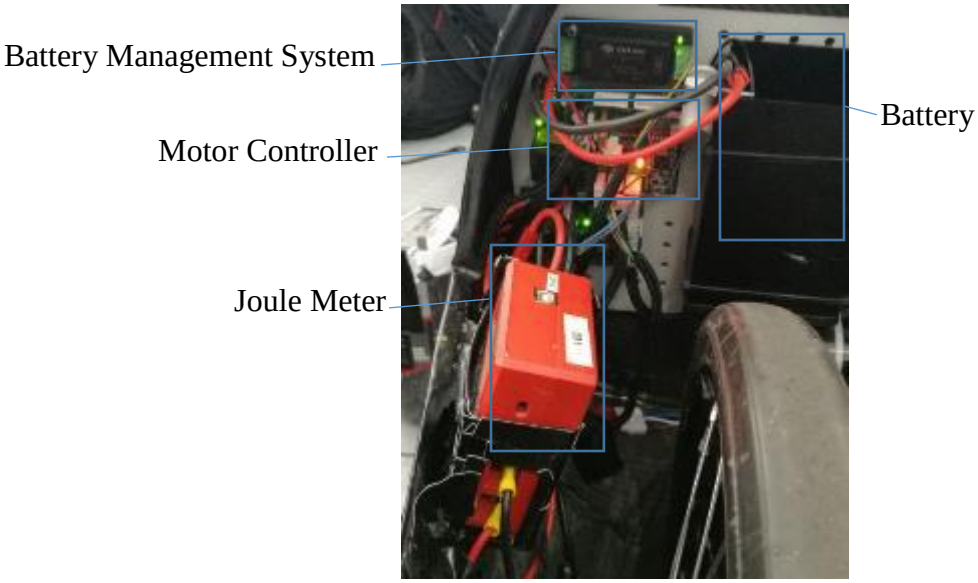

Figure 2: Duke University Battery Electric Vehicle Motor Controller Configuration

Shown in Figure 2, Duke University's battery electric team used a Teensy 3.2 microcontroller with 5V reduction with the battery mounted on the firewall. A high school team, Central Coast High school, used motor drivers that took readings from the Hall Effect sensors and sent analog signals that fed directly to Pulse Width Modulation (PWM) to actuate the motor. Further research on motors and motor drivers will be discussed in Motor and Motor Control Background.

3.3 Interviews

3.3.1 Charlie Refvem

Charlie Refvem is a Mechanical Engineering grad student doing research on motor control and has a wealth of knowledge about electric motors and their applications. He suggested that we investigate direct drive, since a drivetrain may be responsible for considerable losses. Additionally, he highly recommended that we select a brushless permanent magnet DC motor with magnetic sensor feedback. Ideally, the selected motor driver will provide Field Oriented Control (FOC), using the feedback to manage the three phase waveforms that drive the motor. The feedback ensures that the electric pulses are timed correctly, providing the maximum possible torque and reducing losses.

Charlie recommended that we maximize the operating voltage of the system, reducing current, and use short, high quality wires with low resistance. We will need to consider using thicker wires to reduce resistance but acknowledge the increasing weight with the use of large wires. The system will also operate at its highest efficiency when it is cool, so packaging must consider cooling.

To aid the selection of our motor, Charlie recommended that we run parametric simulations to overlay motor performance with the system curve to find our ideal operating point.

3.3.2 Professor Majid Poshtan

Majid Poshtan is an electrical engineering professor at Cal Poly. He provided advice on brushless DC motors and the parameters such as torque, rated voltage, and speed to consider when selecting a motor. In his overview on what will impact the overall efficiency of the vehicle he stressed that the motor will play a crucial role, so a carefully selected motor based on simulations and limitations by the Shell Eco-Marathon will determine our overall efficiency. The motor controller will not draw as much power as the motor, but the timing of the generated signals will affect the motor efficiency. He suggested buying as many off the shelf components as we can and use thick wires to increase the efficiency of the vehicle. As electrical power is defined in $P=IV = I^2R$, for the same power rating for motors, motors rated for higher voltage are more efficient, allowing the use of thicker wires, which costs less energy consumption in circuits. He also went over how the mechanical and aerodynamic aspects of the vehicle will improve the efficiency of the vehicle. The aerodynamics of the vehicle are already set as we will reuse the chassis of a previous vehicle.

3.3.3 Professor Art MacCarley

Professor MacCarley is an electrical engineering professor at Cal Poly. He has extensive experience with electric vehicle research and control systems. Dr. MacCarley has served as an advisor for the motor controller design. In our first interview he suggested using insulated gate bipolar transistors (IGBTs) instead of MOSFET devices to handle voltage spikes more reliably. His warning was that for higher power switching, MOSFET devices fail catastrophically when the current switching (di/dt) increases greatly because of the direct relationship between the change in current and voltage through the inductors in the motor. IGBTs can be protected with a forward bias Zener diode or Metal Oxide Varistor (MOV). He suggested looking at Sanasonics protection diodes called sNRS, which are really MOVs. These devices are high voltage, high current breakdown devices. The IGBT has a limit of about 120V based on his experience. Using power MOSFITs for lower power uses could be better, which we may be able to get by using MOSFETs for our motor due to its low power operation. However, power MOSFETs are more sensitive to failure because thin oxide channels separate the gate and channel, when breakdown voltage is exceeded it creates a welded short.

Dr MacCarley also suggested looking at International Rectifier (now part of Infineon Technologies) or IXYS for high quality power FETs and integrated drivers for three-phase invertor. For the mechanical emergency shut-off he suggested looking at products from Kilovac.

Concerning the motor feedback, Dr. MacCarley shared that the highest performing motors use a resolver which is a digital positioner. These high efficiency motors use separate position sensors. Dr. MacCarley advised that to build the most efficient motor controller we will need to fully understand how the motor we select works to build the most efficient synthetic sine wave modulator. For high RPM, a high pulse deration modulator is needed. Since power is dissipated during the switching on to off and no power is consumed at full on or full off, minimizing the switching time requires high performance MOSFETs with both high current capacity at fast switching rate. He also suggested that we could use FET device specifically optimized for high current and high switching for our power application. He warned that channel capacitance will be important. He also reminded us that electric motor efficiency is primarily determined by the type of magnets used, commutation control, and winding of the motor.

Dr. MacCarley suggested that we might be able to use a hub motor or other electric bike motor if we replace their electronics but still use their drivers. He also suggested finding a company that could sponsor the motor and give technological help to get coding right. He also suggested researching Halbach motors and contacting companies for a sponsorship. Considering other types of motors, Dr. MacCarley highly suggested using permanent magnet motors with samarium-cobalt or high-quality magnets so that no energy is wasted in created magnetic fields. Another resource he suggested was to find a hobby motor builder who would like to showcase their motor in our car. We could potentially get the motor and technical advice for free in exchange for free advertisement in an international competition.

He also advised that we may face a decision of designing to be innovative and designing to get to competition. If the goal is to get to competition, he suggested using as many off the shelf components that fall under Shell Eco-Marathon rules.

Dr. MacCarley also advised us that TI should give us any components that we want, based on his experience with requesting supplies for his own classes and student projects. He suggested that they may also be able to offer advice from their application engineers or through alumni working at TI.

3.4 Motor and Motor Control Background

Shell Eco-Marathon competition rules prohibit the usage of an off-shelf motor controller or a modified motor controller for an electric propulsion system. Thus, we designed a purposely built motor controller to drive the motor. Typically, the motor controller consists of the following: a controller board that contains micro-controller and electronics connected by printed copper wire circuits, and a driver stage that takes Pulse Width Module Signal (PWM). Electronics range from sensors, motor drivers, power MOSFET and so on and will be discussed in a later section. A micro-controller comes in a tiny package yet is quite powerful in doing data computation and processing. The Pulse Width Module Signal generated from the controller gets amplified and sent to a power stage to generate 3-phase current to drive the motor. The power stage consists of half-bridges. In this section we will discuss results from background research for types of motor, motor control theory and motor candidates. Control algorithms, motor control technique and theory are also discussed with a focus on minimizing energy consumption.

3.4.1 Overall View of Motor

A distinct line is drawn between DC (direct current) and AC (alternating current, single phase and 3 phase) motors. Since our vehicle runs on a rechargeable lithium-ion battery, this research focuses on DC motors. Our background information on DC motors indicated the advantages of using DC motors are:

1. Quick response, and high ratio of torque to inertia
2. Adjustable speed by varying the voltage applied to the motor
3. Torque can be controlled by varying the current applied to the motor
4. Reversible direction by switching the polarity of the voltage applied to the motor
5. Dynamic braking can be obtained by reversing the polarity of the power while the motor is rotating

The DC motor is a machine that transforms electric energy into mechanical energy. DC motors have inductors inside, which produce the magnetic field used to generate movement by the effects of electromagnetism. One way to classify DC motor is the commutation method: if it is done electronically or mechanically. Electronic commutation is researched and developed in last decade and involves heavy motor control theory and vector calculus, and it has become sophisticated and available to market thanks to the state of powerful fast switching micro-electronics.

Here is how mechanical commutation in a typical brushed DC motor work. There are permanent magnets mounted on the inner wall and a spinning armature on the inside. The permanent magnets are stationary, so they are called the stator. The armature contains an electromagnet. When electric current run into this electromagnet, it creates a magnetic field in the armature that attracts and repels the magnets in the stator, spinning the armature 180 degrees. To keep it spinning, actively changing the poles of the electromagnet is achieved by internal mechanical commutation. The internal mechanical commutation is achieved by brushes in contact with two spinning electrodes attached to the armature that flip the magnetic polarity of the electromagnet as it spins. The armature is usually attached to a rotating shaft that provides the output torque.

Since spinning motor would require the brushes are in contact with two spinning electrodes, there would be frictional loss and overtime the brushes tend to wear out; hence, the brushed DC motor would not start.

Electronic commutations are seen in Permanent Magnet motors including Brushless Direct Current (BLDC) motors and Permanent Magnet Synchronous Motor (PMSM). They are driven by electronic commutation, which eliminates the wear and tear of the brushes involved with mechanical commutation of brushed DC motors. Even though they are called DC motors, they are, in fact, quite like AC motors, in which DC current passes through an inverting stage in powering three phases of the motor individually. Different electronic commutation patterns and motor control theory will be discussed in the later section.

In BLDC motors, the permanent magnet is housed in the rotor and the coils are placed in the stator. The coil windings produce a rotating magnetic field because they are separated from each other electrically, which enables them to be turned on and off. The BLDC's commutator does not bring the current to the rotor. Instead, the rotor's permanent magnet field trails the rotating stator field, producing the rotor field.

Permanent magnet synchronous motor (PMSM) is a type of synchronous motor. Synchronous motor is constructed such that permanent magnets are rigidly fixed to the rotating axis to create a constant motor flux. The rotating stator field must rotate at the same frequency as the rotor permanent magnetic field. If not at the same frequency the rotor will experience rapidly alternating positive and negative torque, resulting in less than optimal torque production, excessive vibration and noise.

PMSM is quite like a BLDC motor, also powered by 3-phase, but more efficient. The main differences between these two are: regular BLDC requires trapezoidal winding and trapezoidal supply, and PMSM requires a sinusoidal winding and supply, which are harder to generated than trapezoidal winding and supply, yet it can be accomplished with existing motor drivers in the market. The PMSM is also known as brushless asynchronous motor (BLAC) or synchronous AC motor. In "AC Motor Control and Electric Vehicle Application" by Kwang Hee Nam, he provides a detailed list of comparison between BLDC and PMSM motors which are listed in Appendix C. The differences between BLDC and PMSM are in stator winding, the use of types of sensor for position feedback and control algorithm complexity.

Table 1. Comparison between BLDC and PMSM motors by Kwang

	BLDCM	PMSM
Back EMF	Trapezoidal	Sinusoidal
Phase current	Square	Sinusoidal
Torque ripple	high	low
Position sensor	Hall sensors (inexpensive)	resolver (expensive)
Stator winding	concentrated (less copper)	distributed (more copper)
PM usage	large	relatively small
Eddy loss in PMs	large	relatively small
Control complexity	simple	complicated
Speed range	narrow	wide
Inverter price	low	high

PMSMs are advantageous in incorporating the reluctance torque in the field-weakening range, so that they can be designed to have a wide constant power speed range (CPSR). As a result, PMSMs have higher power densities than any other types of motors.

In summary, our research indicated that PMSM incorporated with field-oriented torque control (FOC) minimizes current drawn among 3-phase motor power line without scarifying performance. Minimizing current drawn reduces energy consumption; thus, yield maximizing vehicle efficiency.

For permanent magnet DC motor with field-oriented control, regenerative braking will become a viable option to regain small proportion of energy due to braking. This could be implemented and would provide a path forward for improving efficiency. However, it adds complexity to the microcontroller design and power board management.

3.4.2 Motor Control Theory and Application

Modern motor control for AC motor and PM motor is performed electronically inside a microcontroller, in which the controller converts the applied DC into AC to drive the motor (like BLDC or PMSM) with complex driving algorithms. Various driving/control algorithms are employed to energize the coils in a sequence to achieve desired directional rotation. The rate at which the windings are commutated is proportional to the speed with which the motor runs. Three common control algorithms are listed in the following:

Trapezoidal control, also known as 6-step on and off switching control, this is the simplest algorithm. For each of the 6 commutation steps, the micro-controller controls which current path is formed between two windings, leaving the third winding disconnected. This method generates high torque ripple, leading to vibration, noise, and poorer performance compared to other algorithms.

Sinusoidal control, also known as voltage-over-frequency commutation, is achieved by programming the micro-controller to output synthetic sine wave current to 3-phase motor windings. Sinusoidal control overcomes many of the issues involved with trapezoidal control by supplying smoothly (sinusoidal) varying current to the 3 windings, thus reducing the torque ripple and offering a smooth rotation. However, these time-varying currents are controlled using basic PI regulators, which lead to poor performance at higher speeds.

Field Oriented Control (FOC), also known as vector control, FOC provides better efficiency at higher speeds than sinusoidal control. It also guarantees optimized efficiency even during transient operation by perfectly maintaining the stator and rotor fluxes. FOC also gives better performance on dynamic load changes when compared to all other techniques.

Following Charlie Refvem suggestion of possibility implementing Field Oriented Control, further investigations were made to outline the pros and cons of FOC and detail the theories and implementation of such control

3.4.2.1 Field Oriented Control

Field oriented control (FOC), or vector control, implementation allows BLDC to run more efficient, and smoother with lower torque ripples. It also provides better dynamic performance to load and speed changes. Furthermore, using a decoupled control of flux and torque, the motor can be tuned to run above nominal speed using field weakening techniques.

The measure of the rotor flux is essential for FOC. The rotor flux can be measured directly and indirectly. The direct method approach is to use hall sensors or flux sensing to measure the rotor flux and calculate the rotor flux angle around the air gap. The direct method is doable but may

not be easy due to space limitation, armature reaction and noise generated from the rotating rotor. For synchronous motor, the rotor flux is equal to rotor speed, which can be directly measured by position sensor to calculate rotor speed. The rotor position is required for variable transformation from stationary reference frame to synchronously rotating reference frame via Park transformation. A more practical way is to measure the stator current with current sensors and compute voltage values, such that the rotor flux is calculated indirectly from the stator flux and stator current (Kwang, 126).

The goal of FOC is to separately control the torque producing and magnetizing flux components, which allow us to decouple the torque and the magnetizing flux components of stator current. Torque output is expressed as the outer product of flux and current vectors; hence, to maximize torque the two vectors should be orthogonal. For a given motor driven by three-phase current system, the current has two degree of freedom that are allocated to two functionalities: flux regulation and torque control. Based on the synchronous reference frame, the roles of current position are naturally decomposed and represent those of the separately excited DC machine.

Rotor field-oriented control is achieved by aligning the rotor d-axis to the rotor flux, which not only makes the component of rotor flux in rotor q axis $\lambda_{qr}^{e} = 0$ to be zero, but also the rate of change of rotor flux component in q-axis $\dot{\lambda}_{qr}^{e} = 0$ to be zero as shown in Figure 3: Alignment of d-axis to the rotor flux.

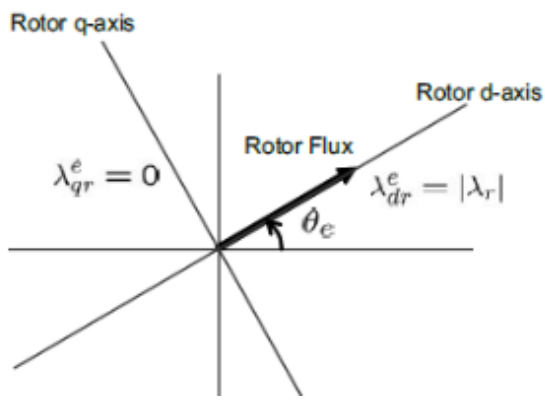

Figure 3: Alignment of d-axis to the rotor flux

Two motor phase currents are measured and transformed via Clarke transformation and Park transformation to give the current in the d, q rotating (synchronous) reference frame. The measured stator current is represented by a vector in synchronous reference frame, which is transformed a three-phase time and speed dependent system into a two co-ordinate (d and q co-ordinates) time invariant system. The d-axis current should be regulated to keep a desire field level, while the q-axis current, functioning as the armature/rotor current need to be controlled for torque production using Proportional Integral (PI) Controller.

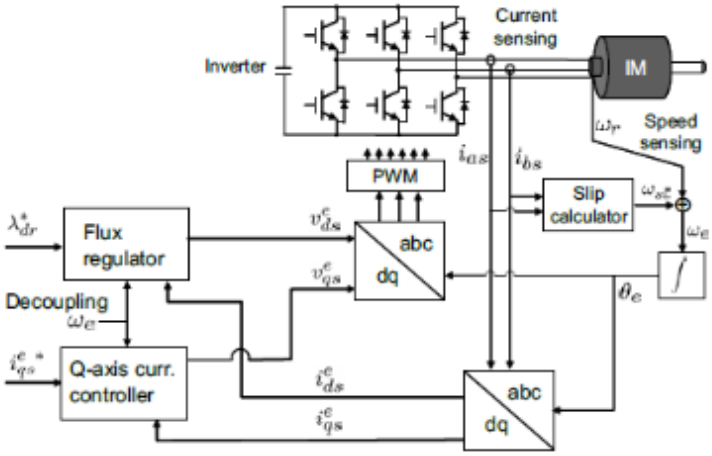

Figure 4. Field-Oriented Control Block Diagram Involving Coordinate Changes by Kwang

Figure 4. Field-Oriented Control Block Diagram Involving Coordinate Changes illustrates a typical field-oriented control block diagram. The measured any two-phase current from stator is used to calculated slip, which is used to estimate the rotor flux angle with known rotor speed. Phase current is measured by utilizing Hall sensor or a shunt resistor, and since the phase current sum is equal to zero, measuring only two-phase currents is adequate. Also, the measured current is transformed and decoupled for flux regulator and q-axis current controller. Lastly, the computed voltage vector in q, d coordinate is transformed to normal coordinate and feeds to on-duties of the PWM. (Kwang, 116)

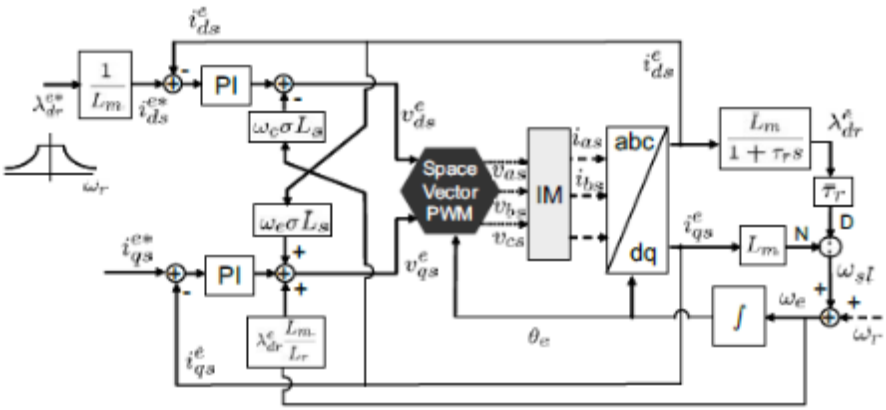

Figure 5. Block Diagram for Rotor Field-Oriented Control Scheme

Figure 4 shows a detailed control block diagram for the rotor field-oriented control scheme. The current control part equation and slip calculation equation are shown in Appendix C.

3.4.2.2 Sensor versus Sensor less Control

Position feedback of the rotor is essential to power and drive a BLDC/PMSM motor. This can be achieved using Hall-Effect sensors or sensor less control.

Three Hall-Effect sensors are used to provide position feedback of the rotor from the three-phase BLDC motor. The signals obtained from Hall Effect sensors are sent to the controller such that the controller can energize the windings in the correct sequence and timing.

For sensorless motor-control, a microcontroller shall be programed to determine the relative position of the stator and rotor without the need for Hall-effect sensors by monitoring the back EMF. Back EMF, also known as an electromotive force, is created when electric motors generates a voltage potential due to the rotating shaft in a changing magnetic field, and it also tends to resist the rotation of the motor.

Sensor less motor control simplifies motor construction by eliminating wiring connections that would be needed to support the sensors and improves reliability when dirt and humidity are present. For a given motor of fixed magnetic flux and number of windings, the EMF is proportional to the angular velocity of the rotor. During the start-up phase, a stationary motor generates no back EMF, making it impossible for the microcontroller to determine the position of the motor; thus, the motor is started in an open loop configuration which allows adequate EMF to be generated and then the microcontroller can take over.

3.5 Vehicle Model and Simulation

The creation of a good model is essential to making the right design decisions moving into the future. The goal of the model is to simulate the performance of the vehicle with various combinations of subsystem components.

One aspect explored through the simulation is the effect of driving with a burn and coast method, where the motor is run in intervals to pick up speed, versus maintaining a constant speed by running the motor always. These two driving cases were selected from our understanding of the components in the drivetrain and the vehicle dynamics. Electric motors typically run most efficiency at a high RPM, therefore the largest power loss at the motor comes from accelerating from a low speed to a high speed. When the motor is running, there is power lost through the drivetrain, battery and electrical system due to inefficiencies. Also considered is that the drag and road losses are larger at higher speeds. To balance all these losses and design the most efficient overall system it was necessary to roughly estimate the driving strategy so that the reduction ratio for the sprockets can be optimized to run the motor at its peak efficiency during the operating conditions the car would experience the most. There were many factors considered before we selected our components and driving method and the simulation helped balance these tradeoffs and bring us to a satisfactory operating point.

Previous simulations have been created for the combustion vehicle in Simulink. The simulation considers drag, power consumption from the engine, inefficiencies in the drivetrain, and other factors to estimate the performance of the vehicle. The structure of these were considered as we developed our own electric car simulation.

The goal was to develop a model that can be used for future electric cars. The parameters for drag, gear ratios, efficiency, motor specifications from its power curves, vehicle speed commands, are all configurable.

3.5.1 Developing the Vehicle Model

The vehicle was modeled as a first order system. The simplified model of the vehicle was derived by analyzing the wheel as seen in Figure 6.

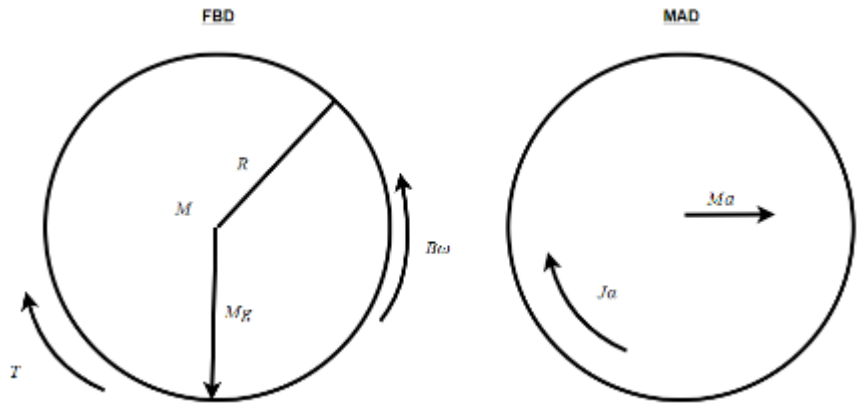

Figure 6: Wheel free body diagram and mass acceleration diagram

Assuming no slip, the torque on the wheel, T, is a combination of the torque provided from the motor through the drivetrain and the torque on the vehicle due to road loads (i.e. the change in elevation in the road profile). R is the radius of the wheel, B is the equivalent viscous damping on the vehicle due to air drag and rolling resistance, and J is the equivalent rotational moment of inertia of the vehicle on the wheel.

The equivalent inertia of the vehicle reflected onto the wheel includes the effects of the mass of the car through the wheel radius, the inertia of the drivetrain through the gear ratio, GR, and the inertia of the tire.

$$J = R^2 M_{car} + J_{wheel} + (GR)^2 J_{Drivetrain}$$

For simplicity, we used data collected from coast-down tests on a past Supermileage vehicle to approximate the inertia. This term does not include the inertia of the drivetrain, since the wheel does not spin with the drivetrain when coasting down. For simplicity, the simulated model did not include the inertial effects of the drivetrain.

The equivalent viscous damping includes the air drag and rolling resistance from the wheel hub and drivetrain.

$$B = R^2 B_{drag} + B_{wheel} + (GR)^2 B_{Drivetrain}$$

These values vary depending on the components selected. For simplicity, we analyzed the velocity coast down profile of the previous vehicle recorded with Race-Capture, which is a car data acquisition system, and compared it to the coast down profile of the model in the simulation. The equivalent drag coefficient was modified until the velocity coast down profiles matched.

The equations of motion were derived by summing the moments about the center of the wheel.

$$\sum M_o = \sum \mathrm{M}_o$$

$$B\omega - T = -J\alpha$$

$$J\dot{\omega} + B\omega = T$$

Taking the Laplace transform and rearranging variables, we get the transfer function of the vehicle which outputs the angular velocity of the wheel for an input torque.

$$\frac{\Omega}{T} = \frac{1/J}{s + B/J}$$

The values in Table 2 show the estimated values used to model the vehicle.

Table 2: Vehicle properties

Property	Value	Units
W_{car}	220	lbf
B	0.065	$bf * ft * s$
R	9.75	in
J	4.51	$lbf * ft * s^2$

3.5.2 Developing the Road Profile

The change in elevation versus position is required to approximate the torque on the vehicle from the road. The change in elevation versus position of the Sonoma Racetrack was measured by GPS onboard our vehicle. The collected data was very noisy, but a Savitzky-Golay filter, which smooths according to a quadratic polynomial, was used in MATLAB to smooth the road data as seen in Figure 7.

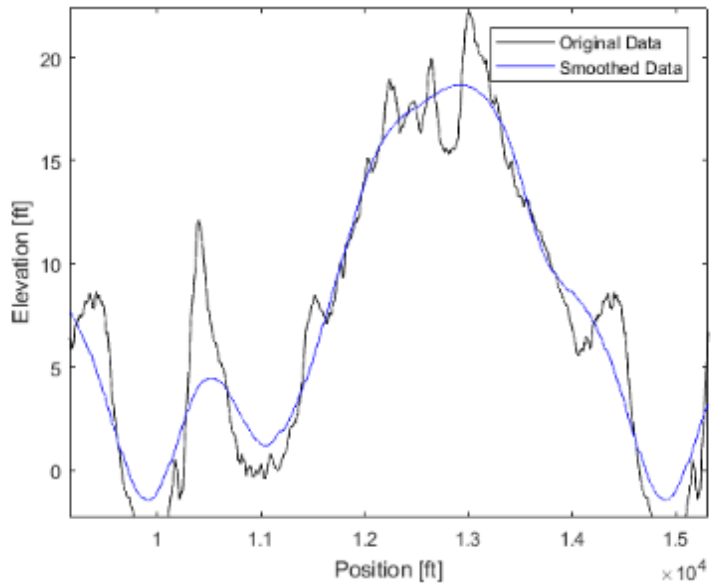

Figure 7: Sonoma raceway elevation versus position

From the smooth road profile, the slope of the road versus position was calculated as shown in Figure 8.

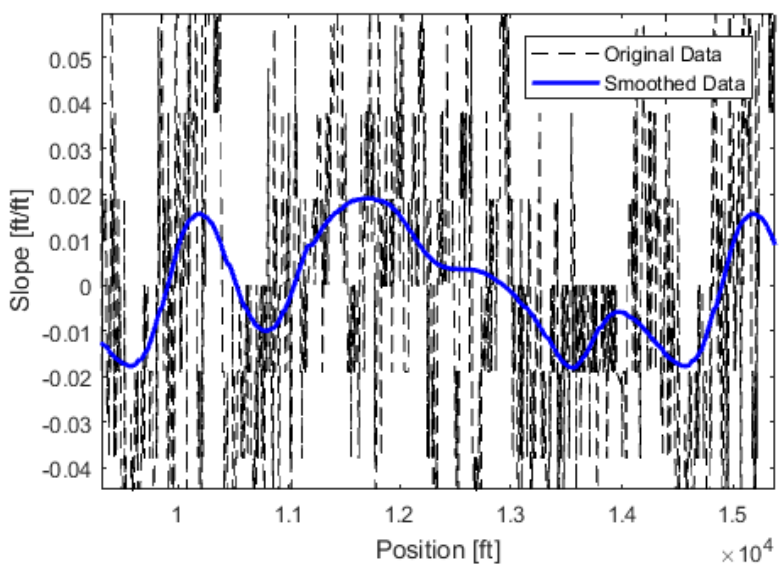

Figure 8: Sonoma raceway slope versus position

The torque applied to the vehicle from the road slope may be calculated as a function of the slope based on a model of an object on an incline.

$$\theta_{slope} = \tan^{-1}(slope)$$

$$T_{slope} = M_{car} g \sin(\theta_{slope}) R$$

The torque from the road is added to the torque provided by the motor through the drivetrain to determine the total torque on the vehicle

$$T_{total} = T_{motor} + T_{slope}$$

Combined, the total torque will either accelerate or decelerate the vehicle. According to the equations of motion, to maintain a constant vehicle speed, the magnitude of the motor torque must equal the combined torque from the road and the torque from viscous damping, $B\omega$.

3.5.3 Developing the Motor Model

The motors have been modeled as simple DC motors with an internal resistance, and inductance. Energy is transferred from the electrical to mechanical domain by the motor torque constant, k_t, in units of $\frac{Nm}{Amp}$, and the back electromotive force (EMF) produced by the motor is described by the back EMF constant, k_v, in units of $\frac{Volts}{RPM}$.

The behavior of a DC motor may be explained by the relationship between the torque and RPM. As RPM increases, the available torque from the motor decreases. This behavior can be justified mathematically by observing the torque and EMF constants. As RPM increases, the voltage generated by the motor increases. As the generated motor voltage,V_m, approaches the source voltage, V_s, the voltage drops across the motor decreases. According to Ohms law, the current is proportional to the voltage drop over the resistance.

$$I = \frac{V_s - V_m}{R_m}$$

Thus, the current through the motor decreases as the RPM increases. Since the torque is directly proportional to the current from the torque constant, the torque also decreases.

The parameters required to model the motor are the motor resistance, R_m, the motor torque and EMF constants, k_t andk_v, and the nominal motor voltage, V_s. The accuracy of the model can be improved by including the value of motor inductance, L_m, if it is provided by the manufacturer.

If any of these specifications are not provided by the motor manufacturer, they may be derived from other parameters. If the motor torque and current at two points are known, the torque constant can be calculated.

$$k_t = \frac{T_2 - T_1}{I_2 - I_1}$$

The motor resistance can be calculated from the motor voltage and peak current.

$$R_m = \frac{V_s}{I_{peak}}$$

By understanding the fundamental relationships between properties of a DC motor, there are many more ways to estimate the motor parameters necessary to develop a functional model.

3.5.4 Simulation Architecture

The simulation is created as block diagrams in MATLAB Simulink environment. The simulation has five different sections: the controller, the motor system, the road profile, the vehicle system, and the driver profile. Refer to Appendix D for the complete block diagram.

3.5.4.1 Motor Controller

The motor controller is modeled as a simple proportional, integral, and derivative controller (PID). The input is the error between the command speed and the actual speed in miles per hour, and the output is a voltage command to the motor. This will allow us to tune the controller and adjust the system's response.

3.5.4.2 Motor System

The motor system takes the voltage command and wheel angular velocity as inputs, and outputs the motor torque to the vehicle as shown in Figure 9.

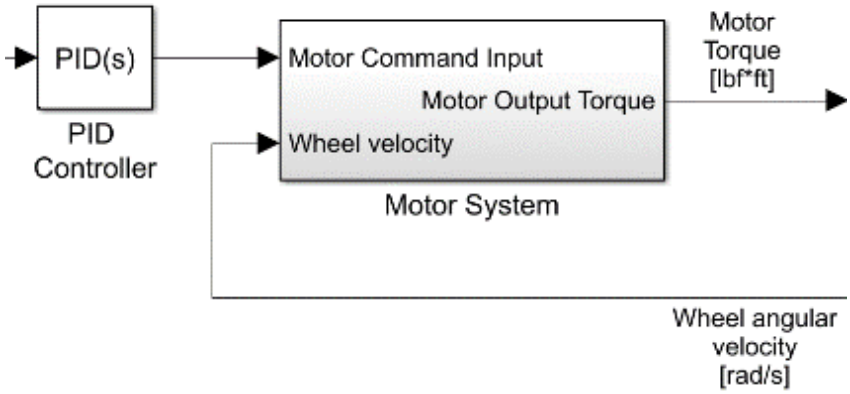

Figure 9: Motor system block exterior

Figure 9 illustrates control system implementation of proportional integral derivative (PID) controller in the Supermileage electric car. The inner workings of the motor system are shown in Figure 10.

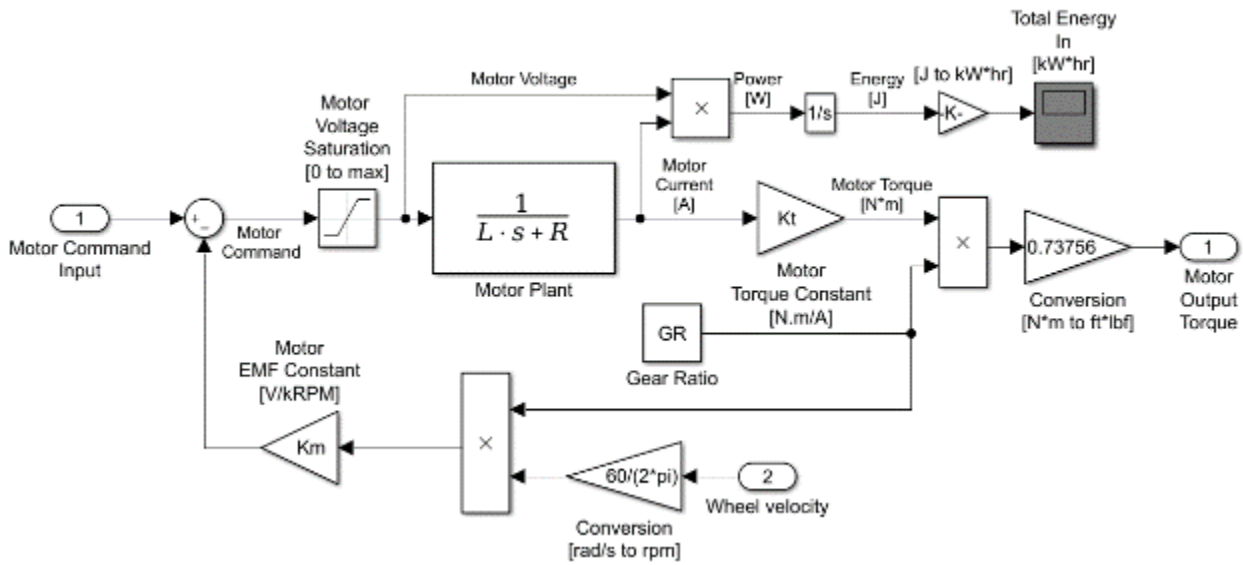

Figure 10: Motor system block interior

The difference between the input voltage and back EMF is saturated due to the capabilities of the battery before it enters the motor plant. The plant outputs the current, which is converted to a torque. The torque is amplified with the drivetrain gear ratio, converted to pounds force, and output to the vehicle. The energy consumed in kilowatt hours is calculated by multiplying the voltage and current through the circuit during operation (power in Watts), integrating with respect to time, and converting from Joules.

3.5.4.3 Vehicle System

The vehicle system inputs the combined motor and slope torque and outputs the angular velocity of the tire as shown in Figure 11.

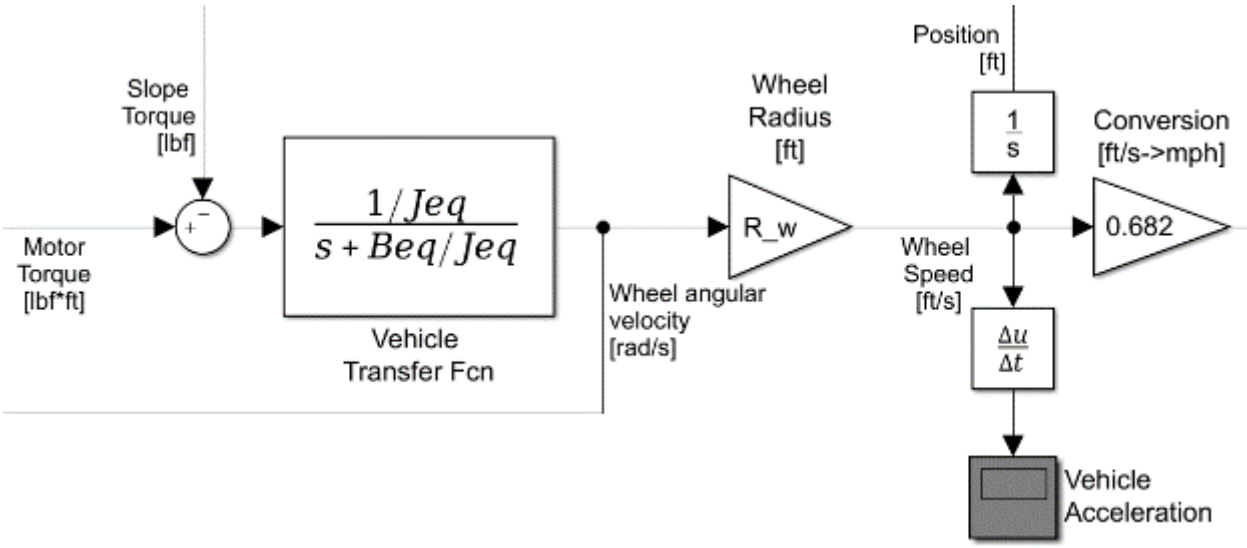

Figure 11: Vehicle system block diagram

The angular velocity is multiplied by the radius and converted to the vehicle speed in miles per hour. The position of the vehicle on the track in feet is determined by integrating the speed of the vehicle with respect to time.

3.5.4.4 Road Profile

The road profile takes the road position as an input and outputs the track slope and disturbance torque from the road slope to the vehicle as shown in Figure 12.

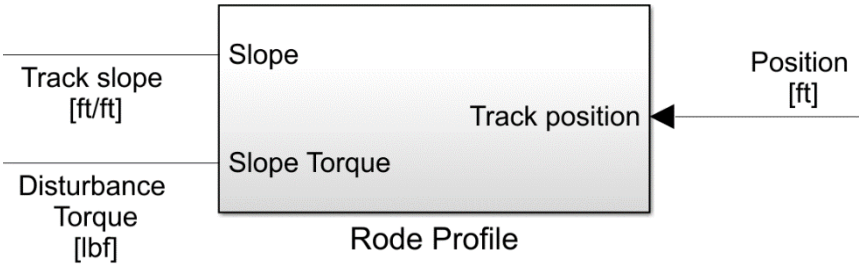

Figure 12: Road profile block exterior

The interior of the road profile block is shown in Figure 13.

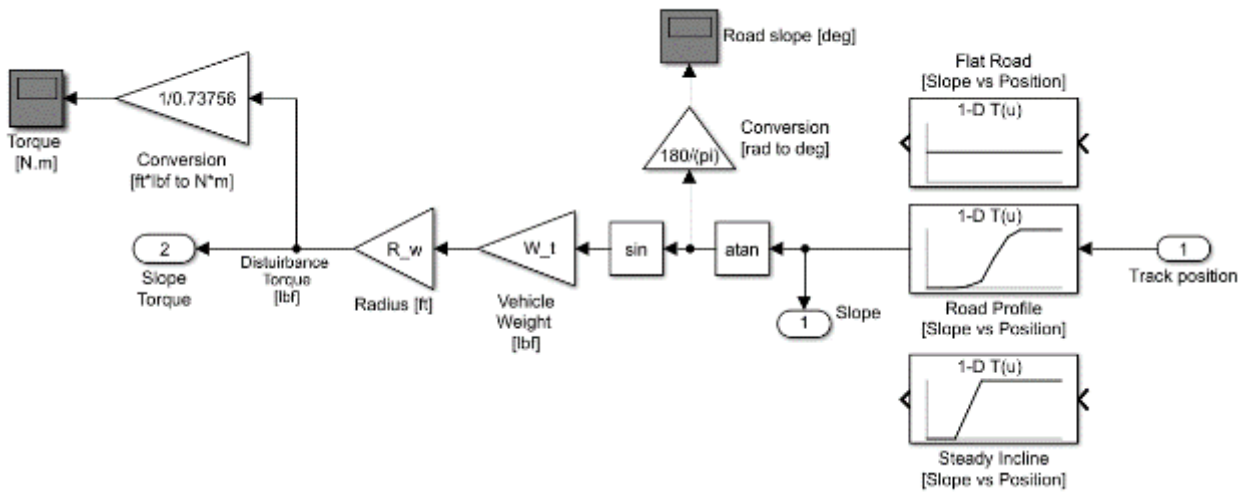

Figure 13: Road profile block interior

The road profile is imported as a lookup table which outputs the road slope for the given position of the vehicle on the track. The slope is converted to an angle which is multiplied by the weight of the vehicle and radius of the tire to output the torque on the vehicle in pounds force. The slope of the road is also output to aid the creation of the driver profile

3.5.4.5 Driver Profile

The driver profile aims to create an optimal driver profile to minimize the amount of energy required to complete the course. The inputs are the slope of the track, the track position, and the speed of the vehicle, and the outputs are the burn profile and a flag to end the simulation when the track is complete. The exterior of the block is shown in Figure 14.

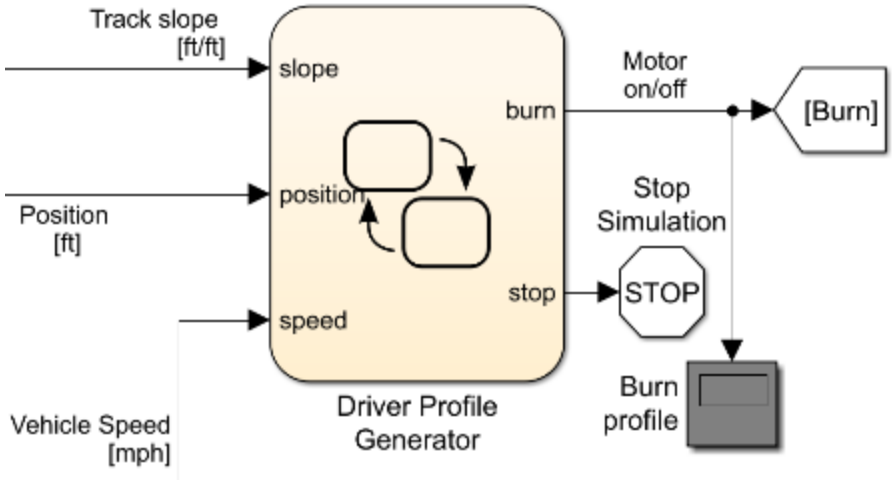

Figure 14: Driver profile block exterior

The interior of the block is shown in Figure 15.

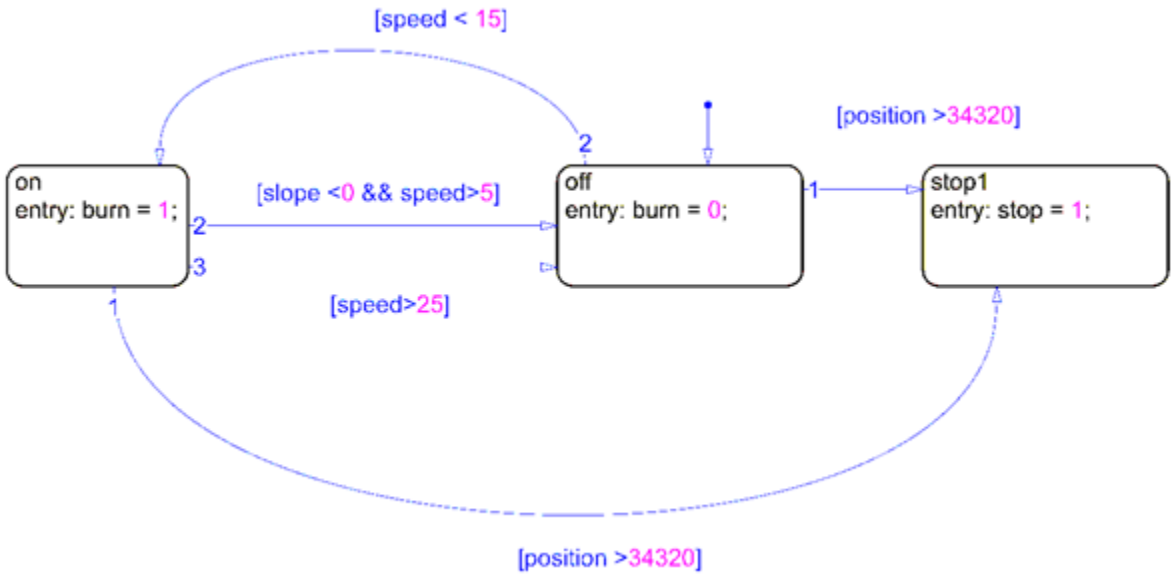

Figure 15: Driver profile block interior

The driver profile block was created in Stateflow and uses logical transitions to determine if power should be applied to the motor. The generator checks the slope of the road, and if the slope of the road is negative (i.e. the car is going downhill) then no power is applied to the motor. Additionally, speed thresholds for minimum and maximum speeds may be defined.

3.5.5 Setting up the Simulation

The motor, vehicle, and road parameters are defined in MATLAB. The road data is imported from a spreadsheet, smoothed, and an array of slope versus position is generated. The drivetrain, vehicle, and motor parameters shown in Table 3 are entered in their respective sections.

Table 3: Simulation parameters

Parameter	Description	Example Value	Units
GR	Gear Ratio	7:1	in/in
D_Wheel	Wheel Diameter	19.5	in
W_t	Total Weight	220	lbf
Beq	Equivalent Viscous Damping Factor	0.065	$lbf * ft * s$
M_Volt	Rated Motor Voltage	48	V
Kt	Torque Constant	0.118	Nm/A
Km	EMF Constant	8.81	$V/kRPM$
R	Motor Resistance	0.07	Ω
L	Motor Inductance	0.1	mH

When the parameters are loaded, the Simulink simulation may be run to monitor vehicle

parameters and determine the energy required to complete the course. Currently, parameters for the driver profile are manually set, but the goal is to create an optimization routine to minimize the amount of energy required to complete the track in the required time. Refer to Appendix E for the MATLAB script.

3.5.6 Simulation results

The simulation assisted the selection of our motor and battery. Figure 16 through Figure 20 show the results of four motors run through the simulation. The result is the total energy used by the motor to complete the track in under 26 minutes.

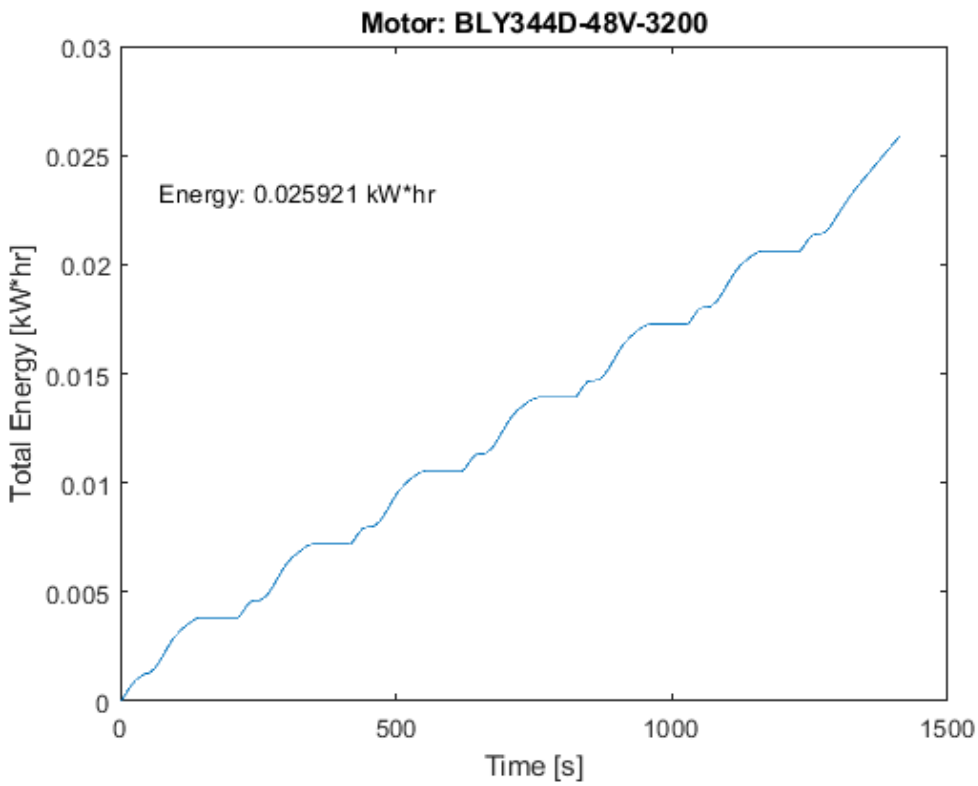

Figure 16: Motor 1 simulation result

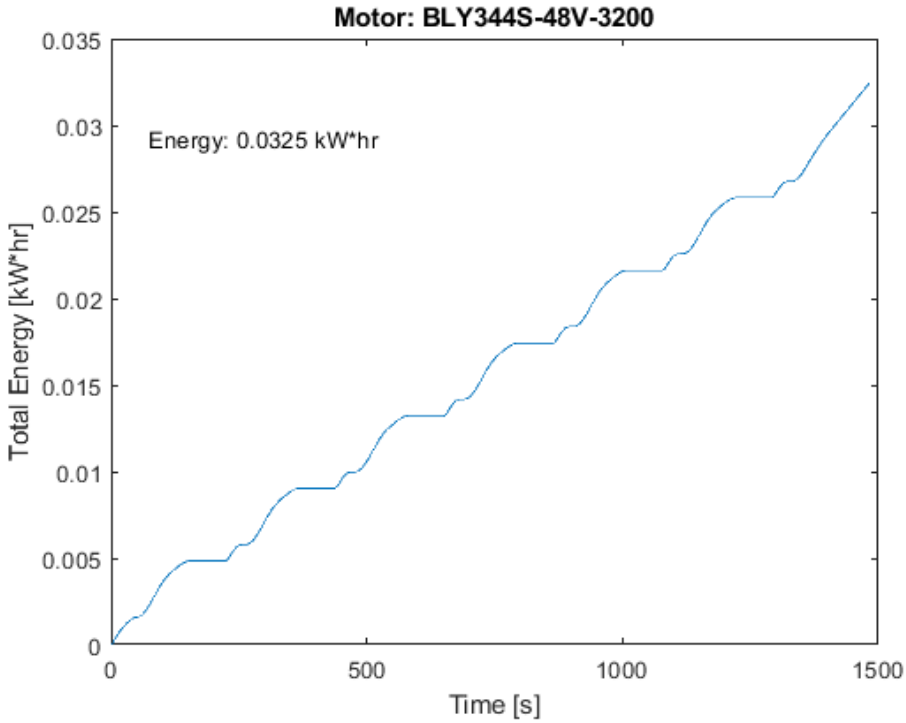

Figure 17: Motor 2 simulation result

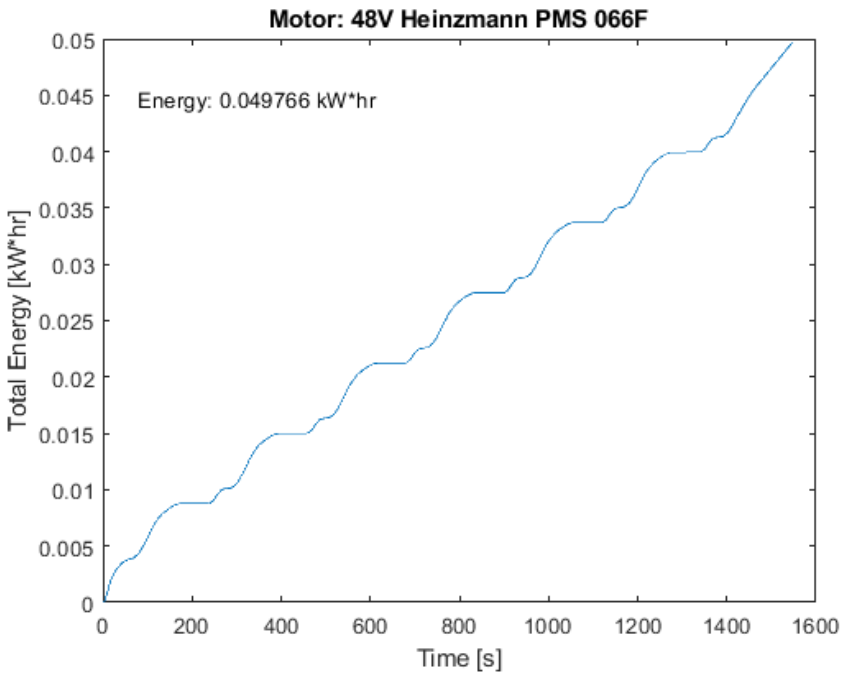

Figure 18: Motor 3 simulation result

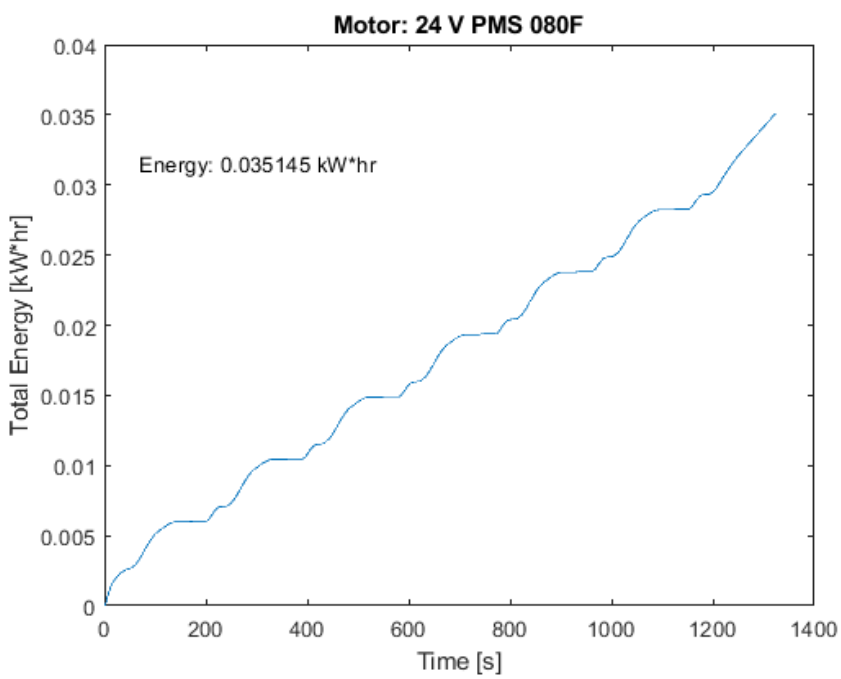

Figure 19: Motor 4 result

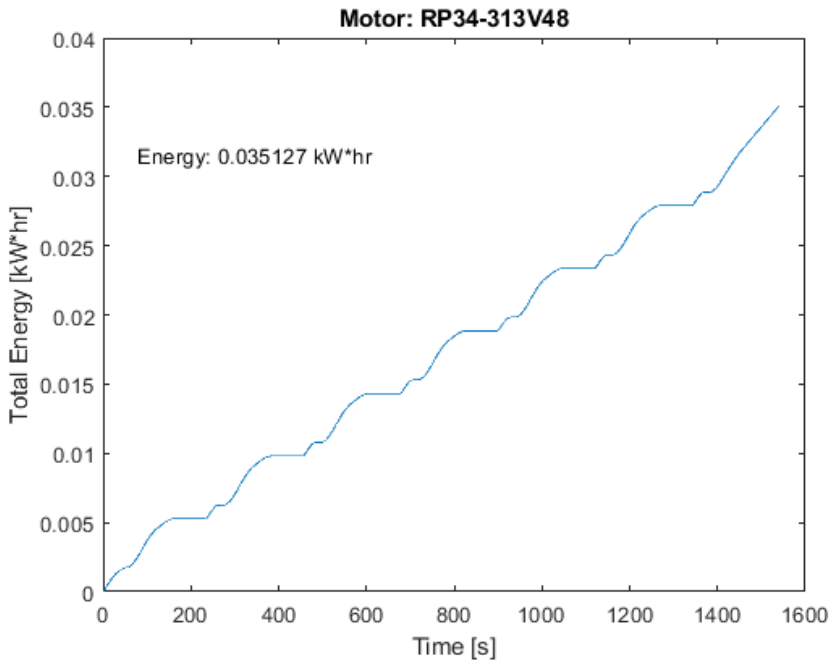

Figure 20: Motor 5 simulation result

These initial results were obtained using approximate values for the motor and vehicle properties. These results aided the initial component selections for the battery and motor. The motor initially selected was the 600 Watt BLY344D, which has an estimated energy consumption of 25.9 watt-hour for the 6.2-mile road profile. However, the team chose to use the smaller BLY343D, since the specifications were similar, and the weight was lower. Additionally, the efficiency point for the BLY343D motor was at 440 Watts, which was higher than the maximum wattage necessary for the vehicle to meet our specifications.

We also ran the simulation with different gear ratios to further improve our simulated efficiency. The results showed that a larger gear ratio would improve efficiency, while limiting top speed. We selected a ratio that allows us to meet our speed requirement.

Further testing may be conducted to validate the selections. Additionally, the simulation parameters may be modified to closer reflect the vehicle and track properties after the vehicle is built and additional test data is collected.

3.6 Electronics

3.6.1 Microcontroller

The microcontroller's role is to take in the driver inputs as digital or analog signals and relay that information to the motor controller in the form of a PWM signal which is converted into a three-phase signal to power the motor. The motor driver allows real time user input like a button or switch to turn on/off the motor or have the controller receive feedback from the motor to adjust the speed on its own.

The microcontroller also receives information from the back emf to measure the speed of the motor and optimize the timing of the three phase signals to drive the motor efficiently. Timing is crucial to having an efficient motor because if the signal is sent too fast or too slow it will not energize the magnets correctly and can cause the rotor to vibrate without spinning or prevent it from spinning entirely. Current and voltage feedback would also be used by the microcontroller to provide accurate and reliable control.

3.6.2 Motor Drivers

Typical BLDC motors are controlled by receiving a Pulse Width Modulation (PWM) signal that is generated from a motor controller. Trapezoidal, sinusoidal and field-oriented control are three control schemes for electronic commutation.

The trapezoidal technique is the simplest, but it causes torque to ripple at low speeds. At each step, two windings are energized (one on low and one on high) while the other windings floats for current return. Sinusoidal control reduces torque ripple. It is achieved by having all three coils remain energized with the driving current in each of them varying sinusoidal at 120 degrees from each other. Field-oriented control relies on measuring and adjusting stator currents so that the angle between the rotor and stator flux is always 90 degrees. It is more efficient at high speeds and give better performance during dynamic load changes and allow accurate motor control at both low and high speeds. Motor drivers with field-oriented control would be great for the benefits of high efficiency and accurate motor control.

In a motor that uses a trapezoidal PWM, the MOSFET bridge switching must occur in a precise sequence for the BLDC motor to operate efficiently. The sequence is determined by the relative positions of the rotor's magnet pairs and the stator's winding. A three-phase BLDC motor requires a six-step commutation sequence to complete one electrical cycle. The number of mechanical revolutions per electrical cycle is determined by the number of pairs of magnets on the rotor. A rotor comprised of two pairs of magnets requires two electrical cycles to spin one revolution.

Figure 21 shows a typical arrangement of BLDC motor driver diagram with three Hall-effect sensors (A, B and C indicating rotor position). This shows a microchip microcontroller, an insulated-gate bipolar transistor (IGBT) driver, and a three-phase inverter with six MOSFETs (metal oxide semiconductor field effect transistors) used for high-power switching. The microcontroller, is mirrored by the IGBT driver, sends PWM (pulse width modulated) signals that drives the average voltage and current to the coils, which corresponds to motor speed and torque (Digi-Key).

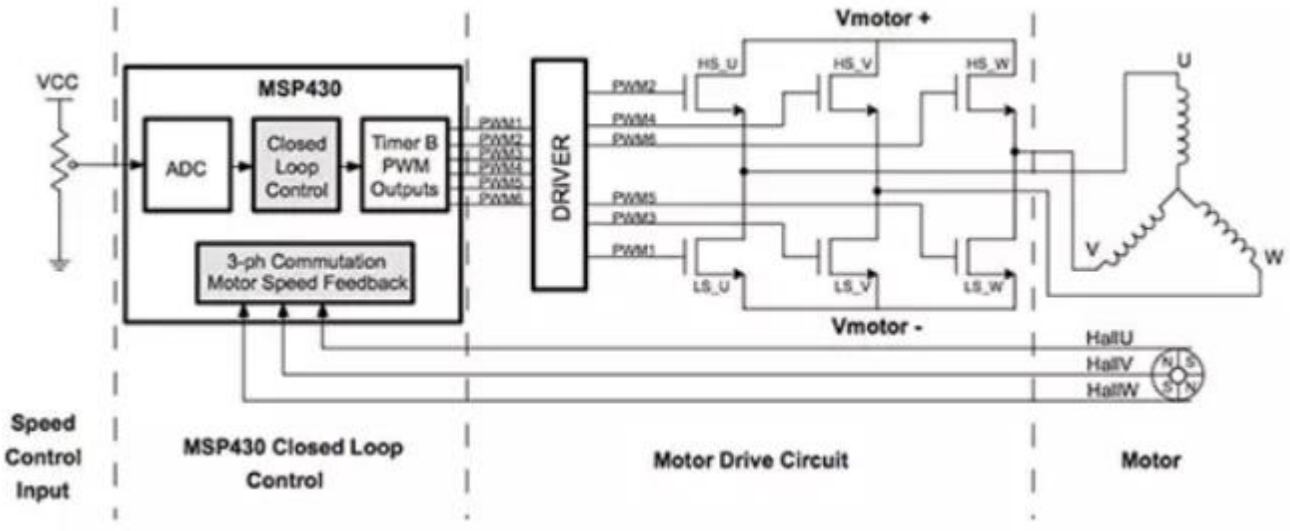

Figure 21: BLDC power supply control system using an 8-bit microcontroller

Although it is possible to build and implement motor control by directly reading the Hall-Effect sensors and provide a corresponding PWM by programming a microcontroller, to meet the real time constraint and achieve high efficiency, this feat would be difficult with an undergraduate knowledge base. There are motor drivers available in the market that interprets the signals from the Hall-Effect sensors and sends corresponding PWM signal to actuate the motor. Implementing this motor driver would require a step-down converter to power the microcontroller, typically less than 5 V, plus other system requirements. Gate driver control and fault handling as well as timing and control logic would need to be implemented as well.

Texas Instruments makes a three-phase pre-drive DRV8301 that steps down the voltage, can drive three-phase brushless motor, and provide PWM signals. This pre-driver can sink 2.3A and source 1.7A of current. It requires a single power supply with an input voltage of 8 - 60 V. Likewise, ON Semiconductor’s LB11696V adds discrete transistors at the output of the circuits which controls the desired output power and is used for large BLDC motor applications like air conditioners and water heaters. Allegro Microsystems's A4915 three-phase MOSFET driver operates as a pre-driver for MOSFETs in a half-bridge configuration. Microchip also offers a pre-driver MCP8025 for a six-power MOSFET bridge for small sensor less units and integrates a step-down switching regulator to power an external controller. TI offers DRV8398 which takes inputs from three Hall-effect sensors directly and can be used without an additional microcontroller. Also, developments in position sensor technology such as Analog Devices' ADA4571 provide angle sensors and signal conditioners that offer greater precision than Hall-effect sensors.

3.6.3 Electronics Assembly

As the number and complexity of the electronic components increases, it is important to design these components in a way that facilitates assembly and servicing by the team. It is also critical

to consider environmental hazards to the components, such as dust and liquid. An enclosure will be used to protect the electronics from dust and liquid and will serve to keep it clean. Vibrations will also have to be considered. Soldered electrical connections lose reliability when introduced to vibrations and movement. Soldering will also complicate the timely separation of electrical components. Thus, connections between electrical systems should avoid soldering where possible. A printed circuit board will make the circuit compact and improve the electrical connections by eliminating wires thus diminishing noise. Electrical connectors should extend from the motor driver, allowing them to be easily networked together with the motor, battery, and driver inputs.

3.7 Drivetrain

The drivetrain is a source of significant losses, so careful selection and design of drivetrain system is important to the efficiency of the whole system. Sources of power loss include bearing friction, vibration, sliding power loss, and rolling power loss. The drivetrain options include gearbox, chain and sprocket, belt and pulley, and direct drive. Preliminary research on each system and power loss is summarized below.

3.7.1 Power Transfer and Efficiency

As mentioned above the three main mechanisms for power transfer are gears, belts, and chains. Research was made into the efficiency factors for each of these transfer modes and is summarized below to aid in the design of this project and serve as a reference for improvements to the e-car in years to come.

Considering gear drivetrains, the paper “Comparison of Spur Gear Efficiency Prediction Methods” provides an overview of five efficiency models which could be used to determine the efficiency of using a gear system in E-Ventus. The authors, Anderson and Loewenthal, provide an in-depth analysis of five gear efficiency models compared to three gear systems tested with pitch line velocities from 1 to 20 m/s and loading factors from 17 to 1600 with jet lubricated ground gears. Their own model found that rolling losses become significant at higher speeds. It also provided a good prediction for the losses from no-load up to full-load across all gear geometries tested. The other four models underperformed the Anderson-Loewenthal model for loaded and unloaded testing. This model can be used in our project as a versatile tool for predicting the efficiency of a gear train used in the electric car. The model equations for rolling, sliding, and drag (or windage) losses can be found in Appendix F.

Analysis for the efficiency of chain systems is well presented in “Effects of Frictional Loss on Bicycle Chain Drive Efficiency” by J. B. Spicer et.al. The conclusion of the paper is that chain system efficiency is increased with increased tooth ratio and increased with chain tension. From their experimental data they found a 2-5% increase when the sprocket ratio was doubled. Chain tension yield an efficiency increase of 18% when the chain tension was quadrupled. No significant effect was found by lubricant used. The maximum efficiency calculated was 98.6%. The table summary of chain configurations and resulting efficiencies from their report can be found in Appendix G.

Belt versus chain efficiencies are addressed in the M.R. Bolton et al Senior Project design paper and demonstrate that the kinetic energy usage is increased by 428% based on past years analysis of energy usage comparison. According to “Tech Talk: Belt vs. Chain Drive” the advantage of a belt drive system in bicycles is the low maintenance and long life due to reduced wear and stretch. Belt systems also require no lubrication. Chain stretch is a main cause of loss of efficiency in chain drive systems. A downside to belts is that they cannot be ‘unlinked’ to allow the belt to pass through closed loops.

Friction Facts conducted a test on the efficiency of belt and chain drives using a Gates Carbon Drive System and a traditional single speed chain drive. Their efficiency test determined that frictional losses for a belt system were 34.6% greater than the roller chain when tested with manufacture specified preloads. This paper determined that for low load applications such as bicycles, chains are a more efficient power transmission system. This is because the pretension for belts is much higher than for chains and as the load on the system increases the pretension on the belt must also increase which drives up the frictional losses. However, the paper demonstrated that if the preload tension remains below 40 lbf then the belt drive system loses less energy to friction. Comparing load rough estimates from the vehicle system dynamics and approximate motor specifications, the loads are low enough that the belt tension would not significantly reduce the efficiency. From initial calculations using a 1:7 reduction the loads would be from 17 lbf- 34 lbf. The tension needed according to the Gates Carbon drive belt specifications would be below the 40 lbf tension where the belt system efficiency dips below the chain system efficiency from Friction Facts Efficiency Test.

Based on friction test by Friction Facts, the comparison of efficiency between belts and chains may come down to the pretension on the system.

From the 2017 Preliminary Design Report for the Supermileage vehicle, considerations for lubrication were made for the first time with the conclusion that efficient lubricants are often dry lubricants such as paraffin wax (Bolton). The testing performed by Friction Facts quoted in the paper shows that the four most efficient bike chain lubricants were led by paraffin wax, followed by three light or dry Teflon lubricants.

The 2018 internal combustion engine car used a Teflon spray on lubricant and a graphite spray on lubricant on the sprocket. These methods proved to have sufficient durability, maintaining their coating through each competition run.

3.7.2 Clutch and Hub

Considering the drivers experience, the question of motor jerk was researched with reference to the use of clutches and idle modes for an electric vehicle. Research papers by Xiong and Gu as well as Batra demonstrate that anti-jerk methodologies are more efficiently addressed by the motor controller and other electrical systems rather than a clutch in electric vehicle systems. Thus, our system tuned the motor jerk using software rather than including extra mechanical systems.

Building from past designs, the Odyssey hub performed well in the internal combustion car, Delamina, in the 2018 competition. However, the Odyssey hubs are only compatible with rim brakes, which in Delamina was a cause of much design and packaging grief, requiring custom manufactured caliper arms mounted under the engine plate. The old Ventus car ran with Phil hubs and a disk brake which was a much cleaner design, using off the shelf components. However, the 2017 Phil rear hub was not reliable and needed replacement.

Two important considerations for a new hub were instantaneous engagement and low bearing friction. The two main constructions of bicycle wheel hubs are sprag clutch and pawl. The pawl uses an armature and toothed ring shown on the left in Figure 22. This is the most common configuration for hubs. The speed of engagement depends on the number of teeth and pawls. The teeth engage with the spring-loaded pawls to provide torque transfer and pawls slide over the teeth without engaging when freewheeling. The sprag clutch shown on the right in Figure 22 uses figure eight shaped cams which provide instantaneous engagement and torque transfer but also minimal friction when freewheeling.

Figure 22. Comparison of Pawl and Sprag Clutch Mechanisms

According to a study by Duke University on wheel drag, the coefficient of friction of Sprag clutch hubs by Onyx was 25% less than the lowest pawl hub coefficient of friction (.135 vs .181). Onyx also uses ceramic bearings standard in all their hubs. They also have a variety of hubs available, offering single speed with disk brake and spline profile for the sprocket. Other high-quality hub manufacturers considered were Carbon-Ti, Extra-Lite, and Chris King.

3.7.3 Motor plate and Assembly

To begin understanding the requirement for the motor plate a search through the Supermileage archives was conducted to learn from past designs. From an internal memo by past president Eli Rogers, important factors for the design of the motor plate were determined to be:

- built-in alignment
- modular and removable

- adaptable to use with dynamometer
- minimized components
- easily accessible engine bolts
- built-in brake and chain guard mounts
- standardized bolt sizes and limiting the number of types used
- minimizing the needed number of tools required for removal

From the 2016 Drivetrain Senior Project Preliminary Design Review additional factors were

- having a single piece drivetrain mount
- isolating engine vibration
- mounting the engine lower
- testing for optimal gear ratio and proper chain tension.

Each of these items have been considered in the design for the motor plate and assembly of the drivetrain system. More detailed descriptions of the design choices are discussed in Design Development section and use with dynamometer is discussed in Chassis Dynamometer section.

Research into mechanical systems layout included drawing inspiration from competitors' design reports. The Michigan Technological University Supermileage Design Report shows the new rear end design which features a one-piece motor plate and wheel dropout design. The chain tension is supplied by a moveable motor mount instead of traditional horizontal dropouts with tensioners. This design allowed the team to drop three pounds from their previous year's model by reducing bulky dropouts and tensioner.

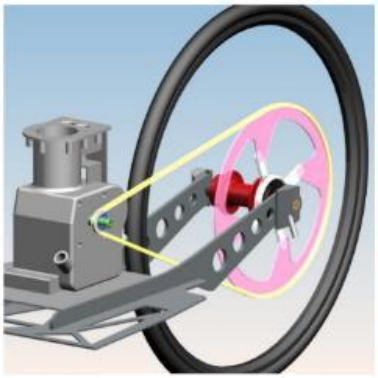

Figure 23. Michigan Technological University 2015 design for single piece motor plate, frame and wheel dropouts.

4 Project Objectives

The Cal Poly Supermileage Vehicle team desired to expand the scope of "Learn by Doing" opportunities that the club provides to Cal Poly students by adding an electric powered vehicle platform. This provides them with opportunities to learn about electric vehicles, collaborate as a dynamic team to overcome engineering challenges, and represent the university at Shell's Eco-Marathon.

The scope of our project includes research and development of the following subsystems:

- Electric motor
- Motor controller
    - PCB design
    - Programming
- Drivetrain design
- Powertrain Packaging
    - Motor Plate
    - Motor Mount
- Battery and power management specifications
- Fabrication and mounting of components to chassis

The components were designed and selected to maximize system efficiency, since the competition is judged by energy consumption. Figure 24 shows the boundary diagram for our scope of work.

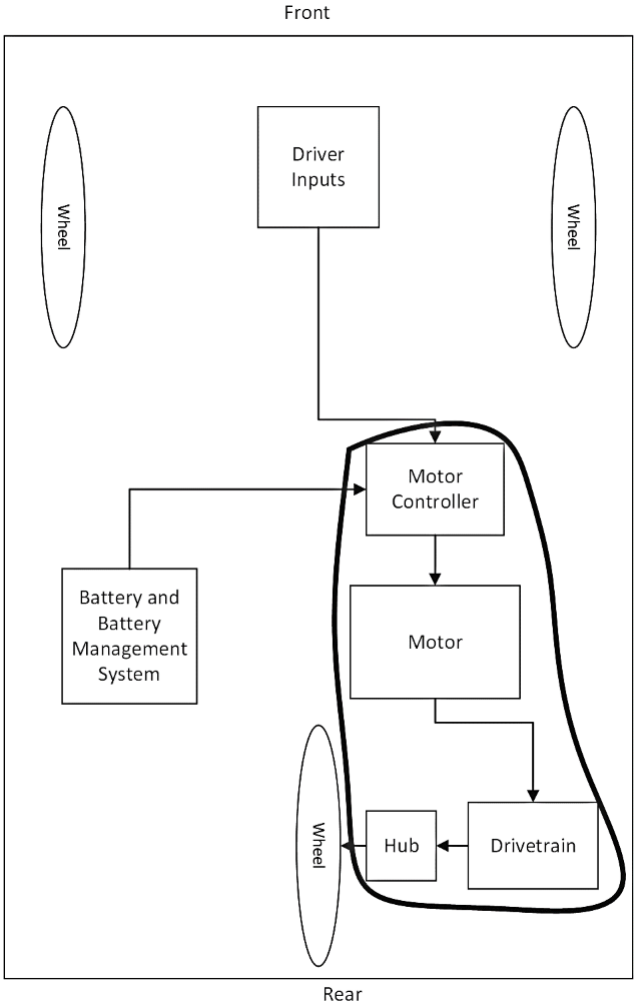

Figure 24: Boundary Diagram

4.1 Technical Specifications and Targets

The technical specifications shown in Table 4 are determined from testing data taken on the Ventus Internal Combustion Engine car in 2017 and the Shell-Eco Marathon rules. Since the chassis and tires remain the same due to time and space restrictions, the starting torque and rolling resistance for the previous vehicle are assumed to be an acceptable starting point for design.

Table 4: Technical Specifications

Spec. #	Parameter Description		Target (units)	Tolerance	Risk	Compliance
1	Battery Voltage	Safety Requirement	48 V nominal; 60 V peak	Max	L	A/T
2	Battery Capacity	Safety Requirement	1kWh	Max	L	A/T
3	Energy Usage For One Lap	Energy Requirement	250 mi/kWh	Minimum	H	A/T
4	Average Speed	Speed Requirement	15 mph	Avg	L	A/T
5	Powertrain Weight	Target to minimize	25 lbf	Max	H	A/T
6	Rear Wheel and Power Train Alignment	Target to minimize	Planar Alignment: 0.0 in Angular Alignment: 0.0	Planar: ± 0.05 Axial: ± 1°	H	A/I
7	Rear Hatch Packaging Space	Fixed Parameter	35 x 19 x 13 in	Max	L	A/I
8	Ruggedness: Impact	Motor plate mounts	220 lbf	± 25 lbf	M	A
9	Grade Climb	Power Requirement	5% grade	± 0.5%	L	A/T
10	Ruggedness: Weather		Rain safe		L	T
11	Budget		$3000	± $1000	M	I

Risk addresses the difficulty in meeting the specified target. Risk can include aspects that are hard to test accurately or require tight tolerances. High risk specifications are discussed in later sections 2.1.1 through 2.1.3.

- H – High
- M - Medium
- L – Low

Compliance refers to the method by which the design requirement can be verified. Specification compliance can be established through models and analysis, rigorous testing or simply visual inspection. Some specifications can also be verified through a combination of methods.

- A – Analysis
- I – Inspection
- S – Similarity to established design
- T - Testing

4.1.1 Energy Usage

The distance per power target was one of the highest risk parameters because it relies on the proper function of the whole system particularly efficiency and weight. Because these two parameters are dependent on each other, they were the most important factors to analyze, test and iterate for design solutions.

4.1.2 Power Train Weight

The power train weight includes all the components contained in the scope of this project. Staying below the target of 25 lbs depended on the motor and battery mainly as they are the heaviest components. Lithium ion batteries can be quite heavy as well as the brushless motors. Staying within this limitation required careful record keeping of projected weights for even the smallest components and creative manufacturing to reduce material.

4.1.3 Rear Wheel and Power Train Alignment

The system alignment with the rear wheel is a significant contributor to drivetrain efficiency as well as power train reliability. These alignment goals were informed by two sources, the Diamond Chain Maintenance Guide and the success of the 2018 Cal Poly Supermileage Drivetrain (CPSMD) senior project team. CPSMD used an alignment of .02 in planar alignment and 1° angular alignment. These metrics proved successful in creating a reliable system. Because of the lower sprocket ratio in this project, the Diamond Chain Maintenance Guide was referenced to determine the alignment tolerances for a lower reduction ratio. Based on their alignment equations for a center distance of 15 inches the tolerance for planar alignment is 0.05 inches. We continued to use CPSMD's angular tolerance of 1°. The alignment between the two sprockets was determined by using a CMM to measure the deviation of the small sprocket from the plane which the larger sprocket defines. This plane could not exceed a 0.05 in offset or 1° angle rotation.

4.2 Quality Function Deployment (QFD)

Based on the customer needs and the engineering specifications discussed above, a QFD was created to organize and explore the relationships among the many facets of this project. From the comparison of customer needs and engineering specifications the most important features for the design are reliability, efficiency, system cost, and ruggedness.

Reliability was based on all components working together to create a system that yields consistent results during testing and competition. This included the need to have reliable alignment that can hold its tolerances over many disassembles and reassembles by the Supermileage team. Efficiency was based on all components minimally attributing to power losses so that overall system power consumption is 250 miles/kWh. This customer need was the most important for customer satisfaction since the team's goal was to place within the top four teams. System cost was important because the project must remain realistic within the $4,000 budget. This limit was important because it required us to consider the necessary quality of each component in order to allocate money wisely according to how they contribute to the efficiency goal. For example, the motor was a high efficiency and high cost item.

Lastly, ruggedness was necessary to ensure that the design can survive normal operating conditions as well as the harsh environment of competition where crashed cars and roll overs are a threat to complete each trial. This was essential to ensure that the design survives for further optimization by the team in future years. The QFD chart is attached in Appendix H and provides more detailed comparison of the customer needs and qualifications.

5 Project Management

5.1 Design Process

The design process for this project followed a concurrent engineering process. This means that while we were determining our design, we also tested our manufacturing processes and material selections for design feasibility.

Our process was split up by three quarters. The first quarter was background research on the problem. We investigated different solutions for electric vehicle powertrain components that would match our specifications and made early design decisions. The main components included the motor, controller, drivetrain, wheel hubs, and mounting plate.

The second quarter focused on component selection and detailed design, including outlining of manufacturing and testing plans.

During the third and final quarter, the team finished manufacturing and conducted tests to verify the design. This ensured our solution met the outlined engineering specifications and verified that the powertrain was ready to be integrated into the club vehicle for future participation at the Shell Eco Marathon's electric vehicle competition.

5.2 Team Roles

The subsystems and key activities have been broken down and given responsibility to each team member. Besides individual roles, the entire team assisted where needed and assembled the powertrain.

Erik Alvarado managed the electrical circuits design, motor controller interfacing and wiring components. He was responsible for creating schematics and board layouts for manufacturing the

motor controller printed circuit board (PCB). He was also in charge of purchasing and managing the bill of material for all electronic components for the PCB.

Clarisa Howe led the mechanical system component design, analysis, and manufacturing. Her responsibilities included organizing prototyping and overall project scheduling. Clarisa oversaw procuring all pertinent parts and materials. She was responsible for quoting and purchasing the parts and necessary materials that were needed to manufacture all the mechanical parts. She was also responsible for ensuring that the materials and parts were procured in a timely manner so that all manufacturing could begin immediately. This process included updating the bill of materials, pushing quotes through to purchase orders and keeping track of all parts and materials during and upon delivery.

Chris McLaughlin was head of analysis and simulation of powertrain and vehicle dynamics, he led mechatronics programming and software development for motor control. He also led the testing and verification for simulation and motor performance, including testing the powertrain on the chassis dynamometer.

Enyi Liang oversaw motor manufacturer research and motor sizing and was responsible for mechanical validation and components integration to vehicle. Enyi was the main line of communication with the sponsor and all third parties. She facilitated meetings with the sponsor and informed them of all pertinent information as needed. She was also responsible for keeping all group members up to date with communications with the sponsor and facilitating all general communication between the team.

6 Project Design

The following section discusses overall vehicle simulation, motor selection, drivetrain and power electronic design.

6.1 System Dynamics and Motor

From motor background research, we chose to power the Supermileage car with a BLDC motor since it is efficient, high torque and light weight. In this section, we discuss our system parameters, DC motor modeling and motor selection.

6.1.1 System Parameters

Vehicle speed requirements were the driving factor in motor selection. This coupled with road grade determined the necessary motor torque and rotational speed. Given a wheel diameter of 19.5 inches, track length of 6.5 miles, the car needed to average 15 mph to finish the track in the required 26 minutes. Choosing a vehicle design operating speeds between 10 to 27 mph corresponded to 172 to 465 RPM at the wheel. For wheel speed analysis, see Appendix I. DC motors operate near 1800 RPM to 3600 RPM and are most efficient operating around 85% to 90% of their max speed; therefore, direct drive was impractical in this case. For operating speeds to be within the efficiency point of the motor a mechanism for speed reduction was necessary. Therefore, the motor speed at the efficiency point was not a constraint in choosing a motor.

Starting torque and torque requirement for the motor was based on the testing data and simulation from Chad Bickel's thesis paper on the modified 2.2 horsepower Yamaha engine used in the Supermileage ICE car. The starting torque determined from Bickel's research was approximately 0.25 ft-lbs. Further engine testing data was acquired from the engine lab on Cal Poly's campus by Dorian Caps. According to Caps findings the current Yamaha engine provides a torque of about 2.5 ft-lbf from 2500 RPM to 6500 RPM. This vehicle used a reduction ratio of 12 so these ICE motor rpms correspond to 208-542 RPM at the wheel. Since our cars desired operating point is 172-465 RPM at the wheel our set point falls within this data and provides a reasonable estimate of needed torque. These two parameters created a good gauge on starting torque for this project's vehicle simulation in MATLAB, which is discussed in Vehicle Model and Simulation.

Based on vehicle simulation, the required torque is 1.2 ft-lbs for the hill climb. Since this fell below the 2.5 ft-lbs in Chads research, the greater torque requirement was used as the more conservative design parameter. Below, in Table 5, the system requirements are summarized for selecting a motor.

Table 5. Summary of System Parameters for Motor Selection

Parameter	Units	Value
Starting Torque (motor)	ft-lbf	0.25
Operating Point Torque (motor)	ft-lbs	2.5
Torque for 5% grade	Ft-lbs	1.2
Average Wheel Speed	RPM	465
Wheel Diameter	inches	19.5

6.1.2 DC Motor Modeling

Electric motors have maximum current drawn and high torque when starting, yet torque output from the motor deceases drastically at high rotational speeds. Characterizing performance of a motor for a given torque constant K_t and back EMF constant K_b requires an understanding of motor dynamics which is given in brief below.

A typical DC brushed motor can be modeled as a circuit as shown in Figure 25 with supply voltage, V_a, resistor, r_a, and inductance, L_a, back-EMF, e_b, motor torque output, T_e, speed, ω_r, and armature current, i_a. (Kwang, 3).

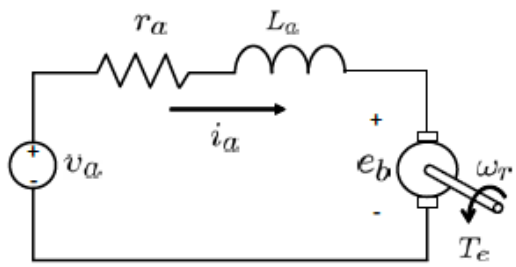

Figure 25. Equivalent circuit for a DC motor

According to Faraday's Law, the back-EMF e_b induced in a rotating coil with a magnetic field and flux changes is equal to:

$$e_b = K_b \omega_r \qquad \text{Equation 1}$$

Where K_b is the back-EMF constant and angular speed of the motor ω_r is linearly proportional to the back-EMF generated.

The torque and current relationship of a DC motor is developed based on current passing through the conductor in a magnetic field, Lorentz force is developed on the conductor. The magnetic torque is expressed as

$$T_e = K_t i_a, \qquad \text{Equation 2}$$

Applying Kirchhoff's Voltage Law to the circuit shown in Figure 25, the following relationships are obtained.

$$v_a = r_a i_a + L_a \frac{di_a}{dt} + e_b, \qquad \text{Equation 3}$$

$$e_b = K_b \omega_r, \qquad \text{Equation 4}$$

$$T_e = K_t i_a \qquad \text{Equation 5}$$

Note that electric power of the motor is voltage times current and is equal to $e_b i_a$, which is equal to mechanical power torque times angular speed of the rotor $T_e \omega_r$; neglecting power loss due to armature resistance, $T_e \omega_r = e_b i_a$. power relationship is obtained by rearranging Equation 1 and 2. Therefore, $K_t = K_b$ is obtained. K_t and K_b are constant motor parameters for a given motor based on its internal coils and winding construction. These two constants are used to guide motor selection.

6.1.3 Motor Selection

Between DC brush and brushless DC (BLDC) motor, BLDC tends to be more efficient, low maintenance, and quieter because of the elimination of the rotating commutator on the shaft of the motor. Thus, BLDC can be made smaller and lighter than brushed DC for the same power rating.

In “AC Motor Control and Electric Vehicle Application” by Kwang Hee Nam, he claims permanent magnet (PM) motors (both BLDC and PMSM) have low inertia due to the high strength electric field generated which allow reduction of the motor volume. Further, since there is no copper loss of the secondary winding, the PM motors have higher efficiency than induction motors. However, the PMSM motors require a more complex programming in the motor controller to provide efficient commutation.

There are several options for BLDC motors, we investigated options for hub motors designed for e-bikes and external BLDC motors used in industrial applications. A hub motor contains an internal planetary gear set, allowing compact packaging and simplified assembly. Mechanical losses are approximately 3% per stage and hub motors can have multiple stages. Additionally, hub motors have a fixed gear ratio, so there was less flexibility for selecting gear ratios in existing hub motor products. Furthermore, having heavy un-sprung mass attached directly to the wheel requires more energy to spin to the same speed as a regular wheel in dynamics response. Hub motors are specific to wheel size and have limited quality options for a 20-inch rim.

In contrast external BLDC motors can be the size of a 16 oz water bottle for similar power ratings as hub motors. They can also be used with a chain drive system to reach efficiencies of 98%. There are many manufacturers and options in BLDC motors as well.

Appendix J outlines our selection criterions for weight, packaging, programming and control, efficiency, dynamic response, source and cost for the motor. Although the PMSM motor scores the highest for its good dynamic response and highest efficiency out of all motors, we decided to choose a BLDC motor, which scored only two points below, for programing ease. Research on implementation of a PMSM was performed before final selection of a BLDC motor. This selection better suited the scope and timeline of this project. A BLDC also offered good efficiency, flexible gear reduction, enormous selection of suppliers and required less expensive Hall-Effect Sensors for positional feedback.

6.1.3.1 Preliminary Motor Selection

As many motor manufacturers provide *Kt* and *Kv* values rather than experimental testing data, these values were used to estimate motor characteristic curves. The following three motors were selected for consideration based on *Kt* and *Kv* values. A DC brushed motor model was used to approximate stall torque and no-load speed, which gave us torque and speed relationships, stall torque values, and maximum power which are populated below in Table 6.

Table 6. DC Motor Selection for PDR

Turnigy SK3 149 Kv 6374			Turnigy Mulstar 9235 100 Kv			Heinzmann PMS 080 F		
V dc =	44	Volts	V dc =	45	Volts	V dc =	24	Volts
Kt	0.06	Nm/A	Kt	0.1	Nm/A	Kt	0.064	Nm/A
Kv	149	RPM/V	Kv	100	RPM/V	Kv	226.76	RPM/V
I max	70	A	I max	57	A	I max	78	A
Pmax = 0.25(w_max*Tstall)	769	W	Pmax = 0.25(w_max*Tstall)	641	W	Pmax = 0.25(w_max*Tstall)	711.2	W
w_max = V*Kv	6556	RPM	w_max = V*Kv	4500	RPM	w_max = V*Kv	5442	RPM
Tstall = Imax*Kt	4.48	Nm	Tstall = Imax*Kt	5.44	Nm	Tstall = Imax*Kt	4.992	Nm
Reduction, e	7		Reduction, e	7		Reduction, e	7	
T new stall = e* Tstall	31.4	Nm	T new stall = e* Tstall	38.1	Nm	T new stall = e* Tstall	34.94	Nm
w_max_new = w_max/e	937	RPM	w_max_new = w_max/e	643	RPM	w_max_new = w_max/e	777.5	RPM

Road load data was taken from Chad Bickel's thesis for the ICE vehicle that used the same chassis. A second order polynomial curve fit of experimental data from coast down test was plotted against vehicle speed. Torque versus speed curves of the above motors running at a steady state speed of 25 mph was also plotted. An overlay of both these plots is shown in Figure 26.

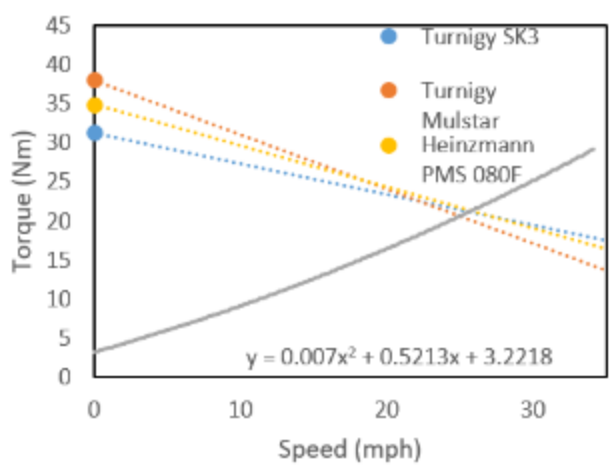

Figure 26. Torque versus Vehicle Speed for Motor Selection for PDR

Note that Turnigy Sk3 and Turnigy Mulstar are BLDC motor are powered by nominal DC voltage at 44V and 45V, while Heinzmann PMS 080F is a PMSM motor powered by nominal DC voltage at 24V. The max power rating for the three motors is average out to be 650 W with a difference of about +/- 50W.

We chose to reject the ideas of using the Hobby King brand Turnigy motors due to their inconsistent quality and unreliability. The Heinzmann PMS080F motor was used for drivetrain design for PDR. However, Heinzmann is a German motor manufacturer and we could not get a hold of the manufacturer or distributor to determine pricing or lead time. This led us to seek other options for our final motor selection.

6.1.3.2 Final Motor Selection

In our final design, we chose to use a BLY343D-48V-3200 BLDC motor from Anaheim Automation, which is a US manufacturer that provided good technical support and had the motor in stock resulting a shorter lead time. The motor also had shown promising results from the simulation. The BLY343 characteristics are shown in Table 7 and manufacturers motor curves can be found in Appendix K.

The motor has an internal Hall-Effect sensor for 3-phase current feedback and a rotary encoder mounted on the back shaft. The Hall-Effect sensors are used to improve the starting performance of the motor by detecting the shaft position. An encoder, ENC-AMT112Q, utilizes differential line driver and has resolution up to 4000 pulse per revolution (PPR). The pulses captured by the encoder are sent to a quadruple differential line receiver, and encoder counts are sent to the microcontroller. The presence of the encoder will allow future teams to use greater position control on the motor for more efficient commutation in future iterations of the powertrain.

Table 7: BLY343D-48V-3200 Motor Specifications

Property	Value
Coil Resistance(ohm)	0.11
Inductance(mH)	0.17
Ki (N*m/A) [oz-in/A]	0.14 [20.39]
Ke (V/kRPM)	10.61
Simulated Energy Usage (W hr)	31

Using the brushed DC model in the simulation, characteristic curve of BLY343 running off nominal 48V battery supply was obtained. The motor simulation was fed into a simulation loop using a track profile obtained from RaceCapture to simulate energy consumption. The simulation was run at various gear ratios, results are shown in Figure 27.

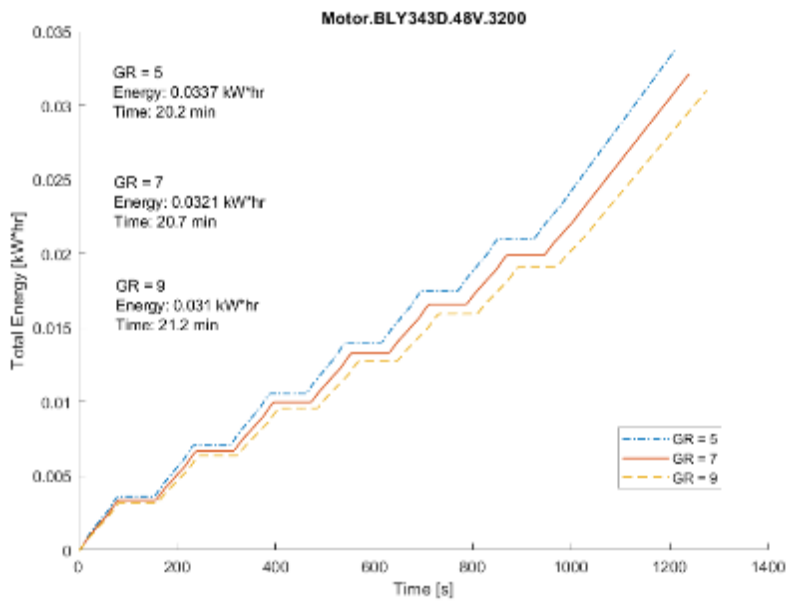

Figure 27. BLY343D simulated with different gear ratios

The simulation showed that larger gear ratios improved efficiency and decreased the maximum amperage of the battery. We selected a ratio of 9:1 to improve efficiency while not adding too much inertia to the drivetrain.

6.2 Motor Mount

Based on the selection of the BLY343 motor, a motor mount design was developed to control alignment. The design for the motor mount addressed concerns from previous years that alignment needed to be built into the components, components needed to be minimized, and standard bolts needed to be used for easy assembly/disassembly. Based on the lower vibration of the electric motor it was decided that vibration isolation in the motor mount would not be necessary for the e-car.

In order to ensure effective alignment, the proper use of locating pins was researched. From both last year's drivetrain senior project and product information from Misumiusa, it was determined that the best solution for locating the motor mount on the motor plate was using two locating pins, one with a round head and the other with a diamond head. The round pin holds precision location and the diamond pin holds angular placement. The diamond head prevent binding when small misalignment is present and provides better assembly.

The design of the motor mount is shown below in Figure 28. The mount was designed to be milled from a block of aluminum to provide good geometric control and reduced weight. The motor mount base is positioned in front of the motor to allow other components such as the chain guard to use its surface for attachment. The single supporting arm on the right helps reduce deflection in the face. There could only be one supporting arm because the chain travels across the left side of the mount.

Figure 28. Final design of the motor mount for BLY343 motor

The BLY343 motor has four #10 holes in the face. The motor mount utilizes all four mounting holes to distribute the force from the chain. To maintain the position of the mount relative to the dropouts, two pins are press fit into the motor plate and fit into the holes on the motor mount outer edge. The locating pins used in the motor mount are a paired round and diamond head pin. The forces from the motor on the mounting screws was determined to be 181 lbs based on the motor weight and peak motor torque.

The four holes on the motor mount base are tapped for ¼ -20 bolts so that the mount is bolted from the bottom of the motor plate into the motor mount eliminating nuts and washers. In order to minimize required components and standardize bolts for assembly, ¼-20 bolts are used whenever possible in all components. Bolt calculations from Shigley's Mechanical Engineering Design were used to determine the loading on the bolts and ensure they were under their yield point. The MATLAB script used to determine the loading factors is given in Appendix L.

Bending calculation were also performed to determine the total deflection due to loading and motor weight on the mount face. The calculations can be found at the end of Appendix L. From these calculations we determined that a face thickness of 0.35 inches would limit deflection to 0.001 inches. This was insignificant considering that perpendicularity tolerance was 0.0125 inches for the face to the base. Detail drawing of the motor mount are available in Appendix M.

6.3 Drivetrain

The drivetrain for this project is defined as all the components for the mechanical propulsion system: chain, driven and driver sprockets, hub, and wheel dropouts. Drivetrain systems considered in the development of the design were gears, pulley and belt, and chain and sprocket. A more detailed discussion of these systems can be found in the Background.

The main concern with gears was the limited space to mount the motor between the wheel and the wall. When the chassis body was measured it was clear that the narrow back cavity of the E-Ventus chassis was not well suited for gear applications. The use of a more complicated gearbox that would allow the motor to be mounted in front of the wheel would introduce an unacceptable level of mechanical losses. Therefore, due to space limitations a gear system on E-Ventus was not feasible this year.

The comparison between belt drive and chain drive came down to the kinetic energy required to accelerate them to operating conditions during a “burn and coast” driving profile. Findings by the senior project team last year, and validated by this team, conclude that the belt system required more energy at spin up as described in the drivetrain background. Therefore, if the drivetrain starts and stops many times on the track the belt system is a less efficient design. Since a “burn and coast” hybrid control strategy is being used in this first iteration e-car, the chain drive was selected for its high efficiency and low rotational inertia.

The 2018 Cal Poly Supermileage drivetrain senior project (CPSMD) team performed extensive research and development to design a single stage chain drive that was reliable and robust. In past years, the team has struggled with throwing the chain in a single stage system. The resulting 2018 design for wheel dropouts, sprocket manufacturing, and alignment procedures proved successful in competition and these designs and methods are adopted in the 2019 E-Ventus drivetrain. Appropriate gear ratio and motor plate design are particular to this project and are discussed in following sections. Aspects of the 2018 CPSMD team design are summarized where their designs are adopted.

6.3.1 Preliminary Drivetrain Design

Determining the size of chain needed was the first design priority. To aid in the design process, the Chain Drive Design spreadsheet created by John Andrew was utilized along with hand calculations to size the chain. System parameters such as expected loads and sprocket dimensions were added and rated Hp and safety factors were calculated.

Based on design motor parameters a reduction of 4:1 to 7:1 was investigated to see what the sizing limitations might be for each. The rated power to design power ratio for the ANSI #25 and #35 chain were compared to see which had the better factor of safety.

The design horsepower was based on the max power from the Heinzmann motor selected for the preliminary design. This is a worst-case scenario as the system should never be run near its max power making this a conservative estimate. The rated horsepower is the smaller of the value determined from link strength limited power and roller bushing limited power as defined by Shigley's.

For a #25 chain the ratio of rated horsepower to design horsepower is 1.14. Since the factor of safety was not very high for the #25 chain, the same analysis was determined for a #35 chain. This resulted in a rated horsepower to design horsepower of 2.96. The weight tradeoff was considered to determine if the increased factor of safety would be worth selecting a larger chain.

The weight/foot increase of using a #35 chain was 233% jumping from 0.09 lb/ft to 0.21 lb/ft. This increases the chain weight from 0.4 lbs to 0.95 lbs. Considering that keeping the system under the 25 lb limit is a high-risk specification and the design horsepower is conservatively high for what the system is predicted to experience, the final decision was to keep the #25 chain for a chain and sprocket system.

Appendix N gives the parameters determined from the spreadsheet. The driven sprocket is denoted as an uppercase letter and the driver sprocket is denoted with a lowercase letter. In all cases the driver tooth number was 17 teeth. The minimum number of teeth for the driver was determined with the goal of reducing chordal action and optimizing center to center distance of the two sprockets according to chain design guidelines from Shigley's Mechanical Design and Tsubaki. Reducing chordal action was based on a motor speed at 3000 RPM. Chordal action causes excessive chain vibration due to teeth spacing and the polygonal path of the chain around the sprocket. This vibration decreases chain drive efficiency. For a set chain pitch, chordal action can be decreased by increasing the diameter of the smallest sprocket.

6.3.2 Final Drivetrain Design

Based on the selected BLY343-48V-3200 motor and power curves provided by the manufacture, a reduction of 9:1 would operate the motor in its optimal range at an average vehicle speed of 18 mph. Although the optimal driver sprocket was 17 teeth, the final design includes driving sprockets ranging from 14-21 teeth with a fixed driven sprocket of 135 teeth. This allows the reduction ratio to be varied from 6.4:1 to 9.6:1 by swapping out the driver sprocket to adapt to the track requirements. A summary of the final drivetrain design is given in Table 8.

Table 8. Summary of Drivetrain Selection

Specification	Value	Units
Chain Pitch	.25	Inches
Driver Sprocket	15	Teeth
Driven Sprocket	135	Teeth
Reduction Ratio	9	--
Center to Center	15.5	Inches
Hub	Onyx BMX Pro ISO HG	
Dropouts	Modified from CPSMD design	

6.3.2.1 The Hub

An efficient rear bike hub is an essential component that impacts the efficiency of our entire drivetrain system. Light weight, instantaneous engagement and almost silent coasting led us to select the Onyx BMX PRO ISO HG-110/10mm Bolt-on Rear Hub shown in Figure 29. As mentioned in the background this hub demonstrated 25% reduction in friction coefficient from market leading pawl-type hubs.

The bolt-on feature of this hub allows us to continue to use 2018 CPSMD senior project dropouts with modification to the thru-hole size from 14mm to 10mm with clearance fit. The hub also allows us to mount our sprocket with a standard Shimano Hyperglide spline profile which provides a simple and efficient solution to transfer power from the custom-made sprocket to the hub.

Figure 29.Onyx BMX 110/10mm Bolt-On Sprag Clutch Hub

Although manufacture information on torque rating was not available, a BMX rider would output much more torque than our motor’s stall torque and the torque transferred the wheel. Our current torque seen at the wheel is 60 Nm or 45 ft-lbs with assumed gear ratio of 10:1. A BMX rider weighing 160 lbs with a six-inch crank arm can produce 80 ft-lbs from their weight alone. Therefore, we are confident that the design of the hub is robust enough for our driving conditions.

6.3.2.2 The Sprockets

Because a #25 chain was chosen and a relatively large reduction ratio, the larger sprocket was not available as an off the shelf component and required custom manufacturing. The club has custom manufactured their own sprockets using water jet for the last three years with excellent results in tooth profile.

The driven sprocket design was utilized from last years' senior project and resized to have 135 teeth. The design is shown in Figure 30. The driver sprockets were stock items from McMaster Carr. Cut sheets for these components can be found in Appendix O.

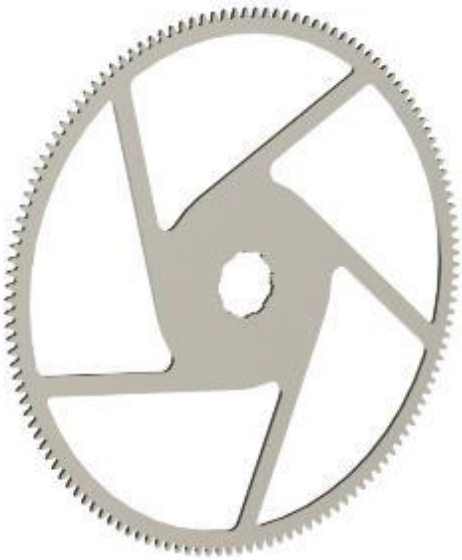

Figure 30. 135 tooth driven sprocket with spline

As can be seen in the figure above, the driven sprocket integrated with the hub through splines, providing excellent torque transfer. The sprocket spline tolerance specification from Onyx technical support is shown in Appendix P. The desired tolerance for a spline is bilateral +0.002/-0.000 inch. See drawing for the large sprocket in Appendix Q.

The center-to-center distance for the two sprockets is 15.5" due to packaging issues. Although chain design equations from Shigley's solved simultaneously for center distances and chain length suggested an optimal center to center distance of 11.03" our motor plate mock-up placed in the chassis showed that the chain angle would cause interference with the rear wheel well. We determined that increasing the center distance to 15.5 inches would remove chain interference and be the most economical solution. Center distance calculations using EES can be found in in Appendix R.

Considering chain vibration during operation, we determined that even with proper tensioning the chain could vary ¾" to 1" based on Diamond Chain Company installation and tensioning manuals.

6.3.2.3 Rear Dropouts

The dropout design by the senior project team last year proved to be a very robust and precise method of creating chain tension and hub support. Their design used an outer housing and an inner slide. The slide position was controlled along the length of the car by threaded rods and across the car by bolts that threaded into the hub axle. This allowed two axes of adjustment on the rear wheel which improved chain alignment. The figure below shows a rendering of their design. The wheel dropout was designed to be CNC machined out of 6061 aluminum. The bolt-on thru-hole size was changed from 14 mm to 10 mm. The original 7/8-24 hex nuts were sized down to ¾ -16 nuts to accommodate smaller bolts. The drawing for the new design is attached in Appendix S.

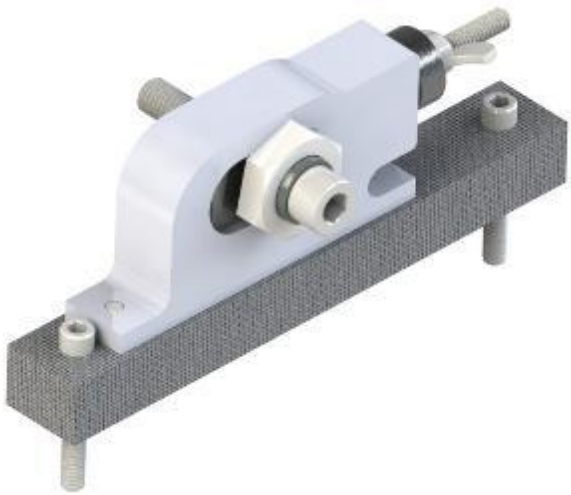

Figure 31. Updated dropout assembly on Gerolite insert

6.4 Motor Plate

Selection of a motor plate was determined on seven significant factors listed below in order of importance

1. Reliable drivetrain alignment
2. Reduce center of gravity of the vehicle
3. Lightweight
4. Structural strength and rigidity
5. Easy to assembly and disassembly
6. Manufacture feasibility
7. Ease of use with Supermileage dynamometer
8. Number of chassis mounts that would have to be replaced

The reliability of the drivetrain alignment means that after removal and reinstallation of the motor plate the drivetrain is precisely and accurately fixed into the same place in all three axes. Alignment should be set once during initial installation of the system.

The lower cars' center of gravity, the more stable the vehicle is during cornering. The speed at which we can take corners is important because having to brake reduces energy efficiency, or rolling the vehicle means disqualify.

Reduction in weight was always a consideration with every component in Supermileage. It must be made with the least amount of material possible without compromising the alignment reliability or the structural strength and rigidity. Lightweight and structural strength were a balancing act in this design.

Ease of assembly, allowing the motor plate to be easily taken in and out of the chassis, was another important factor for the design. The fewer pieces that must be put together, the easier and faster it is to assemble and disassemble.

Manufacturability was also important for the feasibility of the design. The more contours, the more difficult to hold tolerances and ensure structural strength. Failure points at joints were considered in each design.

This year the use of the Supermileage Club dynamometer was a huge advantage for testing the motor and drivetrain. The design had to be compatible with the dynamometer. This included maintaining alignment when taken from the chassis and mounted to the dynamometer.

The last consideration was how the current chassis would be altered based on the design. There were four motor plate mounting brackets in the chassis. The right front bracket was broken in a roll over two years ago. The back two brackets were positioned for mounting the axle and were structurally solid. Removing the back brackets was considered difficult and not preferred. The front brackets, with one already broken were considered only mildly difficult. The easiest solution for the motor plate brackets was to fix the one broken bracket.

6.4.1 Plate

The motor plate configuration underwent several design evolutions which is only be briefly discussed here before the final design is presented. The development of the drivetrain layout is shown in Figure 32. The image on the left shows the preliminary design which has arms that angles down from the axle to a flat plate were the large mass can be mounted low in the chassis body. The image on the right shows the final design using a bent plate which achieves the same goal of dropping the center of gravity for the assembly but keeps the wheel dropouts leveled. Not shown in the layouts are brake mounts, joule meter, controller board and electronics.

Preliminary design of Motor Plate

Final Version of Motor Plate

Figure 32. Evolution of motor plate design

6.4.2 Preliminary Motor Plate Design

The preliminary design for the motor plate is shown in the Figure 33 below.

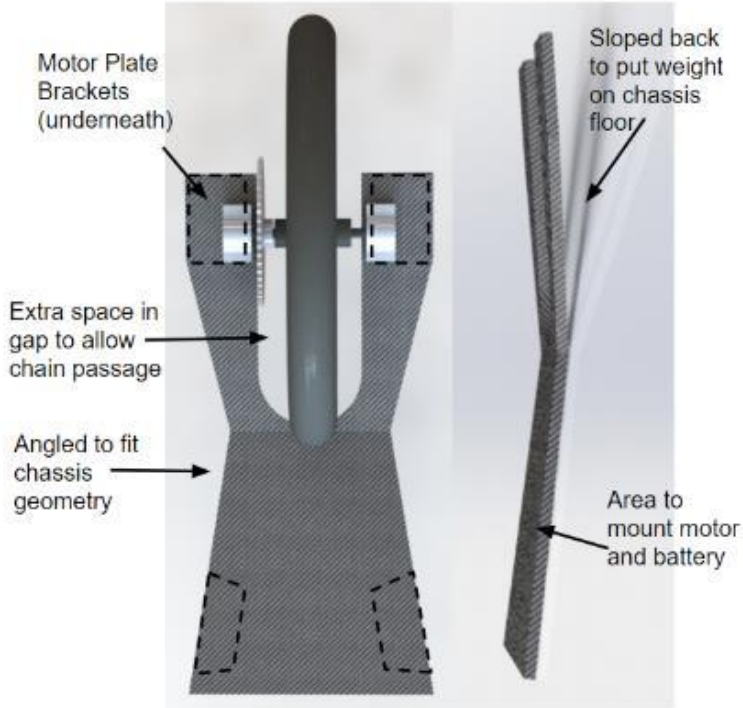

Figure 33. Preliminary design for the motor plate selected from eight potential concepts.

A prototyping workday was used to produce motor plate configurations out of cardboard. From the ideation session eight configurations were sketched up for comparison. The sketches and

weighted decision matrix are shown in Appendix T. The above list of eight specifications were the criteria against which the configurations were measured.

The concept that rated the highest was a one-piece plate slanted at the wheel down to the bottom of the chassis with a platform extending across the bottom. The concept design is shown in Figure 34.

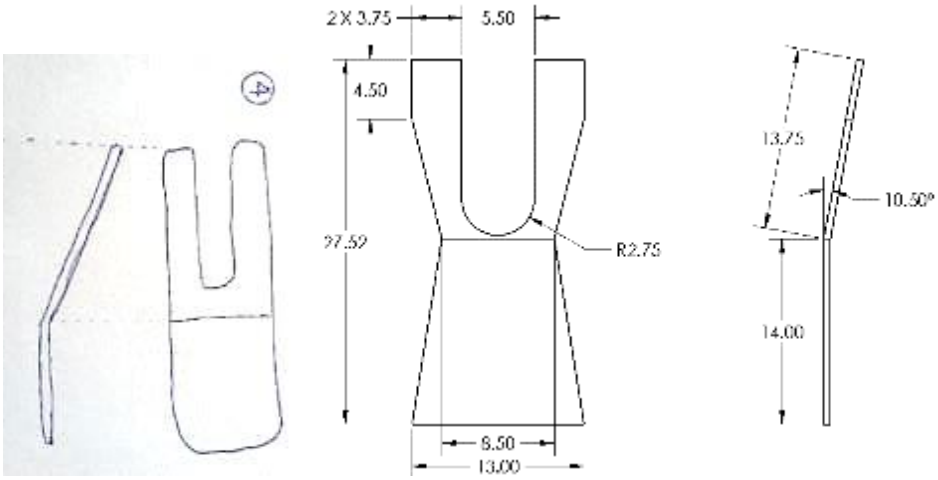

Figure 34. Highest rated idea for motor plate configuration, sketch and developed design

The selected design scored high in alignment reliability because it was one piece that holds the wheel axle, driven sprocket, motor, and driving sprocket along one rigid body. Once the wheel dropouts and the motor mount are aligned removing the motor plate would not move the alignment of the drivetrain.

The design also attempted to bring the bulk of the drivetrain weight further down in the car by having a flat plate at the chassis bottom where heavier components could be attached.

A carbon laminated balsa wood with potted inserts for all bolt points was also selected in this preliminary design. This was a reliable design that has been used for numerous years previously.

The manufacturing method selected post-bonded two flat pieces together to form the angle. However, because the slanted part would rest on the bottom of the chassis strength concerns at the thin arms was not critical. The thinnest areas shown in the diagram on the right would not be load bearing as the wheel and axle positioned at the end of the arms would be supported by the brackets underneath.

6.4.2.1 Inserts

In areas where high compression loads are expected it is necessary to have high strength inserts to take that loading. One area of high loading is the point of connection between the motor plate and the chassis. Last year’s senior project had developed a plate insert that provided load bearing and plate alignment. The alignment feature was excellent but the horizonal orientation of the bolts made assembly extremely difficult due to limited working space. Like the plate the inserts have gone through several iterations which are shown in Figure 35.

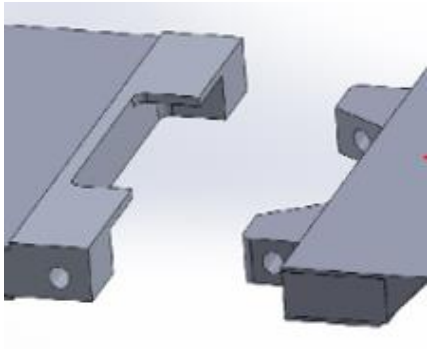

(a) The 2018 design

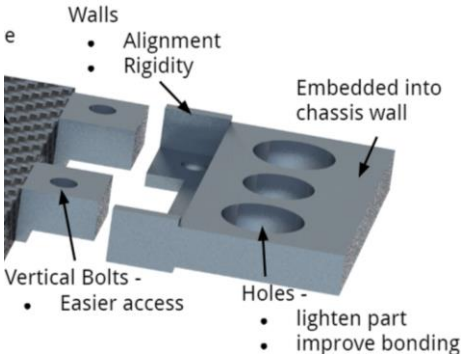

(b) Modification for vertical bolts (PDR)

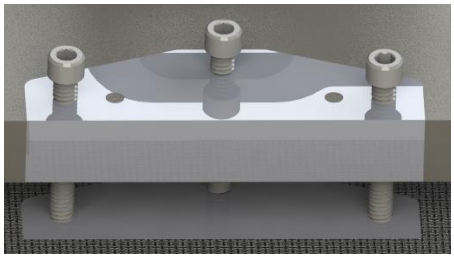

(c) Modification for simpler manufacturing (CDR)

(d) Final design: integrated with dropout

Figure 35. Evolution of motor plate inserts

The inserts pictured above are set into the plate core and chassis brackets during the layup and provide support for the compressive loads that these areas experience. Figure 35 (c) above uses paired round and diamond head locating pins for plate alignment instead of built in features like walls in order to simplify manufacturing. A three-hole pattern was determined for the inserts to reduce the hinging effect of only having two fasteners. An insert is mounted on each side of the axle and on the front of the motor plate.

In order to solidify the plate, insert design it was necessary to determine the forces that the wheel or chassis would transfer into the plate.

The forces on the motor plate were determined from worst case scenario at the axle when the car is braking, turning, and hitting a bump. This worst-case scenario was informed by the 2017 competition when the motor plate broke at the axle due to rough road conditions. The load analysis was performed using a custom MATLAB script which is provided in Appendix L. The inputs used in the script and the calculated forces are given in

Table 9 and Table 10.

Table 9. Force inputs to determine forces on motor plate.

Force	Value	Units
Braking Force	91.1	lbf
Turning Force	144	lbf
Bump Force	720	lbf
Car Weight	240	lbf
Drivetrain Weight	32	lbf

Table 10: Forces transmitted from axle to wheel dropouts

Force	Value	Units
F_x	103	lbf
F_y	518	lbf
Fz	0	lbf
F_Resultant	528	lbf

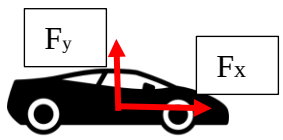

The forces at the dropouts were then used to determine the forces that the inserts in the motor plate would experience. These values are given in Table 11.

Table 11: Force on motor plate mount bolt

Force	Value	Units
Fx	111	lbf
Fy	1,157	lbf
Fz	0	lbf
F_Resultant	1162	lbf

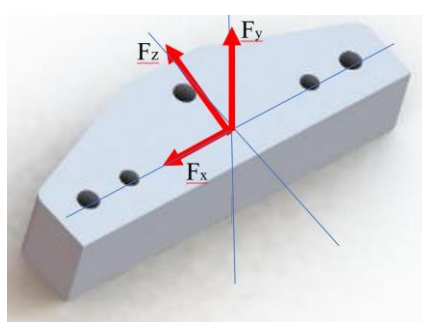

Figure 36. Insert for motor plate interface with chassis.

From the force calculations it was seen that having the plate bolt into the chassis at a significant distance from the dropout bolts created a huge moment about the plate bolts. Although the three-bolt pattern provided some counteraction, another solution needs to be developed.

6.4.3 Final Motor Plate Design

Moving into the final design, three changes were made to the motor plate design - the plate shape, and the core material, insert configuration.

During the preliminary review, concerns arose of changing wheel clearance and ride height when the chain was tensioned due to the slanted mounting of the dropouts. To address this issue, the design was changed so that the dropouts are mounted on a horizontal surface. This design is shown below in Figure 37. This design was selected to avoid changing the wheel height when tensioning the chain but allows the bulk of the drivetrain mass to be lowered to the chassis floor. In order to justify the more complicated manufacturing required for a multilevel plate, the location of the center of mass was compared for the proposed final design and the flat plate design used in past years.

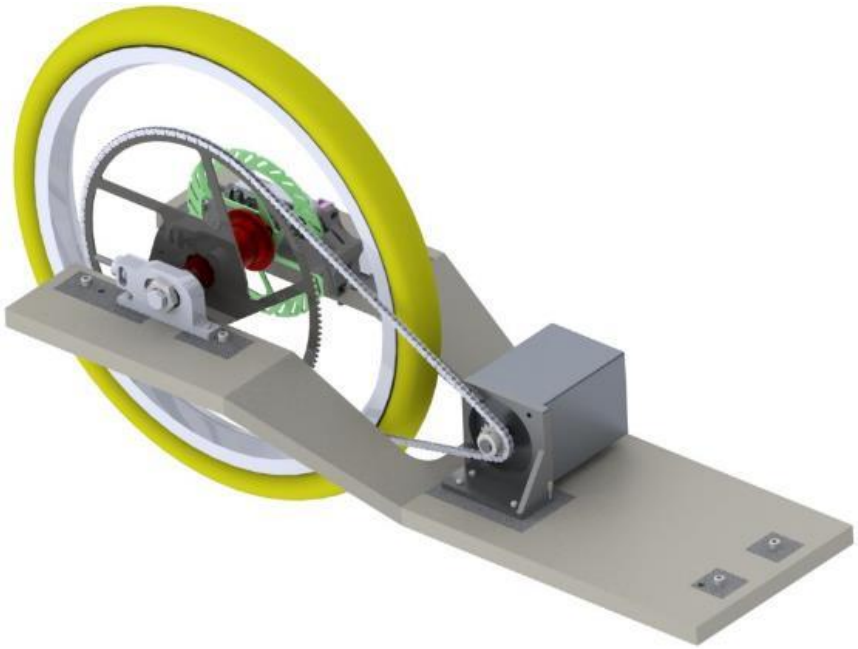

Figure 37. Final Mechanical Design Assembly

Using SolidWorks mass property feature, the center of gravity was found for a flat plate assembly and a sloped plate assembly. The possible assemblies are shown in Figure 38 through Figure 40. The difference between the arrangements center of gravity was 2.14 inches.

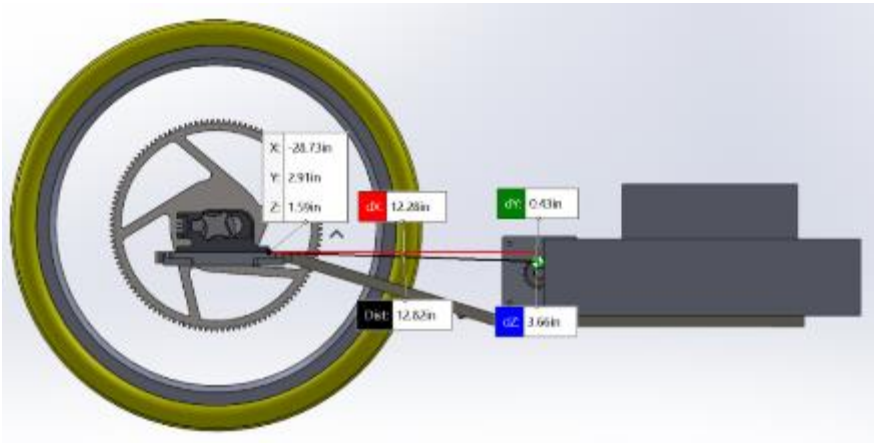

Figure 38. Center of mass evaluation on sloped plate using approximate shape and mass for battery, motor and motor controller.

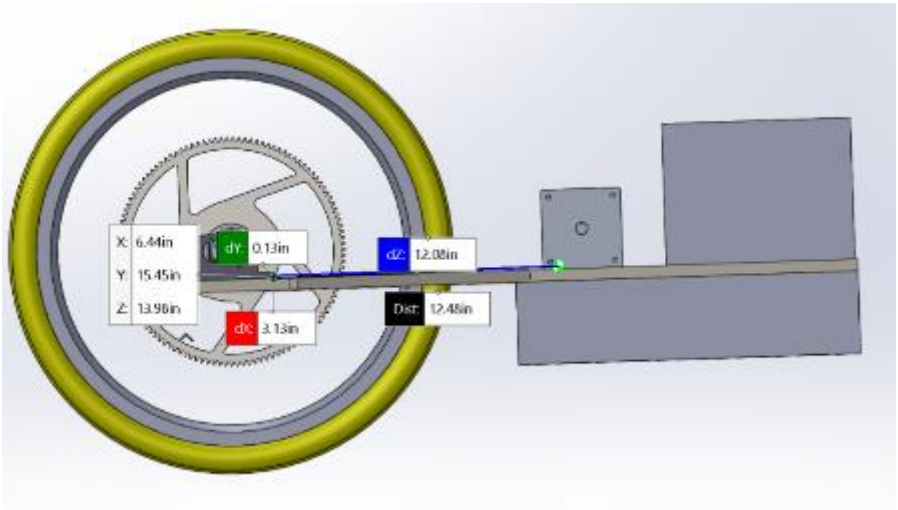

Figure 39. Center of mass evaluation for flat plate with battery mass mounted on bottom.

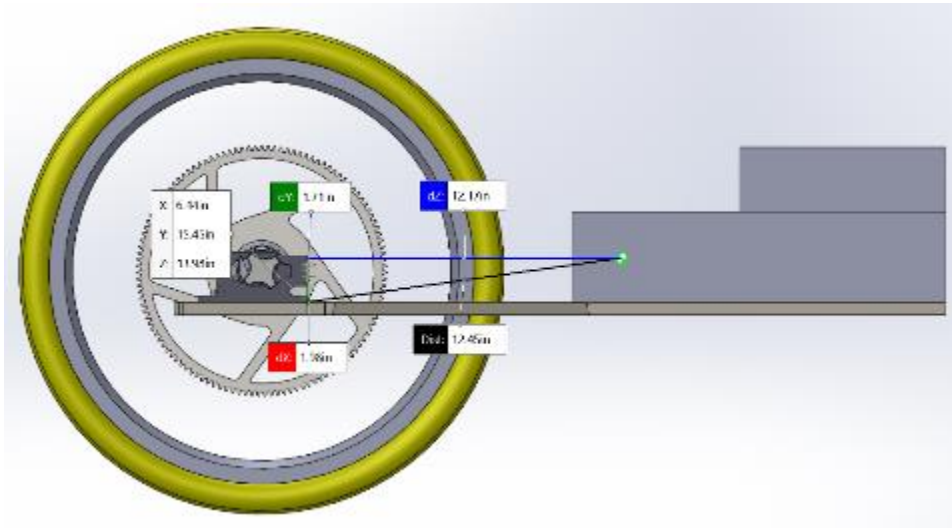

Figure 40.Center of mass evaluation with all masses mounted on top.

Considerations for the accessibility of the battery during competition required that the bottom mounted battery be rejected. During competition quick fixes are of utmost importance to get the car back out on the track. Requiring the engine plate to be removed to switch out a battery was not acceptable accesses. Between the flat plate and sloped plate configurations the center of gravity dropped 2 inches which was significant. The final design allowed the motor, battery, and controller to be mounted 3.7 inches below the wheel axle.

The increased manufacturing difficulty was considered worth the gain. The motor plate detailed drawings can be found in Appendix U.

The second change from the preliminary design was changing the core material from balsa wood to 2lb Polyisocyanurate. The polyisocyanurate at 2 lbs/f^3 provided an 80% weight reduction from balsa wood core at an average of 10 lbs/ ft^3. The motor plate core design is shown in Figure 41.

Figure 41. Single piece, two level motor plate, foam core with cutouts for inserts

The motor plate composition is a composite sandwich board, created in a single layup over a mold to increase the strength at the joints. The core material is 0.75 in 2-lb Polyisocyanurate

foam with LE Gerolite inserts at mounting points to take compressive loading. The motor plate is secured to the chassis through three brackets – two at the rear under the dropouts and one at the front behind the battery box.

6.4.3.1 Inserts

The second change to the plate design was eliminating the separate insert at the outer edge of the plate arms where the motor plate would bolt into the chassis. The bolts into the chassis have been moved in line with the bolts in the dropouts. This was done to eliminate the forces through a weaker foam core "channel" and reduce the moment on the motor plate bolts. The two arrangements are compared below in Figure 42 with force flow lines shown in red.

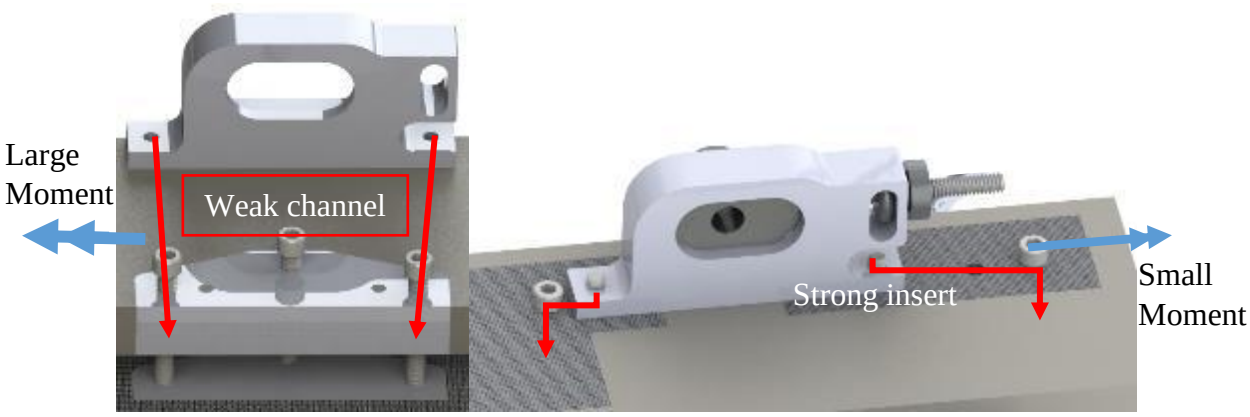

Figure 42. Comparison of preliminary and final design of motor plat bolt location (force flow shown in red)

A Gerolite LE material was selected because it provided a 40% weight saving per square inch over using aluminum. Built-in alignment is provided by paired round and diamond head pins on each side of the axle in line with the plate bolts and one diamond head pin at the front of the plate. The pins are press fit into the chassis brackets and fit into precision reamed holes in the inserts. Two locating pins are necessary for each arm in order to keep from flexing. Since the plate is so long one additional diamond head pins is added at the front of the motor plate to prevent rotation. These five location pins create a secure and repeatable alignment of the plate within the chassis.

6.5 Electrical Components

The electrical components were selected based on their reliability, compatibility, and their versatility. The first iteration of the motor controller featured a microcontroller, buck converters, high/low side gate drivers, and MOSFETs. The schematic in Figure 43 shows the connection of the first iteration of the board and how Phase A is generated by the high-side/low-side driver and the MOSFETs. The input signals from the microcontroller are modeled by repetitive square pulses labeled PWM_AL and PWM_AH. The second and third iteration of the board replace the buck converter and gate driver with Texas Instruments' integrated driver chip, the DRV8301.

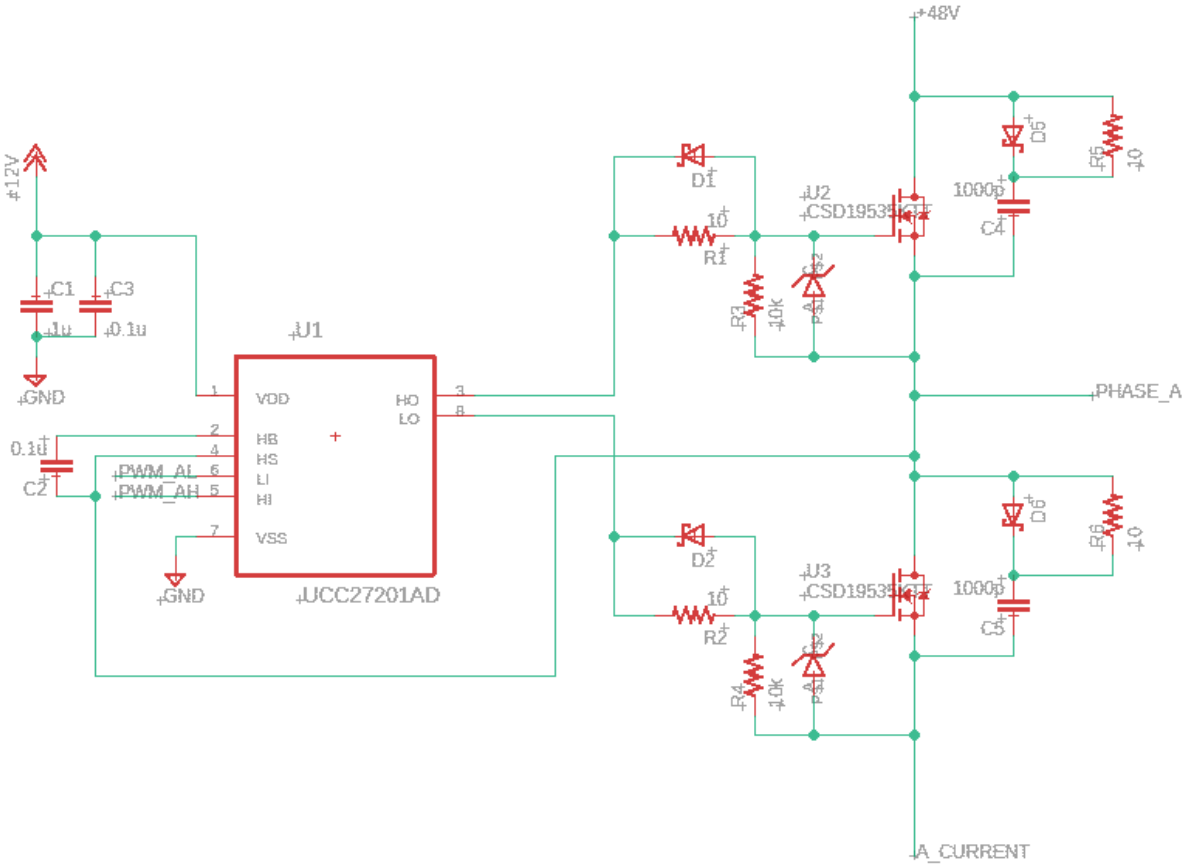

Figure 43: Driving Stage Schematic

6.5.1 Power MOSFETs

The CSD19535KTT power MOSFET is used for the half-bridge configuration shown in Figure 43. This MOSFET can operate at a max voltage of 100V. The battery should be at 48V nominal so this MOSFET is a robust option to drive the motor and improves its reliability during competition. It also has a source to drain diode which provides the component protection from ESD. When the motor is first switched on, it draws a large instantaneous current. According to the datasheet, the MOSFET can handle 197A of continuous current and about 400A of pulsed drain current.

The MOSFET is designed to minimize losses in power conversion applications. It has a low $R_{DS(on)}$ of 3.6mΩ which results in less power dissipation across it when it is conducting. It also has a typical gate to source threshold voltage ($V_{GS(th)}$) of 2.7V and a max V_{GS} of 20V. This means that supplying it with a voltage greater than the threshold turns it on and cause it to conduct current to the coils in the motor. By alternating the V_{GS} of the high-side and low-side MOSFETs using the driver, we can create a modulated sine wave to power the motor. There are three pairs of MOSFETs, one for each phase of the motor, each with its own high-side/low-side driver.

6.5.2 Gate Drivers

The first iteration of the design featured a high-side/low-side driver. This is a component that takes in two PWM signals from the microcontroller and outputs a modulated signal to each pair of power MOSFETS to produce the three phases to drive the motor. The device selected to drive the high and low sides of MOSFETs is the UCC27201A. This device has a high slew rate with 3A source and sink capability which allows it to rapidly charge and discharge the gates of the MOSFETs. To avoid having both MOSFETs on at the same time and prevent shoot through, a delay between the switching of the MOSFETs is needed. This delay is known as the dead time. During the dead time, the body diode of the off MOSFET provides a commutation path which contributes a fair amount to power losses. The driver has a precise 1ns delay between the rise and fall times to allow us to use the maximum PWM duty cycle which increases the efficiency of the driver. The driver also has under voltage lockout and overvoltage protection making it reliable and robust.

The second iteration of the board used TI's DRV8301 which has three integrated gate drivers and a buck converter to drop the voltage to 5 volts. The 5 volts is used to power the microcontroller. The third iteration used the same driver chip as the second iteration, but improvements were made in the shunt resistor selection and the PCB layout. The integrated chip in the second and third iteration are further discussed in a later section.

6.5.3 Microcontroller

For driver inputs, an analog signal like a potentiometer would allow us to vary the input voltage to adjust the speed of the motor. Using a potentiometer in the form of a dial or knob presents the driver with some difficulty as the driver would need one hand to adjust the speed while maintaining control of the vehicle with the other hand. For precise speed control, a joystick or slider type potentiometer may be the best option for an analog signal and the microcontroller may be programmed to receive either input.

A digital signal would also make it easier on the driver as they would only have a button to press which can easily be integrated into the steering wheel. After feedback from the SMV team, a digital option such as a switch seemed like a viable option. With a digital input, we would have to program the microcontroller to accelerate at a constant rate until the digital input was turned off at which point, the vehicle would begin to coast.

Table 12 provides five types of microcontroller specification that are good candidates for our application. Speed is essential to increase efficiency. A faster clock speed allows the microcontroller to read in the Hall Effect sensor data or analyze the back EMF quicker and provide more accurate timing for the PWM signals to the driver.

The benefits of the Teensy 3.2 are that it is the smallest out of all the microcontrollers; therefore, it may take up the least board space. The input and output voltages are about the same across the microcontrollers. The Teensy 3.2 also draws about four times less current than the Arduino Uno. Another benefit of the Teensy 3.2 is that it can be programmed using Arduino's software. This makes the programming simpler and allows easier integration of components made for the

Arduino. There are also many forums for help with Arduino projects which we can use for the Teensy.

More background research was performed, and the InstaSPIN-FOC enabled LaunchXL-F28069M from TI was selected as a viable option for microcontrollers. This launch pad supports sensor less and sensored control using either hall sensors or an encoder. TI also provides an extensive user guide to learn to operate the microcontroller. This microcontroller would be the best selection as it is meant to drive a motor and because of its versatility. Since it is capable of both sensor and sensor less control, it can be used to control a large selection of motors. The launch pad can measure the torque, speed, angles, and the flux from the motor. It also has additional pins available to use for driver inputs to control the motor and is coded in C using Code Composer Studio. There is also a Graphic User Interface (GUI) from TI to change different parameters to control the motor. This GUI also identifies the motor's ID to get information about its rated torque, speed, and other parameters. The GUI simplifies the tuning process once the motor is running. It does consumer slightly more power than the Teensy boards, but it has the potential to provide better and more reliable speed control to the motor.

Table 12. Microcontroller Specification Table

	Teensy 3.2	Teensy 3.5	Arduino Uno	Atmel XMEGA-A3BU	LAUNCHXL-F28027
Specification					
Speed	72 MHz	120 MHz	16MHz	12 MHz 1.6V 32 MHz 2.7V	60 MHz
Input Voltage	5V	5V	5 V	1.6-3.6	3.3V
Output Voltage	3.3V	3.3V	5V	TBD	4.6V(Max)
DC Current	10mA	10mA	40-50mA	TBD	20mA
Digital I/O	24	40	14	47	22
Analog Inputs	21	27	6	3	13
Size	1.4" x 0.7"	2.4" x 0.7"	2.7"x 2.1"	TBD	2.6" x 2.1"
Code Language	Arduino's C	Arduino's C	Arduino's C	TBD	C/C++
Cost	$24 (Amazon)	$32 (Amazon)	$20 (Amazon)	$30 (Digi-Key)	$17 (TI)

6.6 Design Challenges and Risks

Unforeseen challenges to the design laid out the previous section include long lead times for parts that must be ordered. Integrating our project with the club sub team projects has historically brought about many unforeseen challenges as system integration turns up design clashes. There are also many design hazards that arise with building an electric powered vehicle. A full list of hazards can be found in Appendix V.

6.7 Motor Controller

Schematic of motor controller are divided into four main parts. The connections to the Launchpad microcontroller and peripherals, feedback circuits, motor driver circuits, and the power circuits. The final schematics are shown in Appendix W. The microcontroller is attached

to the motor controller by four 20-pin headers. The unused pins on the microcontroller are still accessible on the top side and allow the club to test and interface new features in the future. Screw terminals are used for the driver interfaces, battery connections, and motor phases. The signals going into the microcontroller include the feedback signals for the sensor less calculations as well as signals from the driver inputs to control the motor.

The feedback circuits are used to measure the motor phase voltages and currents. The voltage feedback circuits are composed of voltage dividers to scale the three phase voltages to within the analog to digital converters (ADC) range of 0-3.3 Volts. The current feedback circuits are implemented with operational amplifiers. They are connected to the bottom of the low side MOSFETs for each of the three phases. The current sensing circuits scale the measured current to 0-3.3 Volts for the analog to digital converters. Since the measured current is an AC wave with positive and negative components, a 1.65 voltage reference is needed to shift the current within the ADC range. The voltage reference is implemented using a voltage divider from 3.3V to 1.65 V followed by an op amp as an impedance buffer.

The motor driver circuits consist of the DRV8301 driver IC and external MOSFETs. The MOSFETs used, the CSD19535 from Texas Instruments, were chosen due to their low $R_{DS\ (on)}$ and fast switching rate. The integrated chip contains the circuitry to drive the gates of all six MOSFETs. It requires a few external components to operate correctly. The DRV8301 also has two internal op amps that can be used for current feedback. Although we do not use these internal op amps, they are connected to pins on the launchpad in case future changes requires its use.

In the first revision without the DRV8301, the power circuits consisted of two buck converters to generate 12 V and 3.3V. The DRV8301 has an integrated buck converter and only requires an external inductor, diode, and capacitor to produce 5V from the supply. This eliminated the need to have two buck converters and simplified the design and layout. It also reduced the total number of components needed.

After the motor controller was fabricated, we tested it to characterize the thermal generation of the controller.

6.8 Chassis Dynamometer

The chassis dynamometer (dyno) was designed by a previous project to model the inertial properties of the Supermileage vehicle. However, the project was unfinished, and did not include a way to mount the vehicle, shielding of the inertial components, a data acquisition unit, or a test procedure. All these missing features were added by us in order to complete testing of our powertrain. The finished CAD for the mounting and safety assembly is shown in Figure 44.

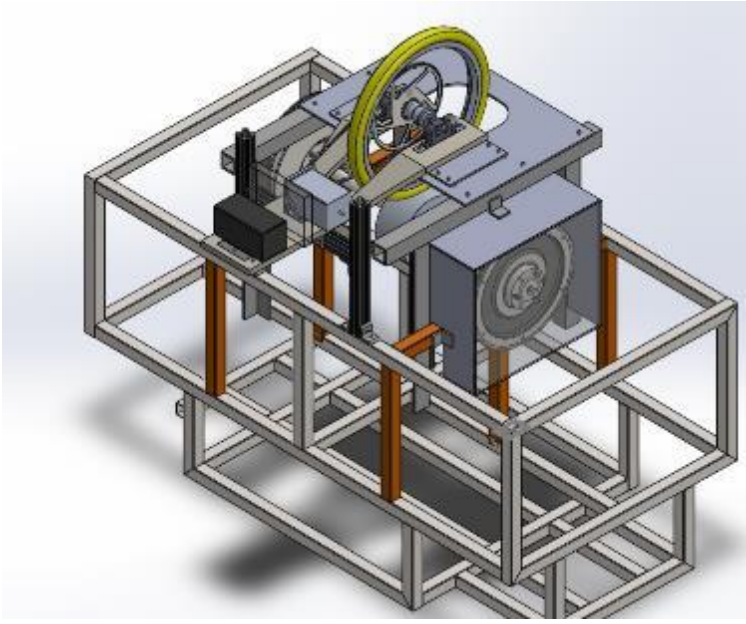

Figure 44: Chassis Dyno CAD Assembly

6.8.1 Dyno Mounting

The design allows the motor plates for either vehicle to be mounted and tested on the dyno. The mounting plate, seen in Figure 45, allows adjustment for various mounting widths, adjusting the horizontal distance between wheel dropouts, and the distance from the dropout mounting holes.

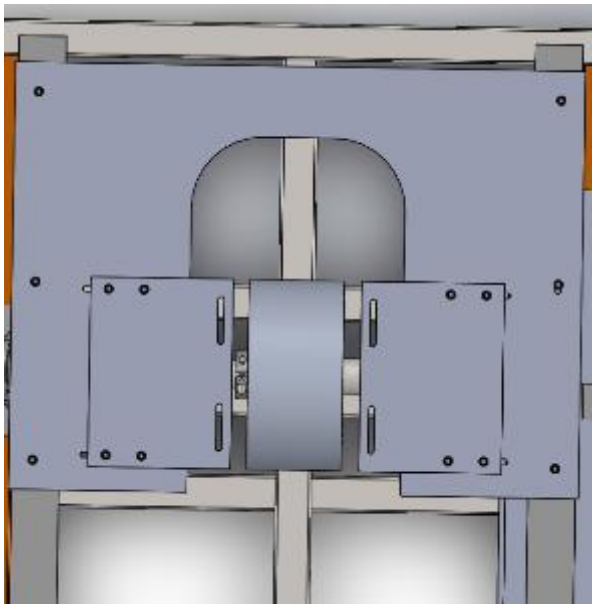

Figure 45: Chassis Dyno Mounting Plate

The mounting plate is fixed to the cart so that there is a gap between the surface of the mounting plate and the bottom of the motor plate. This ensures that the motor plate can be tightened down

until there is suitable force between the wheel and dyno to prevent slipping. The final distance is measured, and a spacer fills the space, enabling a quick installation for future tests.

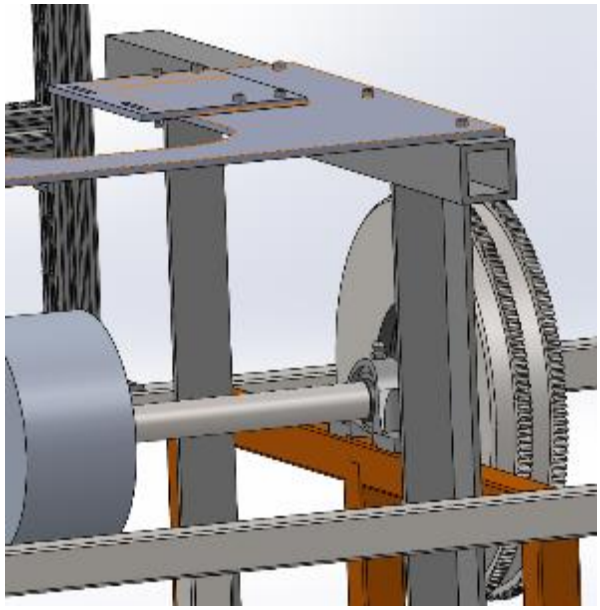

Figure 46: Chassis Dyno Mounting Plate Rear View

To allow multiple plate configurations (slanted versus flat), an adjustable stand was installed to support the bottom of the plate shown in Figure 47.

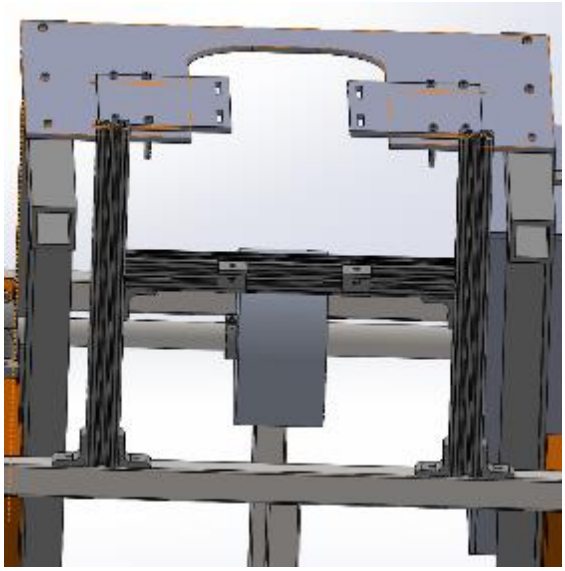

Figure 47: Powertrain Plate Support Stand

The powertrain was attached to the dyno shown in Figure 48. The motor plate was securely and safely fastened to the dyno while powertrain tests were conducted.

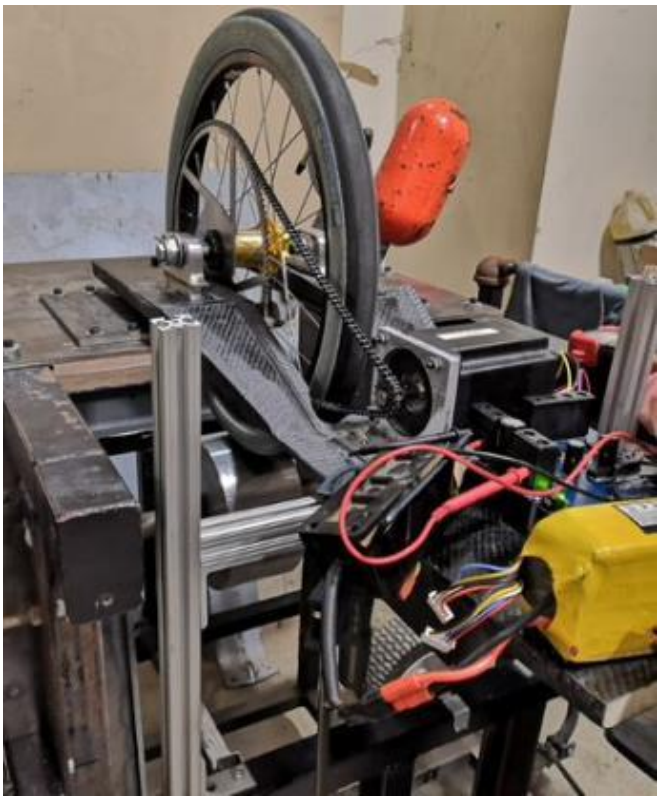

Figure 48: Chassis Dyno Mounting Actual Image

6.8.2 Dyno Safety

The shields were added to isolate the spinning gears shown in Figure 49. This prevents operators from contacting the gear during operation. The ¼” steel plates and brackets also add protection if the shaft fails. The operators should never stand in front of the dyno during operation.

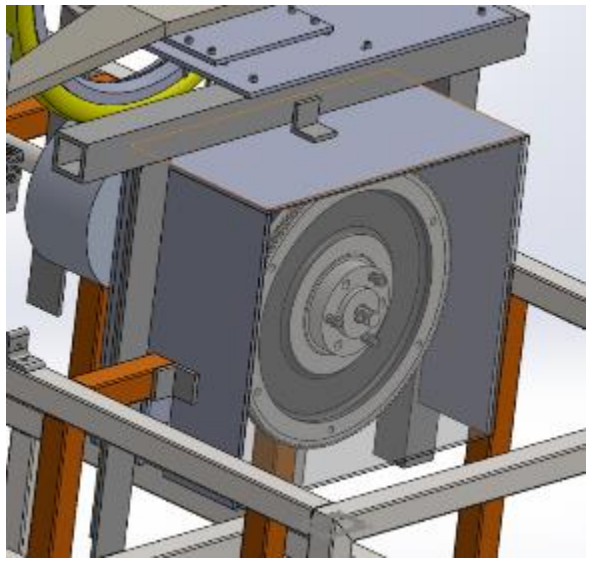

Figure 49: Dyno Safety Shield

6.8.3 Dyno DAQ

For a 200-tooth dyno gear, and a maximum vehicle speed of 30 mph, the tooth frequency is 4.2 kHz. Thus, we require sampling over 8 kHz to avoid antialiasing of the teeth. The tooth frequency is fast due to the 11:4 gear ratio between the tire and dyno mass. The rpm of the dyno gears is over twice the rpm of the wheel.

Dyno Speed Calculation

```
r_dyno = 4; % Dyno inertial wheel radius
mph = 30;   % Max vehicle speed
t = 200;    % Number of dyno gear teeth

ins = (mph*(1.467*12)); %Speed in inches per sec
rps_dyno = ins/r_dyno/(2*pi); % Rps of the dyno
kHz = t*rps_dyno/1000 %Required sensor frequency [kHz]
```

```
kHz = 4.2026
```

The Labjack T7 was donated to the club and acts as the data acquisition unit for the chassis dyno. It has a frequency input which reads up to 100 kHz. The sensor used is the Littelfuse 55505 Hall Effect Flange Mount Gear tooth Speed Sensor, which can measure up to 15 kHz. The DAQ configuration is saved to the club drive.

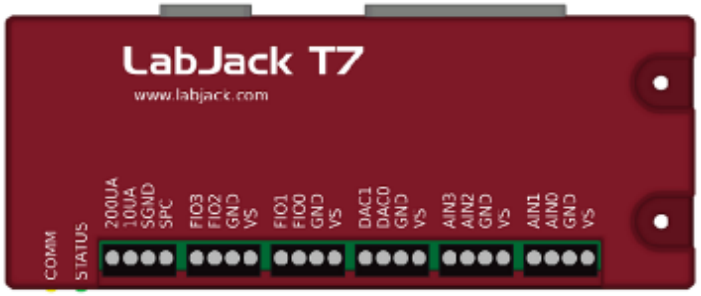

6.8.4 Dyno Test Procedure

See attached Appendix X for testing procedure on the chassis dyno.

6.9 Cost Breakdown

The total cost breakdowns of our selections are attached to the report. Appendix Y lists all the mechanical components, and Appendix Z lists all the electrical components.

6.9.1 Mechanical Breakdown

The mechanical system components can be separated into the drivetrain, motor, and the motor plate.

Table 13: Mechanical Cost Breakdown

System	Component	Cost
Drivetrain	#25 Chain	$78
	Sprockets	$177
	Rear Hub	$280
	Rear Dropouts	$73
	Total	**$608**
Motor	Motor	$550
	Mount	$9
	Total	**$559**
Plate	Plate Mold	$115
	Motor Plate	$245
	Total	**$360**
	System Total	**$1599**

6.9.2 Electrical Breakdown

The electrical system components can be separated into the PCB components, and the PCB.

Table 14: Electrical Cost Breakdown

System	Component	Cost
Components	ICs	-
	RLCs	
	FETs	
	Total	**$159**
PCB	Prototype (3x)	$180
	Final (2x)	$160
	Total	**$340**
	System Total	**$499**

Summary of mechanical and electrical budgets yield us a total of $2098, which is below the $3000 budget cap.

Manufacturing and assembly of all major parts, except for the motor and PCB, was done in house at the student machine shops in the Hanger and Mustang ’60. McMaster Cutsheets are attached in Appendix O.

7 Manufacturing

7.1 PCB Layout and Manufacturing

The PCB is a two-layer board consisting of a signals plane and a dedicated ground plane. Having a dedicated ground plane improves signal integrity and makes laying out the board easier. The board has four standoffs which enable it to easily mount to the case. For each component, we followed the datasheet’s recommended layout to improve thermal characteristics and ensure proper operation of the circuit. Most of the resistors and capacitors were surface mount components with a 0805 package. A few capacitors had a larger package to account for a higher voltage rating. The bulk capacitors selected for the input voltage were aluminum electrolytic capacitors, since they have the highest energy density per volume and smooth out high transient currents. The gate drivers, MOSFETs, and diodes were also surface mount.

Components were placed on the top of the PCB for ease of access, troubleshooting, and servicing. The bottom layer of the PCB was the dedicated ground plane. When laying out the board, we were careful not to introduce long traces on the bottom layer that would inadvertently split the ground plane. This would cause current loops in the ground plane and it would introduce noise into the feedback circuits. Special attention was placed on clearing up a free path from the input voltage terminals to the output terminals on the motor controller board. Decoupling capacitors were placed at the voltage inputs of the components and on the analog and digital grounds to suppress noise. Additional ground vias were placed in open spaces on the board to make the top and bottom ground plane more uniform and allow the top components to have a shorter path to ground, along with ground pads underneath components that draw high current and need good heat dissipation.

For external signals, we used screw terminals located next to the microcontroller. These screw terminals provided access to general-purpose input/output (GPIO) pins and analog-to-digital converter (ADC) pins on the microcontroller. There are also 5V, 3V, and ground terminals to power peripherals on the steering wheel.

7.1.1 Power Stage Layout

The power stage consists of three half-bridge configurations for three-phase. The placement of the MOSFET in this high power, high switching application for a motor drive is sensitive to the parasitic elements by non-ideal layouts as illustrated below.

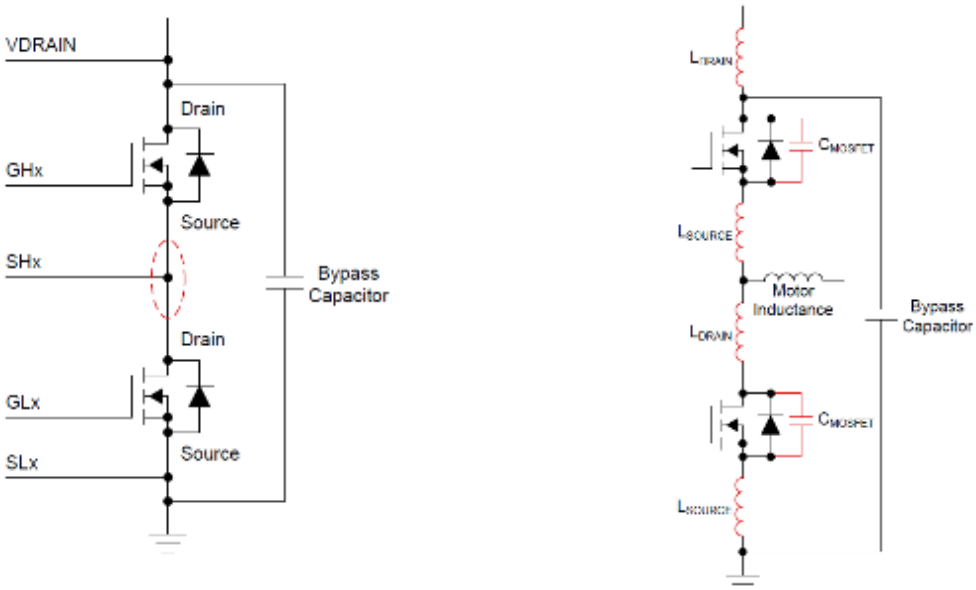

Ideal Half Bridge Configuration with SHx being Switching Node

Non-ideal Half Bridge with Parasitic Elements

Figure 50. Switch-Node Ringing Caused by Parasitic Elements

The switch-node that is connected to one phase of the motor is the connection between the source pin of the high-side MOSFET and drain pin of the low-side MOSFET. This node is most crucial to be routed in the half-bridge configuration due to the high frequency, high current nature of the signal. Like a non-ideal diode consumes power, the non-ideal parasitic elements such as unwanted inductance and capacitance are primary causes of a phenomenon called switch-node ringing.

Switch-node ringing is an LC oscillation that causes EMI and creates overshoot and undershoot voltages which can violate the absolute maximum ratings of the MOSFET drain-to-source voltage and gate pins. It can also decrease the efficiency of the power stage; therefore, it shall be addressed accordingly.

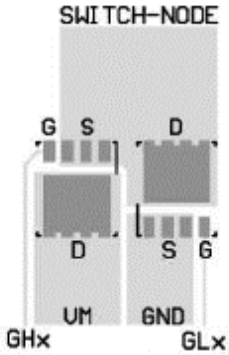

Figure 51. Switch Node Layout

The layout method we used to address the switch-node ringing issue is shown above. This layout minimizes the inductance between the source of the high-side MOSFET and the drain of the low-side MOSFET by minimizing the length and maximizing the width of the copper plane connection and choosing MOSFET package with minimum parasitic inductance.

7.1.2 PCB Manufacturing

After finalizing the design on Eagle, the design was sent to JLCPCB to get fabricated and components were ordered from Digi-Key. The board was assembled via reflow soldering. We were highly recommended to order a thin sheet of laser cut stencil as shown below for an extra $10 when ordering the board. It provided a huge benefit and saved time when spreading solder paste for the components.

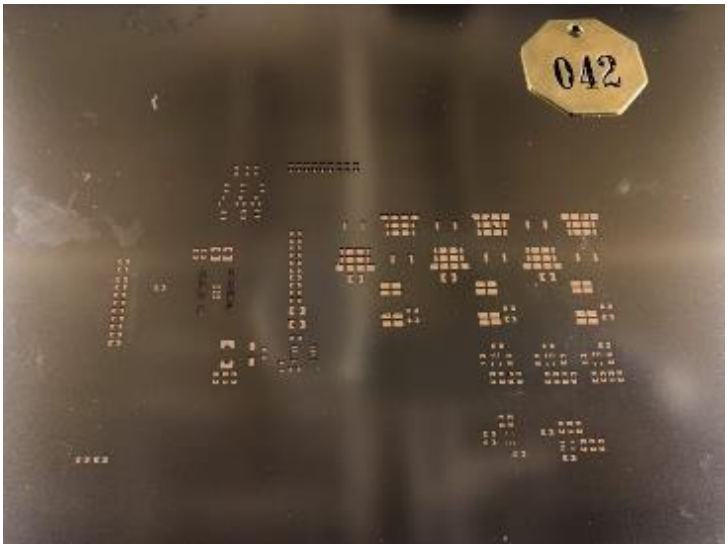

Figure 52. Laser Cut Stencil for Laying Solder Paste

The purchased stencil was already cut to expose the copper pads for surface mount components, allowing solder paste to be put precisely to location.

Figure 53. All Components Received and Organized by Values

After receiving all components and organizing them by values, with Eagle and BOM, we started making the board.

First, we overlapped the stencil on top of the backbone board to make the exposed cuts align perfectly with the copper pads on the board. Then we used the needle style solder paste and dropped the solder paste onto the exposed pads. Utilizing a small squeegee, we applied the solder paste evenly all over the board where components would be surface mounted. Then we removed the stencil from the board and checked for excessive or missing solder paste on the board.

Second, all surface mounted components were laid on the board. This process involved a pair of tweezers and a steady hand. A digital magnifying scope was used to visually inspect the component placement and ensure quality placement.

After all components were placed on the board, a reflow station was used to heat up the board. This process melted the solder paste so that the components would sit in place. Heat from the reflow station was applied in small circular patterns and the heat gun was kept a good distance away from the board to avoid damaging the PCB and the copper traces. The components under the heat gun vibrated and set in place.

Next, the through-hole components were soldered onto the board. Since the input and output voltage terminal blocks had bulky pins, more heat was needed to avoid having a cold solder joint which do not provide a quality connection. We also checked the porosity of the joints using the digital magnifying scope to ensure good connection to the board.

Lastly, a continuity check was performed with a multi-meter to ensure all components were soldered on properly and signal traces were intact.

7.1.3 Result of 3rd Iteration of Board

Over spring break, two boards of the third iteration design were assembled and tested as shown in Figure 54. There were over 250 components on a 5-inch by 7-inch board. With laser cut stencil layout, a digital magnifying scope, and a reflow station (borrowed from Jim Cullins), each board took 14 hours to build. The 3rd iteration motor controller board was tested with a power supply and was able to smoothly spin the unloaded motor up to 2100 RPM twice before it shut itself off. Four days were spent troubleshooting and attempting to fix issues before we ran out of time for competition.

Figure 54. Fabricated 3rd Iteration of Motor Controller Board

One definite challenge was working with the DRV8301 driver chip. This chip comes with 64-pin package that has a ground pad underneath the 0.75-in by 0.25-in chip. This made soldering difficult even with reflow, not to mention adding jumper wires. Additionally, vias were placed on the ground pad underneath the chip during board design to help with reflow soldering and heat dissipation. In the future, we recommend using a breakout board for this chip. Although it would add extra spacing and rooms to the board, it would allow swapping out this chip easily during debugging phases without the risk of damaging the rest of the board.

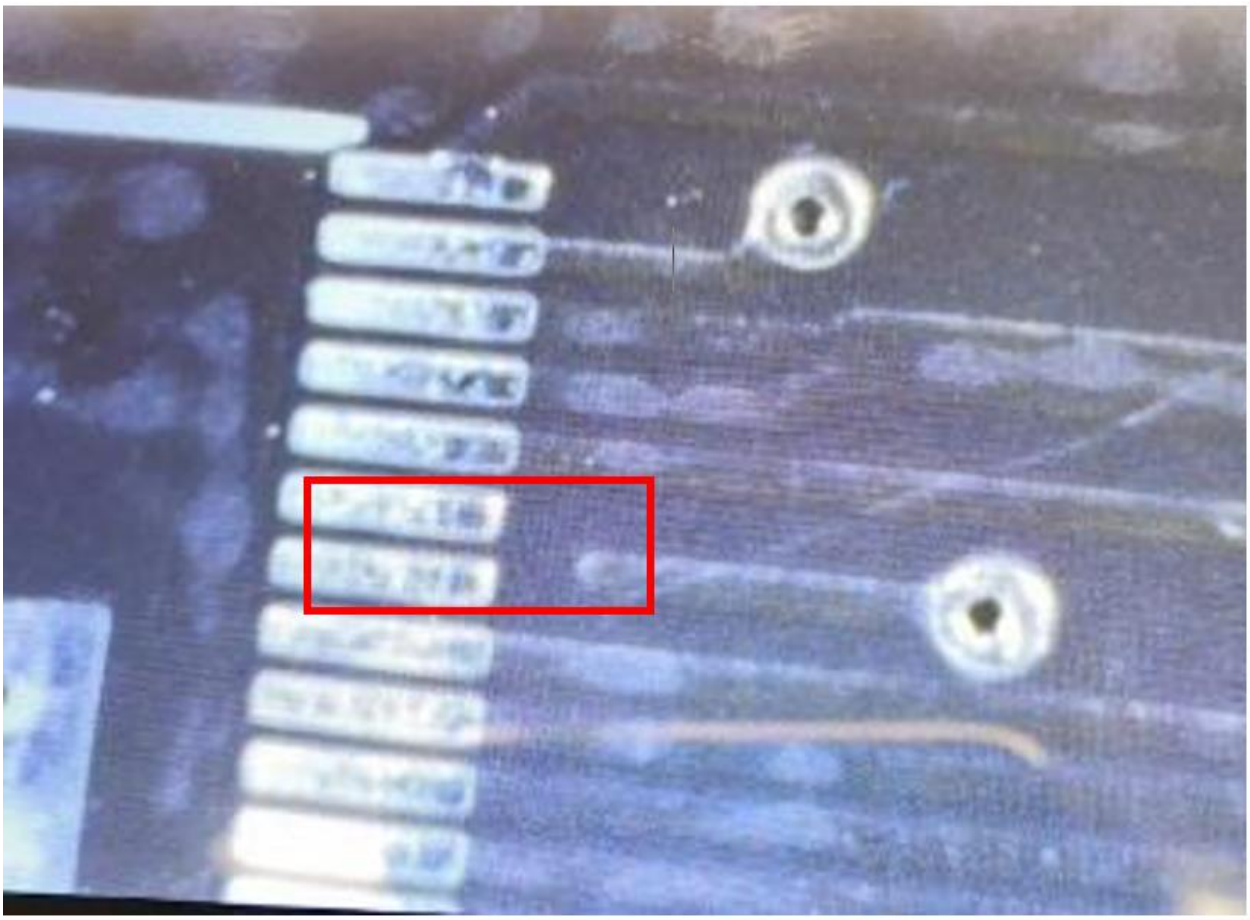

Figure 55. Missing Trace on DRV8301

There were a few errors in the final PCB that would need to be addressed in the next iteration for the board to pass the technical inspection. There was a missing trace on the DRV8301 driver chip as shown above, connecting pins 50 and 51(PH), which are used for the internal buck converter. These pins are essential in operating the motor controller board as they supply the 5V which powers the microcontroller and the feedback circuits. We were able to test the board without this using the USB power from a PC; however, for the motor controller to be a standalone unit, we would need the PH pins to be connected. Connecting it with a wire would be a temporary solution but it would need to be done carefully or else the pin could be ripped up off the PCB damaging the trace and the board. While this could be done temporarily for testing purposes, we advised against it for competition. Using a wire could also short the neighboring pins on the DRV8301 causing the motor controller to fail and presenting a safety hazard.

Since we had large electrolytic capacitors at the input terminals, it would spark when connecting the board to the battery, which was an electrical safety hazard; therefore, future iterations of the board shall have an anti-spark switch to inhibit this spark. The club was in the process of designing an anti-spark switch that may be used in series between the battery and the motor controller. We also observed that the MOSFETs when powering the motor were quite toasty.

Therefore, we recommend adding vias underneath the surface mount MOSFETs. Additionally, surface mount components can be replaced with through hole MOSFETs with heat sinks to dissipate the heat generated when running the motor. Although the heat distribution test was not conducted, the six MOSFETs and the gate driver IC are suspected to dissipate the most heat.

7.2 Motor Controller Programming

The controller program was developed in C++ using Code Composer Studio with the Insta Spin motor control labs. The TI Launchpad includes gate driving programs that were adapted to our software solution. This solution includes the software for the waveform generation for trapezoidal control (6-step commutation), and we integrated it into a solution for driving the vehicle. The project contains configuration files which allow the team to change motor and control parameters. They can easily configure acceleration profiles and speed set points, as well as link control with the driver inputs. The final project for software was uploaded to the Supermileage shared drive.

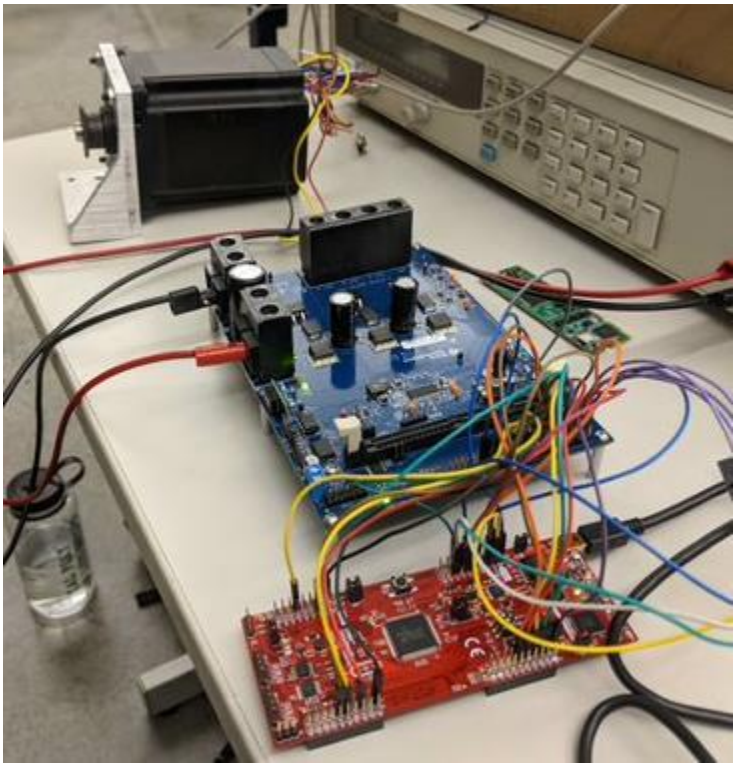

Figure 56. Motor Controller Programming Setup at Mechatronics Lab

7.3 Drivetrain Manufacturing

Assembly of the drivetrain was 50/50 off the shelf/custom manufactured components. The hub was ordered from Onyx, the small sprockets and chain were ordered from McMaster Carr. The wheel dropouts and the large sprockets were made inhouse at the Cal Poly student machine shops.

7.3.1 Sprocket

The SolidWorks drawing of the large sprocket was exported to a DXF file and taken to the Industrial Technologies machine shop to be water jet. The sprockets were cut out of 12-gauge cold rolled steel sheet because of its superior flatness and ability to holds tight tolerances. The water jet process was able to ensure tolerance +0.002” for a precise spline fit and maintain the flatness of the stock. The steel sheets used were stock ordered for the 2018 senior project available in the Supermileage storage crate and were at no cost to this project.

After the sprocket was water jet the edges were deburred with a grinding wheel. The individual teeth were hand filed to create a smooth finish that would reduce friction and chain wear. The development of the sprocket can be seen in Figure 57 below.

Figure 57. Water jetting sprocket and deburring after

Note on Sprocket Manufacturing

The first sprocket was produced on the Advanced Technologies Lab water jet which has a table size of 16 x 16 inches. This required the 5 x 5 ft stock sheets to be cut down for manufacturing. The first sprocket produced in this way had significant warpage. We believe that cutting the flat stock using the hydraulic shear caused plate warp. The industrial Technologies lab could accommodate the full stock size and produced sprockets within the flatness specification.

7.3.2 Dropouts

The dropouts were machined in three separate pieces. The housing and the slider were CNC milled from aluminum stock, shown in Figure 58. The knobs were turned manually from hex stock. The sliders had to be sanded after milling to perfect the fit and maneuverability within the housing. A light lubricant was also used to provide smoother adjustment. The round protrusions

on the base of the dropouts served as a locating feature which would press fit into counterbores in the plate inserts as seen in Figure 59.

Interior and exterior threads on the sliders were tapped by hand. Threaded 1/4-20 rods were then threaded with Loctite into the sliders so that only the knobs could rotate. A nut, locking washer and wing nut were added onto the threaded rod to keep the sliders secure during operation. A washer and nut were threaded onto the slider external threads. The complete the assembly in Figure 59.

Figure 58. CNC Machined Dropout Mounts

Figure 59. Dropout Mounts Mounting on Motor Plate

7.3.3 Motor Mount

The motor mount was CNC machined. A model was created in SolidWorks and CAM was generated in HSMWorks. Stock was sourced from donated 1.75X3.75-inch 6061 Aluminum bar. After the mount was milled, helicoil inserts were added to the threaded holes in the base to strengthen them. Two alignment pin holes were enlarged to ¼ inch with a reamer bit for precision fit with locating pin heads. The motor plate with bolts attaching it from the bottom is shown on the motor plate in Figure 60.

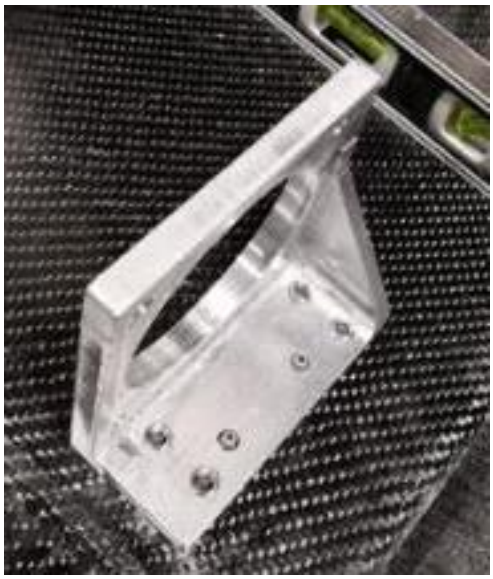

Figure 60. Motor Mount Mounted on Plate

7.4 Motor Plate

The first step in manufacturing the motor plate was to build a mold. This mold created a flat and smooth surface that would hold the wet layup and foam core together in the proper geometry while curing. After several iterations, plates of aluminum were screwed into a reinforced wooden base to create the general inverted shape of the plate. JBWeld was used to fill gaps and countersunk screws. The surface was then milled to create parallel horizontal surfaces. Figure 61 shows the mold in the HAAS VF3. A three-inch shell mill was selected to decrease the number of passes for facing. A 0.005-inch depth pass with manual feed was used. The part was so long in the x-direction that it had to be relocated twice because the part was out of the machining boundary of the table. Unfortunately, the wood base proved insufficiently rigid and hand sanding was necessary to reduce surface ripples caused by vibration.

Figure 61. Facing Plate Mold Manually on VF3

The mold was wet sanded up to 2500 grit to produce a mirror like finish which provided an excellent mold surface for layups. Before the layup was done the mold was brushed with PVA, a demolding film, and let dry for at least 20 minutes. This film provided an extra layer of protection against the plate adhering to the mold.

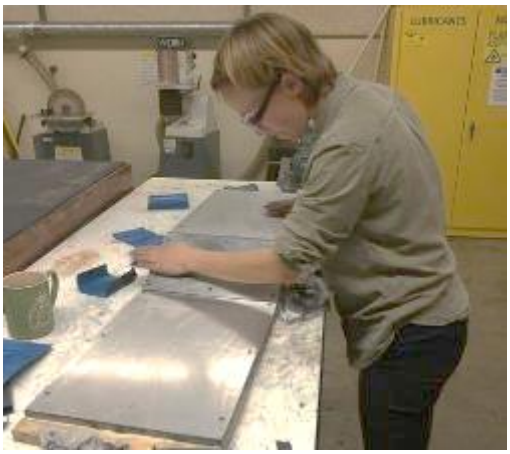

Figure 62. Aluminum Mold being Wet Sanded to 2500 Grid

The second step of motor plate manufacturing was preparing and performing the layup. A full mockup layup was performed to test the process and design. The plate was fabricated upside down on the mold so that the surface of the mold would produce the top side of the plate. This was important to produce the smooth and flat surface required for mounting components.

The foam core was cut into three rectangles having the basic dimensions of the top, middle (or slanted region), and bottom sections of the motor plate. The final profile of the plate was not cut

into the foam at this point in order to simplify the layup and avoid the use of locating features or pins in the mold to keep the upper arms from moving. The sections for the inserts were cut out of the foam as seen in Figure 64. Inserts were cut to dimension with a wood band saw and pressed into the core where compressive loading was foreseen as composite layup are not good for taking compressive loading. The inserts were made of ¾ in thick Garolite and walnut woods. Wood inserts were placed under the motor and brake mounts due to the limited amount of Garolite available. The inserts were wetted on all sides with resin and pressed into the core.

Figure 63. Cut Inserts for Motor Plate

Figure 64. Inserts Were Put into the Foam Core

Three layers of 3k twill carbon fiber were used on each side of the core. The layup schedule was [0/±45/90//90/±45/0] with 5-inch strips of unidirectional fiber in between each twill layer at the elbows. Because of the cool temperatures in the Aero Hanger where the layup was done, the vacuum bag was left on for 24 hours to ensure a complete cure before beginning the demolding process. The layup did not stick to the aluminum plated but the extra fibers overlapping the wood fixtures made it extremely hard to demold. A Dremel was used to cut away the excess cured carbon which allowed the plate to be removed without damage.

Figure 65. Cured motor plate after removing vacuum bag

After the plate was peeled from the mold, it was cut to its final profile. Measurements were taken from the SolidWorks assembly file and the cuts were made with a pneumatic jigsaw using a special composites blade. This produced a clean edge and straight lines.

This first mockup plate was then used to test the durability of the layup design. A drop test showed that the adhesion between the core and carbon fiber was quite strong and the foam fractured internally before delamination. The joints also proved robust and structurally sound after being dropped. This confirmed our layup schedule provided adequate strength and the surface wetting of the foam provided suitable bonding.

The internal foam fracture occurred at sections that had been cut out and the core was exposed. In order to mitigate this problem, we determined that adding edging strips where the foam was exposed would improve bending strength and stiffness as well as protect the core from contaminants. This was based on research done by Sam-Brew et al. and standard practice outlined in Hexcel technical guides.

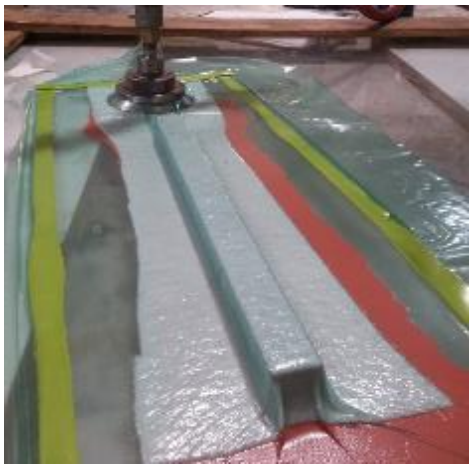

Figure 66. Curing edging strip used to increase plate strength along exposed edges

Once the layup design was improved with adding edging strips, the final layup was performed to create a new plate that would be used for the final assembly. The final plate was demolded and cut to shape and then fit into the chassis by sending down edges until the arms sat level and at the correct height. The last step was post-bonding edge strips onto the cut edges of the plate. Edge strip molds were milled from aluminum to the finished thickness of the plate. Two layers of 90° fabric were wetted and formed to the molds with a vacuum. This method of fabricating edge strips produced a very clean finished product opposed to post bonding with wetted fabric straight to the plate. A secondary layup was done to seal up the exposed foam with the edging pieces and fiber/uni patches.

Figure 67. Final motor plate being fit into chassis

Notes on Plate Manufacturing

The Polyisocyanurate foam used in this project did not have good structure for this application. It was originally bought because it can sustain a high temperature cure so it can be used with prepreg or in a post cure process. This originally gave us more flexibility in choosing our process. However, the foam was a compression of foam powder and was very easy to gouge with a cloth. It maintained a powdery surface that made it difficult to clean and wet out. It was not user-friendly when shaping, was fragile and cracked easily. In the future we would not suggest using Polyisocyanurate foam as a sandwich board core. Alternate foams, rather than solid materials, should be considered due to their low density.

A Further Note on Composites Molds

We attempted four different types of molds in order to create the dual level motor plate. The idea for the first mold was to mill the shape into high density tooling foam. This process is used in many composite applications. After milling the foam gets multiple Duratec coats and high grit sanding to create a smooth surface. Although we planned on using this method, due to machine shop upgrades, the CNC router used on foam was being rebuilt and was unavailable.

The second idea for a mold was to create a solid aluminum mold surface. This is a method professional composite manufactures use because aluminum is easy to machine, provides a great surface finish with minimal surface prep, can handle oven temperatures, and is durable for repeated use. However, since the motor plate was 30 inches long this required a chunk of aluminum that was prohibitively expensive for this senior project. Attempts to piece together aluminum chunks with JB Weld were abandoned under distrust of bonding strength under machining forces.

The third mold was fabricated out of ¾ in ADX plywood using screws and wood glue. After it was assembled the two horizontal surfaces were milled with a 3in fly cutter so that they would have parallel planes. Unfortunately, the porosity of the surface gave it a very poor surface finish. A layer of paraffin wax was squeegeed across the surface to fill the porosity, but adhesion was very poor. A 5-inch wide test piece was very difficult to remove from the mold. Based on concerns of surfaces warping a more durable solution was sought.

This brought us to our final fabricated mold solution, aluminum plates held in place by a wooden frame. This was a compromise between having a hard surface of aluminum to create a good surface finish and not having to use a whole block of aluminum. The aluminum plates were fastened onto the wood base using screws and L brackets. Once assembled, the plate was machined on its horizontal planes to ensure they maintained a parallel orientation relative to each other. Milling the aluminum plates on a wood base turned out to be a very unstable arrangement. The first attempt using a 6 in fly-cutter produced so much vibration it was abandoned after a few passes. The mold had not been designed with fitting on a milling table in mind, either in length or in fixturing. The mold was longer than the travel of any mill would allow, and the base did not accommodate being secured by a vice or easily toe clamped. The fixturing problem resulted in a

set up that vibrated under machining loads and did not give the smooth machined surface finish hoped for.

The better route to have taken for the mold would have been to use an aluminum base welded onto the aluminum plates. Unfortunately, the timing of our senior project and the equipment available did not allow us to use these options at the time.

Table 15. Summary of comparison among mold options

	Solid Aluminum Mold	Wood Mold	Aluminum Sheet Mold (with wood support)	Aluminum Sheet Mold (with aluminum welded base)	40lb Foam Mold
Ease of Manufacturing	Difficult	Easy	Difficult	Moderate	Difficult
Surface Durability	Excellent	Poor	Excellent	Excellent	Moderate
Alignment Durability	Excellent	Poor	Poor	Good	Good
Reusable	Yes	No	No	Yes	Yes
Cost	$$$$	$	$$	$$$	$$$

7.5 Motor Plate Assembly

Once the motor plate was completed, the final assembly of components onto the plate was done on a manual mill. The process for the complete assembly and integration into the chassis was chronologically as follows:

- Dropout placement on motor plate
- Motor mount alignment to dropouts
- Addition of locating pins in motor mount to fine tune alignment of sprockets
- Motor plate placement into chassis to align rear wheel to front wheels

The dropout placement was performed on the Bridgeport manual mill in the Mustang 60 student machine shop. The motor plate was first squared to the mill axis using a dial indicator along the front edge of the plate.

Figure 68. Squaring motor plate in preparation for aligning dropout holes

The manufactured plate was not perfectly square, so only the x-axis was aligned with the mill axis since this was the critical axis for alignment. The complete rear axle assembly was used to measure the center to center distance of all four dropout mounting holes. These dimensions were then checked to ensure they would be centered on the plate inserts. The x-distance from the back of the plate was taken from the SolidWorks model which considers the geometry of the chassis' back compartment and the required position for the rear axle in order to have enough clearance with the rear hatch. The y-location was determined from visually centering on the inserts. Using the digital readout on the manual mill, the x and y-locations of the remaining three holes were determined and drilled. Counterbores were then drilled in the motor plate top surface for the dropout location features.

Once the location of the dropouts was set, the dropout assembly and the motor assembly were placed on the motor plate. The dropout assembly used one of the water jet sprockets cut down to the central disk which allowed spindle and table clearance while providing a surface for alignment. The assembly used for alignment is shown in Figure 69. The motor mount assembly consisted of the motor mount, motor, and small sprocket. Using a dial indicator, the face of the small sprocket and the large sprocket were aligned within one thousandth of an inch. This established the x and y axis alignment for the motor mount bolt holes. With the motor mount held in place a transfer punch was used to mark the plate surface.

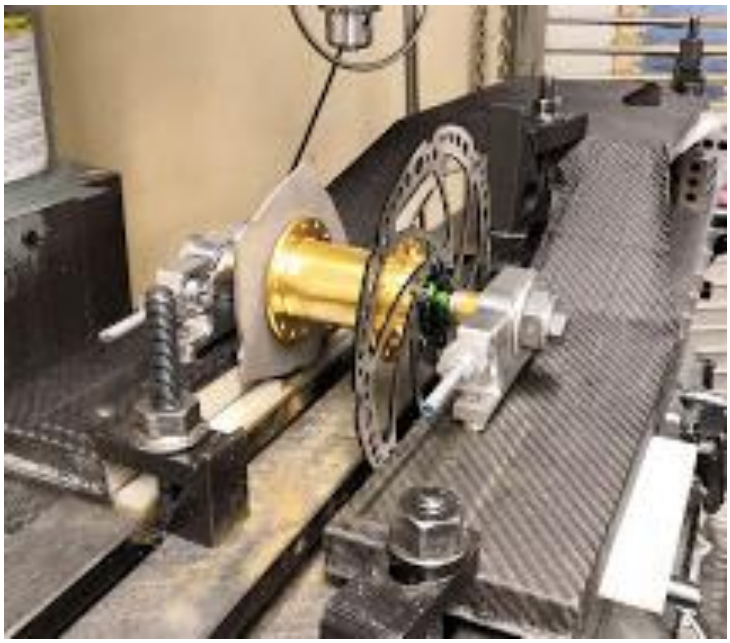

Figure 69. Dropout assembly with cut down sprocket for alignment

Once all the bolt holes were drilled, the motor plate was assembled with the rear dropout assembly and the motor assembly. With all bolts tightened to operational conditions the motor plate assembly was placed under the MicroVu coordinate measuring machining (CMM) available in Mustang 60. This initial measurement was used to determine final adjustments to alignment and mark the motor mount locating pin positions. The CMM creates two planes from measurement points taken from the small and large sprocket. The planar offset and the angular measurement between these two planes checked the tolerances specified in the technical specifications. The allowable angular tolerance was 1° and the allowable planar tolerance was 0.05 inches. In the first measurement the angular tolerance was 0.5° and the planar tolerance was 0.02 in. Based on this reading we set the pin locations and completed the motor plate assembly.

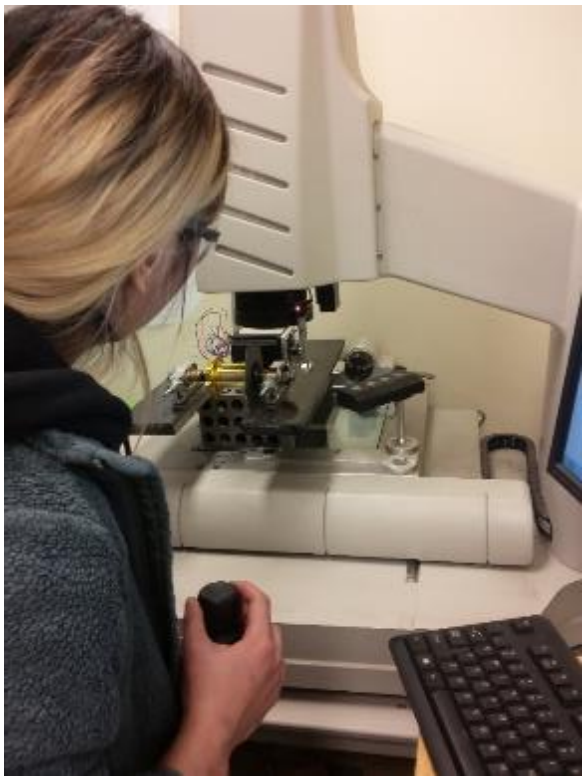

Figure 70. Probing with a Star Probe on the CMM to Measure Sprocket Alignment

Note on axle position on motor plate

This geometry was verified through multiple measurements and a mock wheel which left a chalk mark on the inside of the top hatch if it interfered when spinning. The proper position of the axle was marked on the chassis to facilitate integration.

Alignment Jig and Chassis Brackets

An alignment jig was created for the E-Ventus chassis in order to ensure proper placement of the motor plate in the chassis. Although in past years rear wheel alignment has not been a priority, our team felt that to ensure proper driver control and energy efficiency, a physical system to align the back wheel to the front steering was critical. In order to accomplish this a steel frame was fabricated which held the front axles and ensured the rear wheel was centered between them. The alignment jig is shown in Figure 71. The single vertical tubing at the rear has an adjustable axle that bolts on and fits snuggly into the rear dropouts. Having this horizontal axle be removable allows the chassis to be placed over the jig. The “T” at the front holds the front axle in cups in the vertical members. The front axle base is slotted to allow for horizontal adjustment of the axle position. This provides for fine-tuned centering of the rear axle base to the front axle base. Small holes drilled under the front axle cups allow string to be pulled from each upright to the rear axle providing a quick and accurate check of the axle center. The front axles were measured at 9.5” above the floor and the rear axle 10” above the floor. The alignment jig is designed to fit under the car and through the wheel wells to interface with the wheel axles.

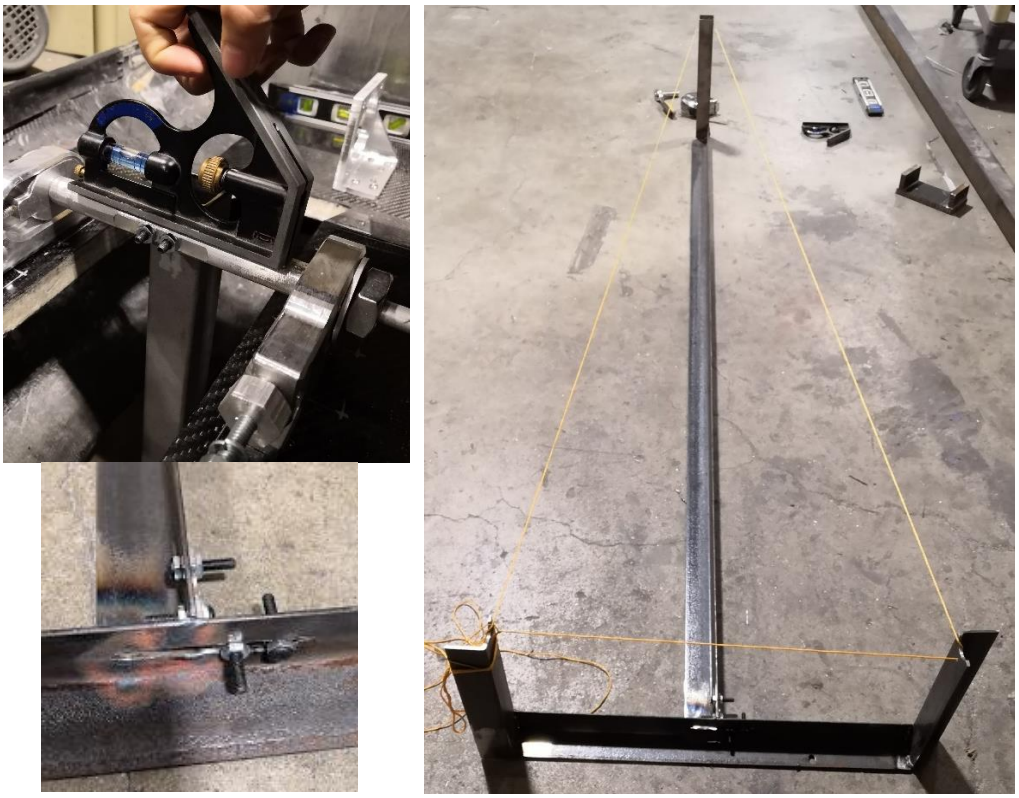

Figure 71. Alignment jig. [top left] Leveling jig axle with plate attached. [bottom left] Slot for centering front axles to back axle. [right] Squaring the jig before placing the chassis over it.

The alignment of the jig was set first by centering the front axle “T” using string and a measuring tape. The T was adjusted in the slot until both strings were the same length. Then the chassis was dropped over the jig and the rear jig axle with the plate attached was bolted on and leveled. The jig axle held the plate at the correct height and position so that the chassis brackets could be shaped to the chassis walls while fitting snugly under the plate arms. The position and outline of the plate was marked in silver sharpie and the plate was removed. This provided a guide for the bracket installation.

The chassis bracket installation occurred in two steps. First the brackets were bonded in with an epoxy silica mix. The brackets were clamped in the position marked when the jig was used. After the epoxy dried a reinforcement layup was done and vacuum bagged for increased bonding strength.

Figure 72. Bonding brackets into the chassis

After the brackets were cured, the jig was again used to place the plate in the chassis. A third bracket was shaped and epoxied under the plate at the firewall to provide support to the cantilevered end of the plate. Where the sloped portion and lower section meet, the plate is supported by the chassis floor. The height of the chassis was adjusted so that the plate arms rested snuggly against the brackets. This position prepared the plate for chassis integration.

Chassis Integration

With the plate arms held in place by the jig, six bolt holes were drilled simultaneously through the plate and brackets. Two bolts on each arm and two bolts at the front of the plate by the firewall. Five holes for locating pins were also drilled through the plate and into the brackets. Two locating pins on each arm and one at the plate front. After all the holes had been drilled the jig was removed. The holes in the brackets were enlarged for weld nuts that were pressed into the inserts from the bottom side and epoxied in place. The weld nuts made assembly and disassembly easier for the plate because it removed the need to use a wrench or keep track of loose nuts. The locating pins were then pressed into the holes in the chassis brackets. A paired round and diamond head pins were used on each of the arms and a single diamond head pin was used at the front. The pin holes in the plate were then expanded and reamed to snuggly fit over the pins. Once the plate was set the caliper break mount, battery box, and controller box were added to the plate.

Battery and Controller Box

The battery and controller box were fabricated out of 1/16” aluminum sheet and tinted Polycarbonate. The plastic protects the electronics from environmental factors and the aluminum provides heat dissipation. A Shell requirement was that the battery be contained within a metal box and secured into the vehicle. The battery box is screwed into the motor plate using weld nuts and three pieces of industrial Velcro secures the plastic lid over the battery. A 15-amp circuit breaker mounts into the side of the battery box and provides easy access if the breaker ever needs

to be reset. The motor controller box is completely removeable from the plate to allow for swapping boards without taking the plate out. A plastic door can be released by a clasp and slid out from beside the motor for even quicker access.

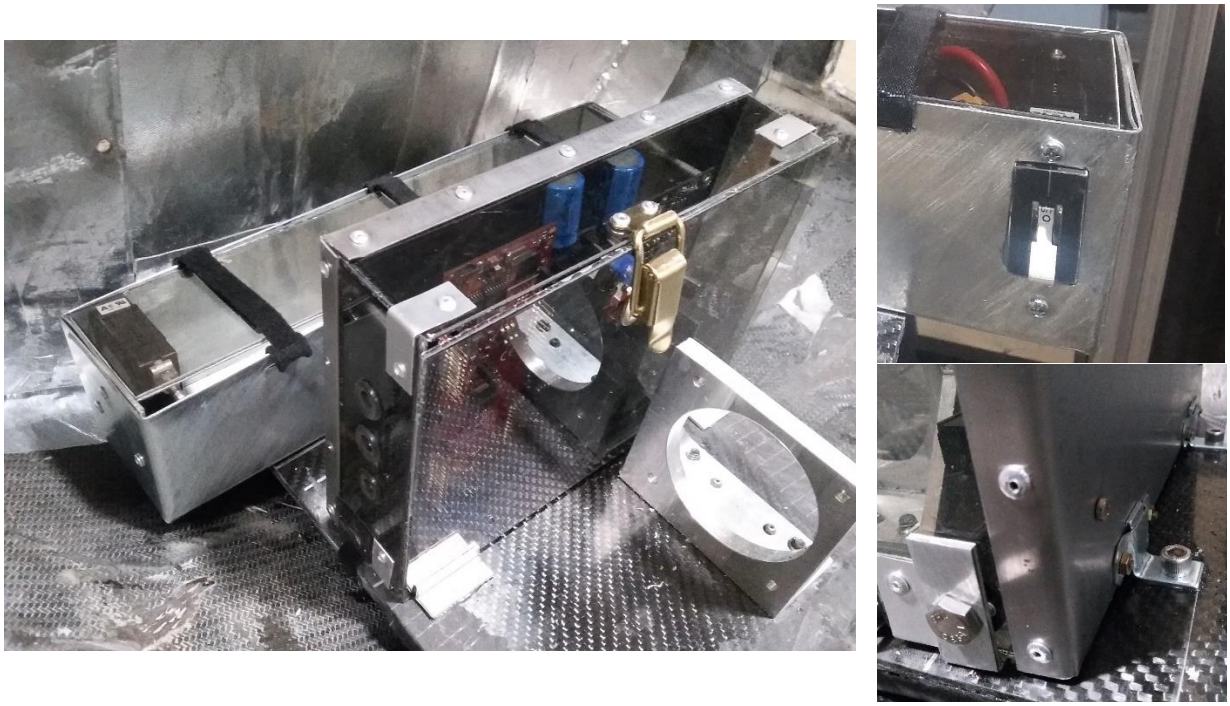

Figure 73. Motor controller and battery box

Figure 74. Finished assembly in chassis (motor not shown)

8 Design Verification and Testing

Tests were conducted at three phases in the design process. The three phases in chronological order are Component, Powertrain, and Vehicle Testing. The test plan is summarized in Appendix AA. For any acceptance criteria not satisfied, the results are analyzed to determine if the test methods or component must be redesigned.

8.1 Testing Completed

8.1.1 Composite Insert Strength

Due to time constraints during the manufacturing period an individual insert was not tested for bonding strength. However, the design and manufacturing method for using Gerolite inserts is one the Supermileage team has used for many years previously without issue. Due to this proven design we felt confident using these components without testing this quarter.

The bond of the 2-lb Polyisocyanurate foam bond was tested in a trial motor plate. The plate was manufactured, trimmed to final size, and the exposed foam edges were sealed with an epoxy micro- balloon mixture. The test plate was then dropped from four feet onto a concrete floor. The bond at the interface between carbon and foam was intact after the fall with no visible delamination. However, the foam itself cracked at the mid thickness. After researching the phenomena, it was found that edge pieces of carbon or other materials are used to cover exposed core material and provide a path for force dissipation and increase shear strength. Therefore, from this test we updated the design and added pre-formed edge pieces that were post-bonded to the plate. Due to time limitations we were not able to test another trial plate.

8.1.2 Rear Hatch Packaging Space

The rear hatch was able to close and latch completely over the new position of the back wheel and allowed the wheel to spin freely.

Test Results = PASS

8.1.3 Motor Mount Perpendicularity

A perpendicularity tolerance of 0.0125” had been assigned to the motor mount face with respect to the base in order to minimize tolerance stacking in the overall assembly. Measurements with the MicroVu CMM after manufacturing showed perpendicularity out of tolerance by a few thou. However, because the parallelism between the two motor plate planes was so hard to control with our manufacturing process the precision of the motor mount would be irrelevant to the magnitude of the skew in the motor plate. Additionally, since the alignment between the sprockets would be measured from the assembly it was decided that the motor mount perpendicularity was not a critical feature and could be more efficiently controlled with shims during assembly rather than costly remanufacturing. We therefore determined that the perpendicularity achieved from the CNC manufacturing was enough.

8.1.4 Sprocket Flatness

The water jet manufactured sprockets were measured for flatness the MicroVu CMM in the IME Metrology Lab. The acceptance criterion is flatness variance less than 0.0125”. Results from the CMM are summarized below in Table 16 and can be found in full in Appendix BB.

Table 16. Sprocket Flatness Results

Specification	Target	Measured	Pass/Fail
Sprocket Flatness	0.0125 inches	0.0102 inches	PASS

8.1.5 Sprocket-to-Sprocket Alignment

The planar and angular alignment of the two sprockets was verified using MicroVu coordinate measuring machine (CMM). The acceptance criterion is a variance of less than 0.05 inches for planar alignment and less than 1° for angular alignment. Alignment measurements using the CMM were performed by creating a representative plane for each of the sprockets by touching off at least nine points on each sprocket. The results from the CMM are given in Table 17, the data readout from the CMM in full can be found in Appendix CC.

Table 17. Sprocket Alignment Results

Specification	Target	Measurement	Pass/Fail
Planar Alignment	0.0 ±0.05 inches	0.0074	PASS
Angular Alignment	0± 1°	0.47°	PASS

8.1.6 Powertrain Weight

The powertrain weight includes motor plate, motor and motor mount, battery and battery box, motor controller box, dropouts, brake system (caliper, mount, rotor), sprockets, chain, wheel assembly (hub, spokes, rim).

Specification	Target	Measurement	Pass/Fail
Powertrain Weight	25 lbs	23.6 lbs	PASS

8.1.7 Motor Property Validation

This test validates the torque and back emf constants of the selected motor. The motor should be run on an electric motor dynamometer. The voltage at a steady state speed can be used to approximate the back emf constant. The properties should be compared to the manufacturer specified values.

The torque constant 'Kt' was found to be 21.36 oz-in/A as shown below, which is close to the specified value of 20.39 oz-in/A (less than 5% difference).

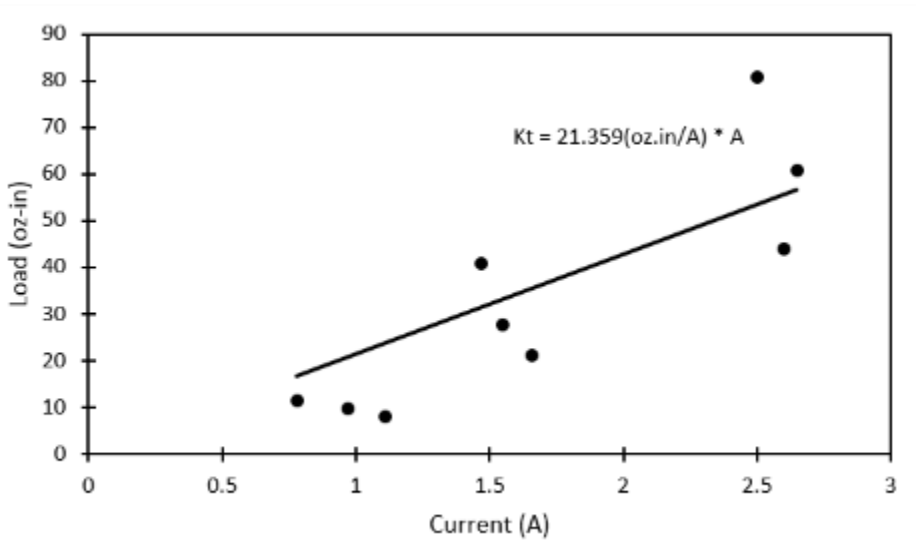

Figure 75: Electric Motor Dyno Data

8.1.8 Nominal and Maximum Battery Voltage

Battery was verified to fully charged to 54V as stated in battery specifications, cut off at 32.5V is controlled by BMS.

Specification	Target	Measured	Pass/Fail
Battery Voltage	< 60 V	54 V	PASS

8.2 Testing Partially Completed

8.2.1 Grade Climb

Based on vehicle dynamics, 190.5 oz -in is required to climb a 5% grade. This requires 8.9 A from the BLY344 motor according to the extrapolated torque-amp curve in Figure 75 which was acquired by running our motor on the electric dyno.

During dyno testing the greatest amperage achieved was 11 A which makes us confident that the selected motor should pass the grade climb. However, further testing is suggested to better qualify the motor behavior and create a more complete torque-amp trend line.

8.2.2 Dynamometer Testing

The goal of this testing was to check the speed, acceleration, and energy values of our powertrain. The initial test run was completed with a 35V battery.

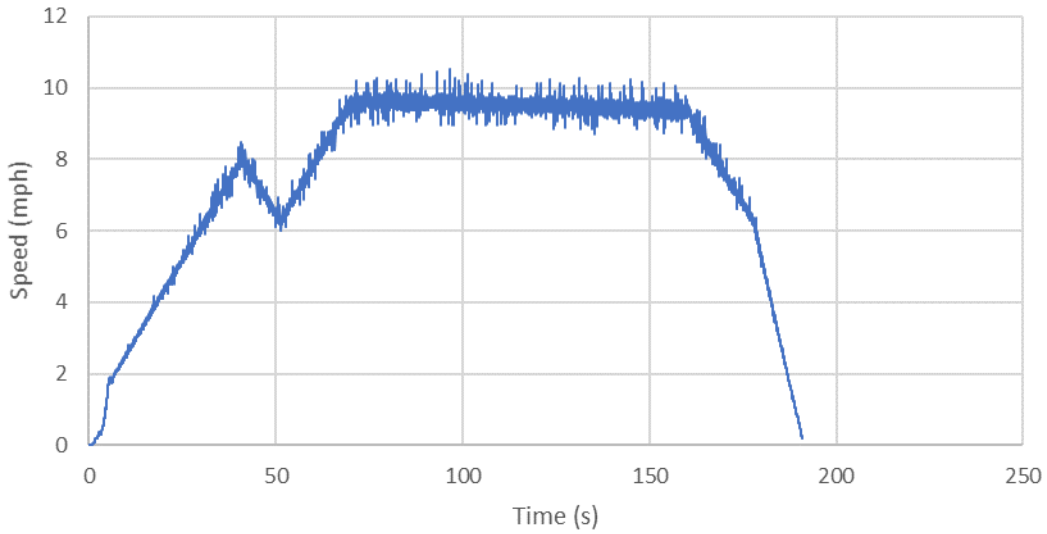

Figure 76: 35V Dyno Test Run

Table 18: 35V Dyno Test run data

Max Speed (mph)	9.5		Energy (W.h)	7.2
Max Current (A)	6.2		Distance (mi)	0.4
Voltage (V)	35.5		Efficiency (mi/kW.h)	55
Max Power (W)	220			

From the result of 9.5 mph at 35 Volts, it became evident that our top speed would not be as high as predicted, since 35 Volts is 73% of our nominal 48 Volts, and we need to at least double our power output to reach 18 mph. Additionally, the efficiency was well below our target value during accelerations. The results had multiple influence factors that would be discussed in next section.

8.2.2.1 Dynamometer speed test

The powertrain assembly was mounted to the club chassis dynamometer to measure the rpm of the wheel. This output steady state speeds at various voltage levels. The criteria for acceptance was to be able to maintain 15 miles per hour at 48 V. A power supply was rented from the ME tech lab to test at our nominal voltage level.

Table 19. Dynamometer Speed Test Results

Specification	Target	Measured	Pass/Fail
Vehicle Speed	15 MPH	13 MPH	FAIL

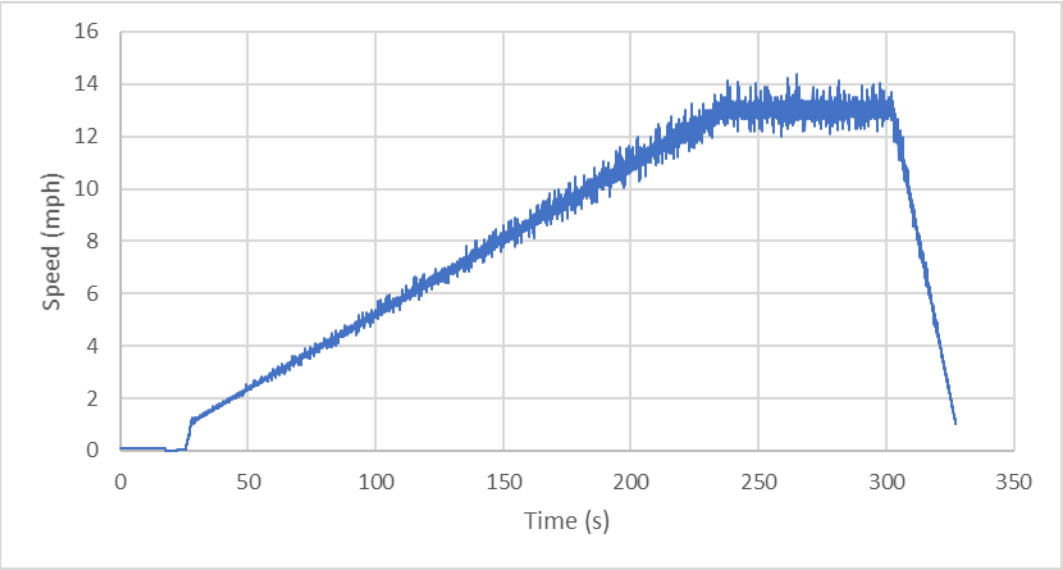

Figure 77. Maximum Speed Test on Dyno

Table 20: Maximum speed test data

Max Speed (mph)	13		Energy (W.h)	13.9
Max Current (A)	5.4		Distance (mi)	0.70
Voltage (V)	48		Efficiency (mi/kW.h)	50
Max Power (W)	255			

The maximum speed reached on the dyno was 13 mph. This fell below the minimum average requirement for the vehicle. Since the steady state speed was determined by the load on the motor, it was likely that the dyno has a higher resistance than the vehicle. After investigating the cause of this higher load, several sources were identified. The first friction source was the motorcycle brake put in place for emergencies constantly contacts the rotor. Attempts to remove the rubbing included cleaning the pistons, bleeding the hydraulic lines, and repositioning the caliper. All these efforts were ineffective at keeping the pads out of the way of the rotor. When the brake was removed the dyno had a much longer spin down; however, the brake could not be removed during testing for safety reasons. It would be suggested that a new braking system be implemented on the dynamometer in order to remove this energy loss.

Secondly, there was excessive loading on the bearings from clamping the tire down to the dyno. The clamping and using rough grip tape were needed to prevent tire slip on the dyno. However, the clamping force was not finely tuned, and any extra force added frictional losses to the system. The tires were also pressurized up to 100 psi after the plate was clamped to reduce slip by increasing the force on the tire as it expanded. To fix these issues, the clamping force should be calibrated to the actual force on the rear tire with a driver in the vehicle without allowing the tire to slip. However, there will always be additional losses in the system from the dyno bearings.

Hence, we believe that although the vehicle only reached 13 MPH max speed on the dyno, it is not a valid representation of the vehicle track speed. The true top speed for this system can be found when the car is ready for track testing in future years or if the dyno is improved to reduce excessive resistance.

8.2.2.2 Dynamometer Acceleration

The motor controller was tuned to run two acceleration profiles in order to compare energy consumption for a rapid and slow acceleration. Since acceleration is predicted to be the area of low efficiency, the test was intended to inform the driving strategy for the driver and allow set acceleration tables to be created for improved vehicle efficiency.

Test Results = Inconclusive

The power data from the fast run was lost, and the club ran out of resources to make additional runs. The acceleration should be tuned for driver comfort and handling. The vehicle should always run above a specified speed that results in a suitable average speed for the course. Once the vehicle is at its operating speed (10 to 15 mph), the driver can rely on negative slopes on the track to gain speed and accelerate under the smaller load to gain additional speed.

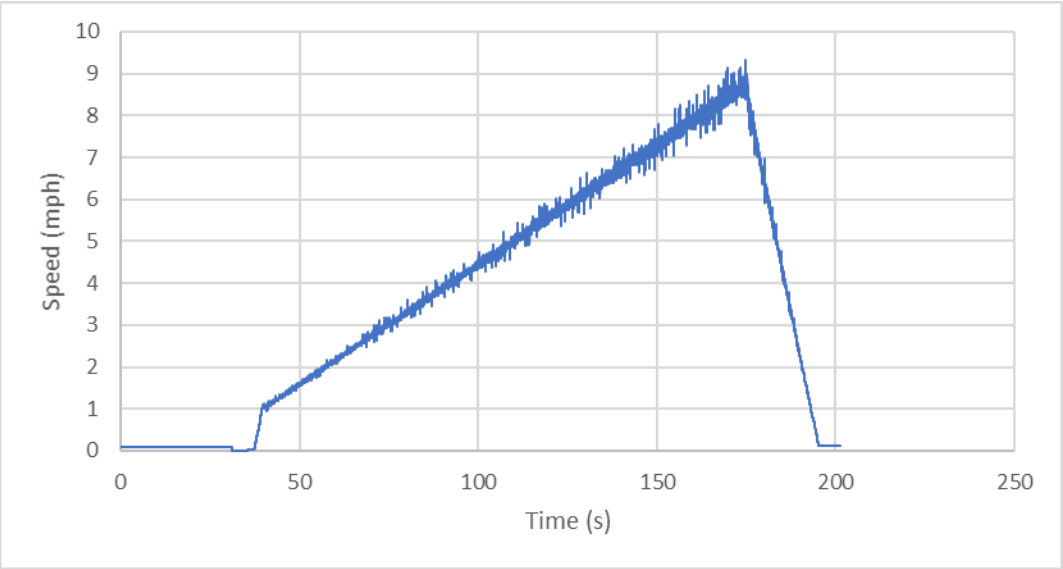

Figure 78: Dyno slow acceleration Ramp

Table 21: Slow acceleration ramp data

Max Speed (mph)	9		Energy (W.h)	4.5
Max Current (A)	3.63		Distance (mi)	0.21
Voltage (V)	48		Efficiency (mi/kW.h)	46
Max Power (W)	172.2			

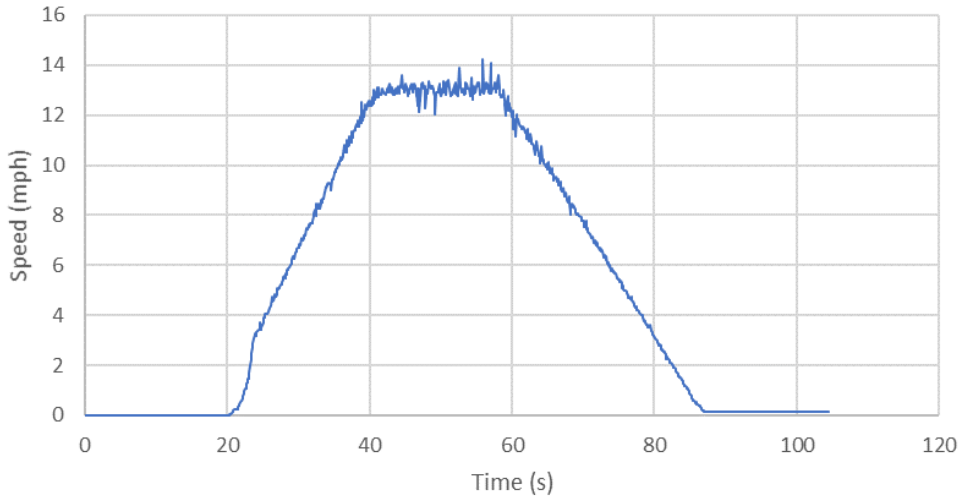

Figure 79: Dyno Fast Acceleration Ramp

Table 22: Fast acceleration ramp data

Max Speed (mph)	13		Energy (W.h)	-
Max Current (A)	-		Distance (mi)	0.031
Voltage (V)	48		Efficiency (mi/kW.h)	-
Max Power (W)	-			

8.3 Incomplete Testing

There were several setbacks in design development and vehicle was not ready for track testing by the end of our timeline. We recommend that the club follows through with these procedures in the future development of this vehicle.

8.3.1 Motor Control

The motor controller design went through three iterations, but still had hardware issues that prevented it from being competition ready. A detailed list of potential points of improvement and design changes can be found in Section 7.1. The software for the controller was validated on the evaluation board. It provides control over motor parameters, and acceleration parameters.

8.3.2 Motor Controller Heat Distribution

The motor controller board was not able to run long enough to perform a heat distribution test. Further testing on subsequent design iterations is suggested to better understand the heat dissipation and ventilation needs for the motor controller housing.

8.3.3 Battery Capacity

This test verifies the battery capacity is sufficient to power the vehicle through one competition run. The battery must have enough energy to run the motor at least 6.2 miles estimated from the dynamometer. Shell rules limit battery capacity to 1kWh. According to manufacturer's specs, the selected battery has 281 Wh capacity.

8.3.4 Drivetrain Damping Coefficient

A coast down test was not performed as the driver compartment was stripped out and left empty so that the vehicle weight was not accurate and there was no way to safely have the driver in the vehicle or steer the vehicle.

8.3.5 Ruggedness Impact

The ruggedness of the vehicle rear must be verified to sustain the expected forces from the track. The rear of the vehicle should be dropped from a height which verifies that the rear can sustain an impact force greater than 220 pounds.

8.3.6 Ruggedness Weather

The interior electrical components must be protected from the environment. The test should be conducted by briefly dousing the vehicle with water and rolling the vehicle over a tarp with a puddle. The electrical components should be observed for any signs of water. The acceptance criterion should be that the electronics are not in contact with water.

8.3.7 Vehicle speed test

The vehicle speed should be tested on the track. The vehicle must be able to maintain an average speed greater than 15 miles per hour and traverse 6.2 miles in under 26 minutes.

8.3.8 Vehicle System Efficiency

The efficiency of the vehicle should be verified. The efficiency must be greater than 250 miles per kilowatt hour or have an energy consumption of 24.8-Watt hours for 6.2 miles. Valid runs must complete 6.2 miles in under 26 minutes

8.3.9 Vehicle Damping Coefficient

A coast down test should be performed to find the damping coefficient of the vehicle. The outcome is to match the damping coefficient in the simulation with the vehicle by creating the same coast down profiles.

9 Conclusion

The Cal Poly Supermileage electric drivetrain and motor control design was, overall, a success. Mechanical drivetrain was complete, integrated into the vehicle, and ready to run. Battery was ordered and received, and the SMV electric team is ready to move it forward. The motor controller board went through three iterations of prototype *and* testing. The third iteration of the controller board was debugged and the SMV team shall be able to move forward with another iteration.

Based on the results from the dynamometer testing, we recommend running the vehicle to stay above a speed set point to limit the amount of time accelerating under load. The following control modes are recommended for efficient operation in these cases.

A. Accelerate Vehicle
    a. This case is when the race starts, this control scheme has a gentle acceleration profile for greater efficiency under load.
    b. It may also be used to increase the speed of the vehicle above the set point
B. Maintain Speed
    a. This mode ensures that the vehicle stays at or above the speed set point, it has a more aggressive acceleration profile for when the motor is not under load.

In software, the primary variable values are speed set point and acceleration rate. These values should be tuned to fit the vehicle.

Case	Speed Set Point	Acceleration Rate
A	Max SP	Med
B	SP	High

Case A rate should ramp to the set point without sacrificing handling and driver comfort. Case B should use a high acceleration rate because the vehicle speed will be above or at the set point, so the motor will be accelerating unloaded or under low loads. The driver should not experience this acceleration because the motor should reach the set point before the vehicle.

One option may be for the driver to use two buttons to control these schemes. The buttons can be split front and back of the same side of the steering wheel. The first button can be used to run at Case B and should be used most of the race. Both buttons, or just the second button, can be used to ramp at the lower acceleration rate.

In the end, we would love to take the time to thank the Cal Poly Supermileage team in sponsoring this senior project, all the people who contribute to this project (Professor Fabijanic, Dr. Rigidly, Dr. MacCarley, Dr. Mello, Trevor Jones, Cal Poly Machine Shop and so on), and finally the teammates that we worked closely with for the three quarters. This project would not be successful without any of you, and we shall keep the learn by doing principle at live.

10 References

Anderson, N. E., and S. H. Loewenthal. “Design of Spur Gears for Improved Efficiency.” *Journal of Mechanical Design*, vol. 104, no. 4, 1982, p. 767. doi:10.1115/1.3256434.

Anderson, N.E., and S.H. Loewenthal, January 1, 1983. “Comparison of Spur Gear Efficiency Prediction Methods”. *Advanced Power Transmission Technol*. NASA Lewis Research Center, Cleveland, OH. p 365-382

Batra, Mohit. 2018, “Dynamics and Model-Predictive Anti-Jerk Control of Connected Electric Vehicles,” Doctor of Philosophy in Systems Design Engineering, University of Waterloo, Ontario Canada.

Bickel, Chad "Optimizing Control of Shell Eco-Marathon Prototype Vehicle to Minimize Fuel Consumption", California Polytechnic State University, San Luis Obispo, CA

Blake, Carl and Bull Chris. “IGBT or MOSFET: Choose Wisely”. *International Rectifier*. Infineon Technologies, 2006

Eduardo, Viramontes, "BLDC Motor Control with Hall Effect Sensors Using the 9S08MP," Freescale Semiconductor, 2009

Kwang, Hee Nam, “AC Motor Control and Electric Vehicle Applications”, CRC Press, 2010 Taylor & Francis Group, LLC

Spicer, James B., et al. “Effects of Frictional Loss on Bicycle Chain Drive Efficiency.” *Journal of Mechanical Design*, vol. 123, no. 4, 2001, p. 598. doi:10.1115/1.1412848.

Bolton, M.R., J. Miller, H. Fields, 2017. “Cal Poly Supermileage Drivetrain Senior Project: Appendix G” California Polytechnic State University, San Luis Obispo, CA.

Ping Xiong & Chenglin Gu (2017) An improved startup mode using clutch coupling for in-wheel electric vehicle drives, Automatika, 58:1, 97-110, DOI: 10.1080/00051144.2017.1361612

Tazerart, F, Mokrani, Z, Reioua, D, & Rekioua, T "Direct torque control implementation with losses minimization of induction motor for electric vehicle applications with high operating life of the battery", Laboratoire de Technologie Industrielle et de l’Information (LTII), Faculte de Technologie, Universite de Bejaia, 06000, Bejaia, Algeria

Rogers, Eli. Memo to Supermileage Club, Cal Poly San Luis Obispo, April 25, 2015. “Subject: Requirements Meeting,” Supermileage Club documentation, Google Drive.

“Gates Carbon Drive System vs. Traditional Chain Drive: Efficiency Test”, Fiction Facts LLC. 2012.

“What are diamond locating pins and should I be using them?” Carlisia Layosa. June 17, 2014.

“Design and Properties of Sandwich Core Structures.” Michigan Technological University.

Joyce, P. 2003. “Sandwich Construction.” United States Naval Academy.

“Mechanical Properties of Carbon Fiber Composite Materials, Fiber / Epoxy resin (120°C Cure)”. December 2014. ACP Composites.

Sam-Brew, S., Semple, K., Smith G. D., Edge Reinforcement of Honeycomb Sandwich Panels, *Forest Products Journal*, Vol. 60 no. 4, pp 382-389, 2010

Sandwich Panel Fabrication Technology, Hexcel Composites, January 1997.

1 Appendix List

Appendix A: Gantt Chart

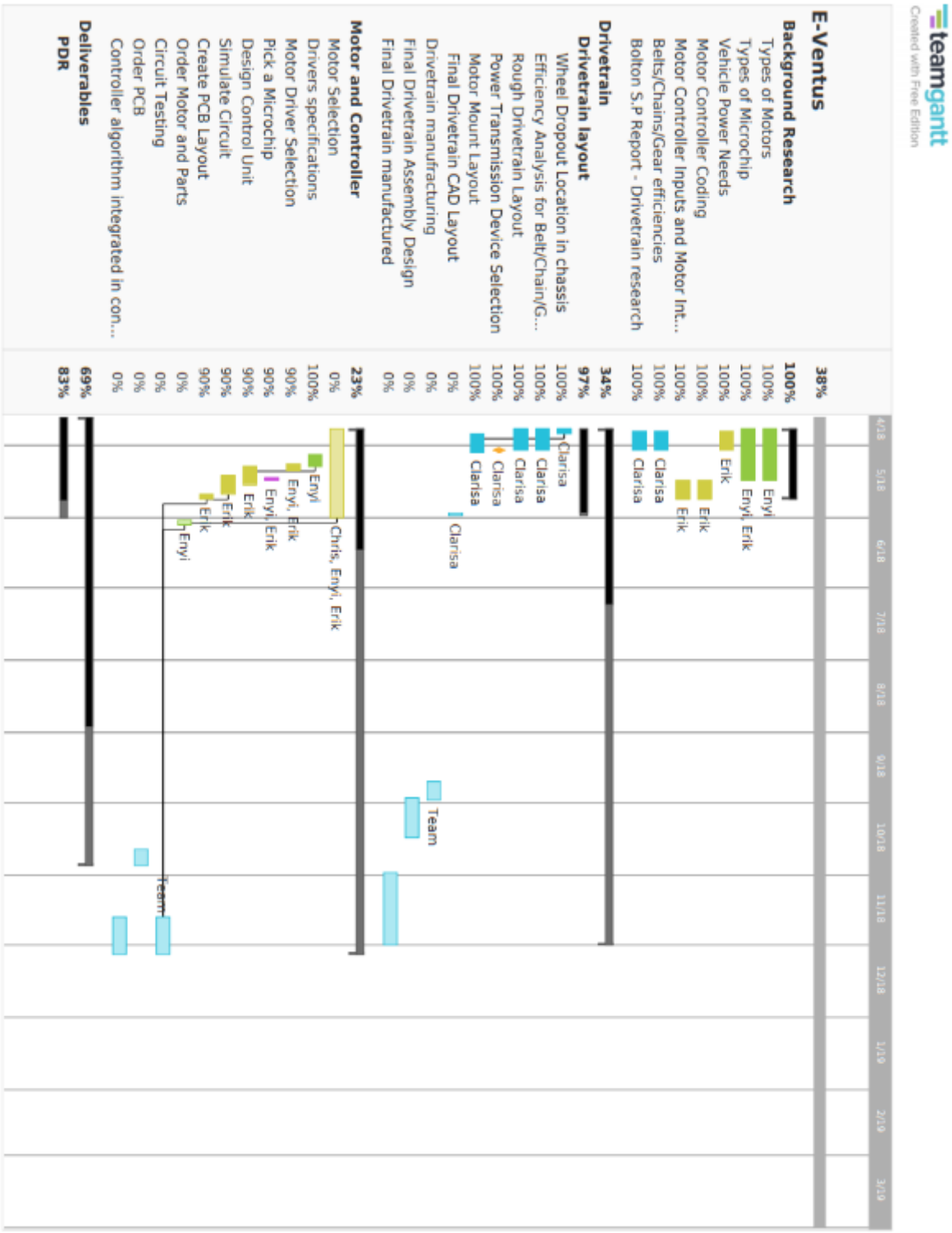

teamgantt
Created with Free Edition

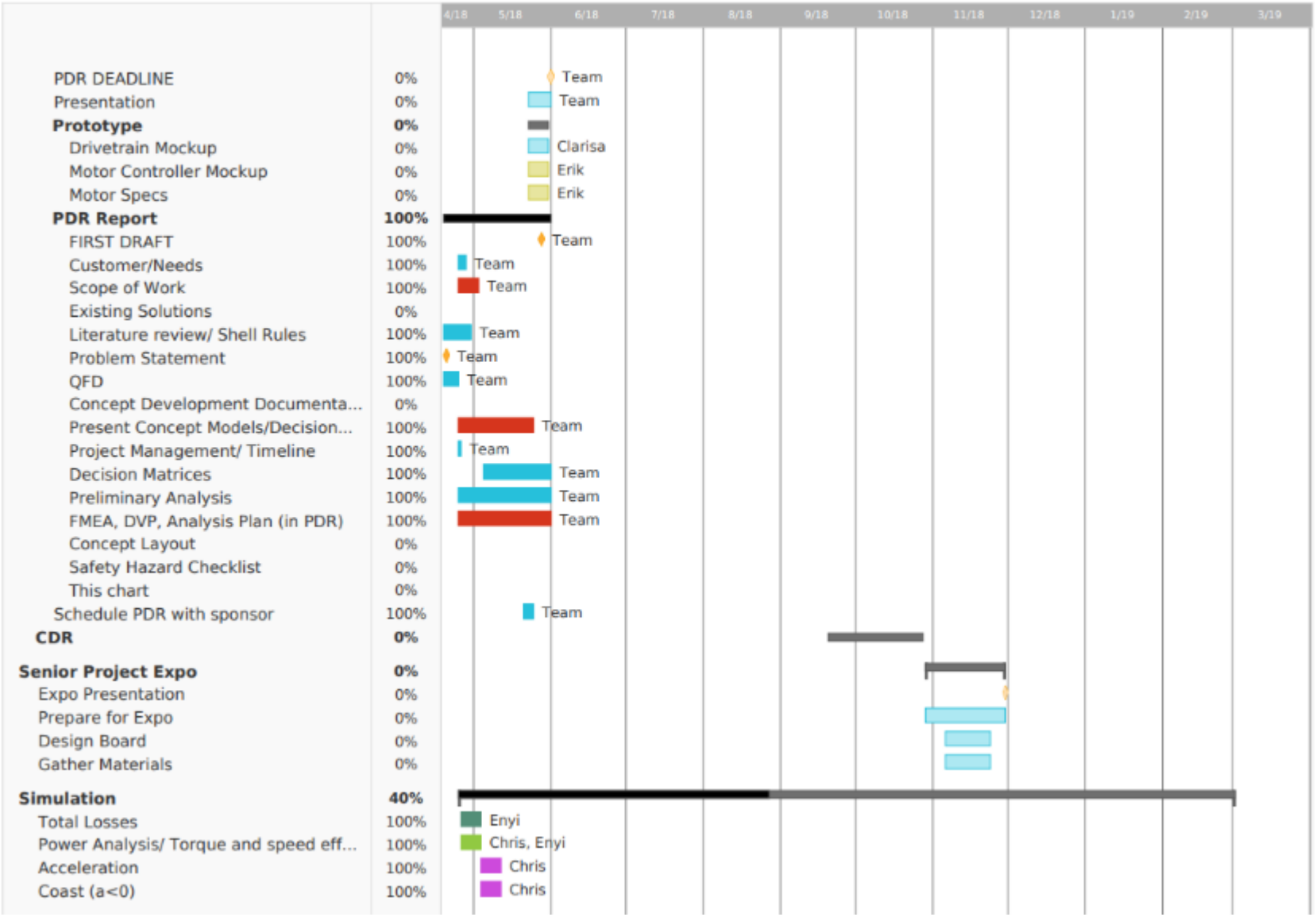

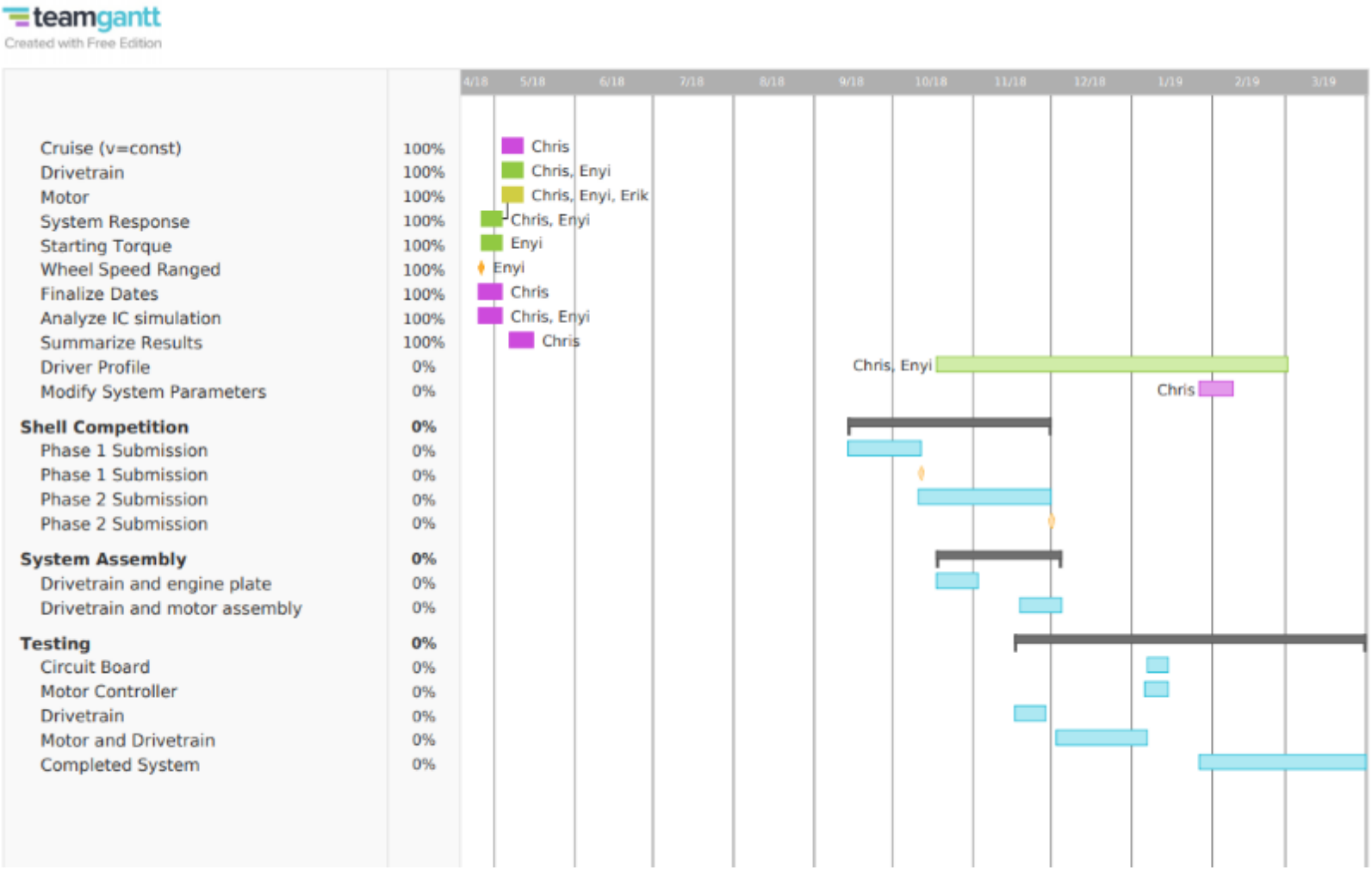
teamgantt
Created with Free Edition
4/18
5/18
6/18
7/18
8/18
9/18
10/18
11/18
12/18
1/19
2/19
3/19
Cruise (v=const) 100% Chris
Drivetrain 100% Chris, Enyi
Motor 100% Chris, Enyi, Erik
System Response 100% Chris, Enyi
Starting Torque 100% Enyi
Wheel Speed Ranged 100% Enyi
Finalize Dates 100% Chris
Analyze IC simulation 100% Chris, Enyi
Summarize Results 100% Chris
Driver Profile 0% Chris, Enyi
Modify System Parameters 0% Chris
Shell Competition 0%
Phase 1 Submission 0%
Phase 1 Submission 0%
Phase 2 Submission 0%
Phase 2 Submission 0%
System Assembly 0%
Drivetrain and engine plate 0%
Drivetrain and motor assembly 0%
Testing 0%
Circuit Board 0%
Motor Controller 0%
Drivetrain 0%
Motor and Drivetrain 0%
Completed System 0%

Appendix B: Full List of Customer Needs

The customer needs are summarized below:

- Shell Eco-marathon
    - System voltage under 60 V max
    - Voltage protection
    - Maximum 1,000 Wh capacity for any lithium ion battery
    - Battery must be contained in a metal box or battery bag (light-weight aluminum and semi-metallic materials are not acceptable)
    - All electric equipment must be properly fused
    - Bulkhead must separate the energy compartment from the driver
    - If using a manual clutch, the starter motor must not be operable with the clutch engaged.
    - Emergency shutdown mechanism to provide physical isolation for the propulsion battery from the electrical system (not power controller or logic system driven isolation system)
    - Dead man switch must be integrated into power system
    - Containers for electric components must be clear
    - Maximum vehicle weight without driver is 140 kg
    - The system must be able to safely handle an 8-meter 90-degree turn while accelerating (paraphrase with some assumptions)
    - For battery electric vehicles, the joule meter must be positioned so that the display can be easily read and reset from the outside of the vehicle without the removal of any vehicle body components. It is acceptable to access the joule meter from outside the vehicle though a hinged door.
    - For Prototype battery electric vehicles, the joule meter should be located between the vehicle electrical system and the motor controller.
    - Only one on-board battery is allowed. For battery electric vehicles this is the propulsion battery, which means that an accessory battery is not allowed.
        - Battery definition: A ‘battery’ is defined as a source of electrical energy, which has exactly two connectors and comes as a single unit. This single unit may contain more than one sub-unit.

    - The Battery Management System must automatically isolate the battery, without operator intervention, if a limit or out of range condition is reached
    - Wheel axels must be designed for cantilever loads
- Driver
    - Speed control should be simple
    - Vehicle should remain controllable
    - Drivetrain tuned so that throttling is reasonable and comfortable.
- Manufacturing Team
    - Reasonably easy to fabricate using the tools available through Mustang 60 and the Hanger
    - Reasonable manufacturing times and cost to allow iterations and spare parts to be fabricated as needed
    - Light weight and readily available material with necessary strength and rigidity
    - Reasonable tolerances for all parts
- Electronics Team
    - All electronic components must be easily installed, removed, and replaced
    - Electronic components are stored in a closed container
    - Minimum length of wires and reduce need for wires where possible
    - Allow for all electrical safety features to be interfaced with motor controller
    - Protection for electrical elements against moisture and dirt
- Brakes Team
    - Motor mount and drivetrain must allow for brake mounting
    - Motor mount and power train must be easily adjustable, allow for easy brake adjustments, Preferably the motor mount would not need to be detached or disassembled in any way
- Steering Team
    - Specify the motor and wheel location to be aligned with front steering system
    - Driver interface should integrate with steering wheel

Appendix C: Rotor Field-Oriented Control by Kwang

Based on the flux angle access methods, field-oriented controls are categorized as a direct or indirect method. Hall sensors or flux sensing coils may be employed to measure the rotor flux. Once the rotor flux is measured, the rotor flux angle can be calculated according to

$$\theta = \tan^{-1}\left(\frac{\lambda_{dr}^s}{\lambda_{qr}^s}\right). \tag{5.1}$$

However, installing sensors around the air gap is not an easy matter due to space limitation, armature reaction, noise, etc.

A more reasonable approach is to use current measurements and internally computed voltage values. The rotor flux is obtained indirectly from the stator flux and

stator current in such a way that

$$\begin{aligned}
\lambda_{dr}^s &= \frac{L_r}{L_m}(\lambda_{ds}^s - L_s i_{ds}^e) + L_m i_{ds}^e = \frac{L_r}{L_m}(\lambda_{ds}^s - \sigma L_s i_{ds}^s), \\
\lambda_{qr}^s &= \frac{L_r}{L_m}(\lambda_{qs}^s - L_s i_{qs}^e) + L_m i_{qs}^e = \frac{L_r}{L_m}(\lambda_{qs}^s - \sigma L_s i_{qs}^s).
\end{aligned}$$

Stator currents are easily measured by current sensors, and the stator fluxes are obtained by integrating $\mathbf{v}_s - r_s \mathbf{i}_s$, i.e.,

$$\lambda_{ds}^s = \int_0^t (v_{ds}^s - r_s i_{ds}^s) d\tau, \tag{5.2}$$

$$\lambda_{qs}^s = \int_0^t (v_{qs}^s - r_s i_{qs}^s) d\tau. \tag{5.3}$$

However, this approach is not reliable when a DC offset is present. On the other hand, indirect methods obtain the flux angle by exploiting the slip information calculated from the IM dynamic model.

5.2 Rotor Field-Orientated Scheme

We express (4.21) and (4.22) as

$$\lambda_{ds}^e = \left(L_s - \frac{L_m^2}{L_r}\right) i_{ds}^e + \frac{L_m}{L_r}\lambda_{dr}^e = L_s\sigma i_{ds}^e + \frac{L_m}{L_r}\lambda_{dr}^e, \tag{5.4}$$

$$\lambda_{qs}^e = \left(L_s - \frac{L_m^2}{L_r}\right) i_{qs}^e + \frac{L_m}{L_r}\lambda_{qr}^e = L_s\sigma i_{qs}^e + \frac{L_m}{L_r}\lambda_{qr}^e. \tag{5.5}$$

Utilizing (5.4) and (5.5), we obtain stator voltage equations as derived already in (4.37):

$$v_{ds}^e = (r_s + pL_s\sigma)i_{ds}^e + \frac{L_m}{L_r}p\lambda_{dr}^e - \omega_e\left(L_s\sigma i_{qs}^e + \frac{L_m}{L_r}\lambda_{qr}^e\right), \tag{5.6}$$

$$v_{qs}^e = (r_s + pL_s\sigma)i_{qs}^e + \frac{L_m}{L_r}p\lambda_{qr}^e + \omega_e\left(L_s\sigma i_{ds}^e + \frac{L_m}{L_r}\lambda_{dr}^e\right). \tag{5.7}$$

Rotor field-oriented scheme is achieved by aligning the d–axis to the rotor flux. This makes not only $\lambda_{qr}^e = 0$ but also $\dot{\lambda}_{qr}^e = 0$, as depicted in Fig. 5.1.

Stator Equation

By letting $\lambda_{qr}^e = 0$, we obtain from (5.6) and (5.7)

$$v_{ds}^e = (r_s + p\sigma L_s)i_{ds}^e - \omega_e\sigma L_s i_{qs}^e + \frac{L_m}{L_r}p\lambda_{dr}^e, \tag{5.8}$$

$$v_{qs}^e = (r_s + p\sigma L_s)i_{qs}^e + \omega_e\sigma L_s i_{ds}^e + \omega_e\frac{L_m}{L_r}\lambda_{dr}^e. \tag{5.9}$$

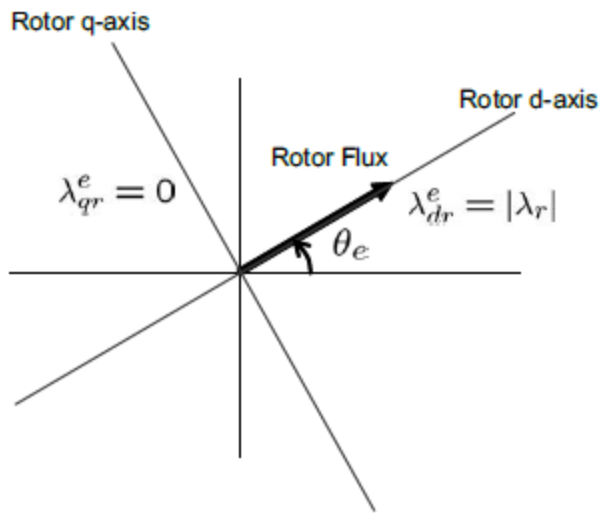

Figure 5.1: Alignment of d–axis to the rotor flux, $\boldsymbol{\lambda}^s_{dqr}$.

Note that $-\omega_e \sigma L_s i^e_{qs}$ and $\omega_e \sigma L_s i^e_{ds}$ are coupling terms between d and q axes dynamics, and that $\omega_e \frac{L_m}{L_r} \lambda^e_{dr}$ is the back EMF term.

Rotor Equation

Applying $\lambda^e_{qr} = 0$ and $\dot{\lambda}^e_{qr} = 0$ to (4.19) and (4.20), we obtain that

$$0 = r_r i^e_{dr} + p\lambda^e_{dr} = (r_r + L_r p) i^e_{dr} + p L_m i^e_{ds}, \tag{5.10}$$

$$0 = r_r i^e_{qr} + (\omega_e - \omega_r)\lambda^e_{dr}. \tag{5.11}$$

Therefore, it follows (5.10) that

$$i^e_{dr} = -\frac{L_m p i^e_{ds}}{r_r + pL_r} \tag{5.12}$$

Utilizing (5.12), we obtain the d–axis rotor flux such that

$$\begin{aligned} \lambda^e_{dr} &= L_m i^e_{ds} + L_r i^e_{dr} \\ &= L_m i^e_{ds} - \frac{L_r L_m p i^e_{ds}}{r_r + pL_r} \\ &= \frac{L_m}{1 + p\tau_r} i^e_{ds}\,, \end{aligned} \tag{5.13}$$

where $\tau_r = \frac{L_r}{r_r}$ is the rotor time constant. In the steady-state, (5.13) reduces to

$$\lambda^e_{dr} = L_m i^e_{ds}\,. \tag{5.14}$$

Since $\lambda^e_{qr} = 0$ in the rotor field-oriented scheme, it follows that

$$0 = L_m i^e_{qs} + L_r i^e_{qr}. \tag{5.15}$$

Then, the slip equation follows from (5.11) and (5.15):

$$\omega_e - \omega_r = s\omega_e = -r_r \frac{i_{qr}^e}{\lambda_{dr}} = \frac{r_r}{L_r}\frac{L_m}{\lambda_{dr}} i_{qs}^e \,. \tag{5.16}$$

Roles of i_{ds} and i_{qs}

Comparing (5.14) with $\lambda_{dr}^e = L_m i_{ds}^e + L_r i_{dr}^e$, it is observed that $i_{dr}^e = 0$. Now, the roles of d and q axes stator currents become clear: Q-axis current, i_{qs}, is proportional to the slip and thus to torque. d–axis current, i_{ds}, is used for producing the rotor flux, λ_{dr}^e. Fig. 5.2 shows the current vectors and flux vector in the rotor field-oriented scheme. Note however that a huge q–axis rotor current flows, although λ_{qr}^e is equal to zero. This can be interpreted that i_{qr}^e flows in opposition to i_{qs}^e to counteract a possible generation of q–axis rotor flux caused by i_{qs}^e, i.e., the rotor current flows to achieve $0 = \lambda_{qr}^e = L_r i_{qr}^e + L_m i_{qs}^e$. Note also from Fig. 5.2 that the stator current, $\mathbf{i}_{dqs}^e$, leads in phase angle the rotor flux, $\boldsymbol{\lambda}_{dqr}^e$ in the vector diagram.

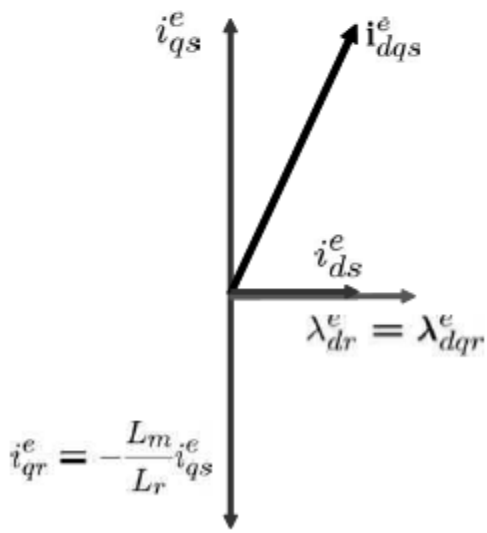

Figure 5.2: Current and flux vectors for the rotor field-oriented scheme.

Summarizing the above, the roles of currents are as follows:

1. i_{ds}^e is used solely for generating the rotor flux $\Leftarrow$ (5.13).

2. $i_{dr}^e = 0$ in the steady-state can be seen by comparing (4.23) with (5.14).

3. i_{qs}^e is used for generating torque $\Leftarrow$ (5.16).

4. i_{qr}^e flows in order to nullify a possible q–axis rotor flux generation caused by $i_{qs}^e \Leftarrow$ (4.24).

With $\lambda_{qr}^e = 0$, the torque equation (4.62) reduces to

$$T = \frac{3P}{4}\frac{L_m}{L_r}\lambda_{dr}^e i_{qs}^e.$$

This equation is comparable to the torque equation of the DC motor. The similarities with the DC motor are:

λ_{dr}^e corresponds to the field.
i_{ds}^e corresponds to the field current.
i_{qs}^e corresponds to the armature current.

Fig. 5.3 shows the field distribution that illustrates the rotor flux generation by i_{ds}^e, torque production by stator q–axis current, and the field cancelation between i_{qs}^e and i_{qr}^e.

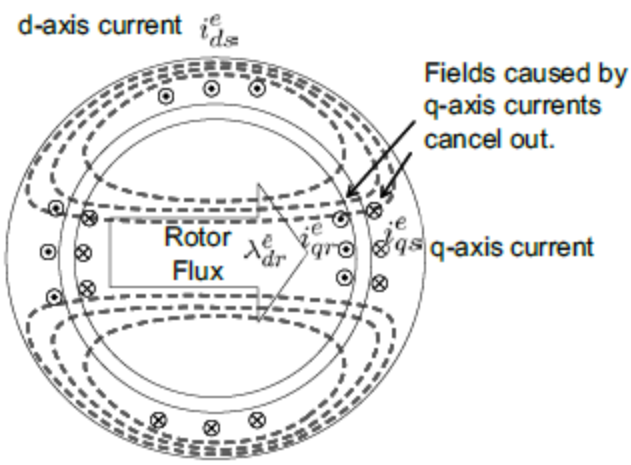

Figure 5.3: Torque production with the rotor field-oriented control: The rotor d–axis field acts on the stator q–axis current.

Vector Diagram in the Steady-State

In the steady-state, $p\lambda_{dr} = 0$ and $pi_{ds}^e = pi_{qs}^e = 0$. With the complex variables, (5.8) and (5.9) are rewritten as

$$\mathbf{v}_{dqs}^e = r_s \mathbf{i}_{dqs}^e + j\omega_e \sigma L_s \mathbf{i}_{dqs}^e + j\omega_e \frac{L_m}{L_r}\lambda_{dr}^e. \tag{5.17}$$

Based on (5.17), vector diagram for the rotor field-oriented control can be drawn as Fig. 5.4. Note that the voltage vector leads the current vector by ϕ.

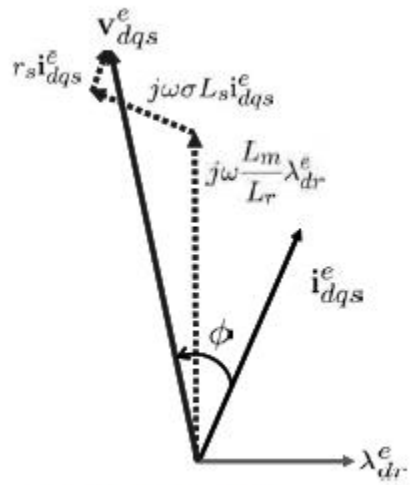

Figure 5.4: Voltage vector diagram for the rotor field-oriented control.

Substituting Laplace operator s for p, we obtain from (5.8) and (5.9) that

$$i^e_{ds} = \frac{\frac{1}{\sigma L_s}}{s+\frac{r_s}{\sigma L_s}} v^e_{ds} + \frac{1}{s+\frac{r_s}{\sigma L_s}} \omega_e i^e_{qs}, \tag{5.18}$$

$$i^e_{qs} = \frac{\frac{1}{\sigma L_s}}{s+\frac{r_s}{\sigma L_s}} \left(v^e_{qs} - \omega_e \frac{L_m}{L_r} \lambda^e_{dr} \right) - \frac{1}{s+\frac{r_s}{\sigma L_s}} \omega_e i^e_{ds}. \tag{5.19}$$

A block diagram based on the reduced model (5.18) and (5.19) is depicted in Fig. 5.5. The IM model contains just coupling terms and the back EMF.

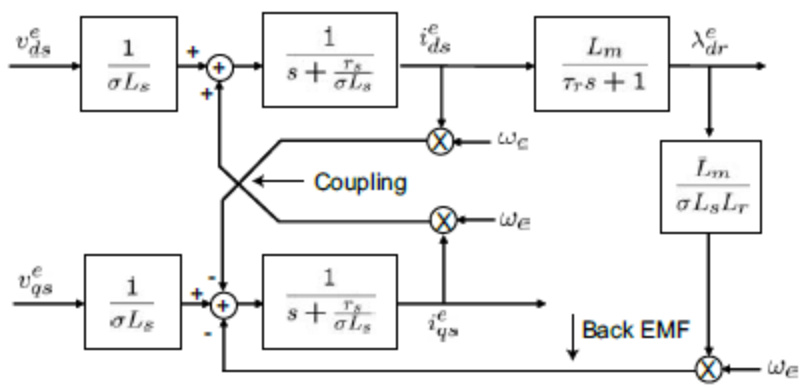

Figure 5.5: IM model under the rotor field-oriented scheme.

5.2.1 Field-Oriented Control Implementation

The IM dynamic model mimics the DC motor dynamic model in the rotor flux reference frame in which the roles of the dq-axes current are separated. Specifically, the d–axis current, functioning as the field current, should be regulated to keep a desired rotor field level. The q–axis current, functioning as the armature current, needs to be controlled for torque production in accordance with a high level controller.

Current Controller in the Synchronous Frame

For dq current regulation, it is necessary to measure the dq axis currents, and better to use PI controllers. However, to obtain dq axis currents in the synchronous (rotor field-oriented) frame, we should know the rotor flux angle, θ_e. Furthermore, the PI controllers output dq voltage commands, d_d^e and v_q^e. But, they have to be transformed into abc-frame to be used for gating the inverter switches. To summarize, the field-oriented current controller should be implemented in the synchronous frame and the rotor flux angle should be known for coordinate transformations.

Angle Estimation

The electrical angular velocity is obtained by adding slip speed to the motor shaft speed, i.e., $\omega_e = \omega_r + \omega_{sl}$. Encoders or resolvers are the most common speed sensors. The angular position θ_e of the rotor flux is obtained by integrating ω_e:

$$\theta_e = \int_0^t \omega_e dt = \int_0^t (\omega_{sl} + \omega_r) dt = \int_0^t (\frac{L_m i_{qs}^e}{\tau_r \lambda_{dr}^e} + \omega_r)\, dt. \tag{5.20}$$

Note that λ_{dr}^e is estimated by (5.13).

Angle Estimation

The electrical angular velocity is obtained by adding slip speed to the motor shaft speed, i.e., $\omega_e = \omega_r + \omega_{sl}$. Encoders or resolvers are the most common speed sensors. The angular position θ_e of the rotor flux is obtained by integrating ω_e:

$$\theta_e = \int_0^t \omega_e dt = \int_0^t (\omega_{sl} + \omega_r) dt = \int_0^t \left(\frac{L_m i_{qs}^e}{\tau_r \lambda_{dr}^e} + \omega_r\right) dt. \tag{5.20}$$

Note that λ_{dr}^e is estimated by (5.13).

Decoupling Current Controller

The most common regulation method is to use PI controller with the decoupling compensation:

$$v_{ds}^e = K_p(i_{ds}^{e*} - i_{ds}^e) + K_i \int_0^t (i_{ds}^{e*} - i_{ds}^e) dt - \omega_e \sigma L_s i_{qs}^e \,, \tag{5.21}$$

$$v_{qs}^e = K_p(i_{qs}^{e*} - i_{qs}^e) + K_i \int_0^t (i_{qs}^{e*} - i_{qs}^e) dt + \omega_e \sigma L_s i_{ds}^e + \omega_e \frac{L_m}{L_r} \lambda_{dr}^e \,, \tag{5.22}$$

where K_p and K_i are proportional and integral gains, respectively. Note that the back EMF, $\omega_e \frac{L_m}{L_r} \lambda_{dr}^e$ is also compensated in the q–axis current controller, (5.22).

The d–axis current is proportional to the flux, so that d–axis current command, i_d^{e*}, is linked directly to the flux level. The q–axis current command normally comes from high level control loops, e.g. torque or speed controller.

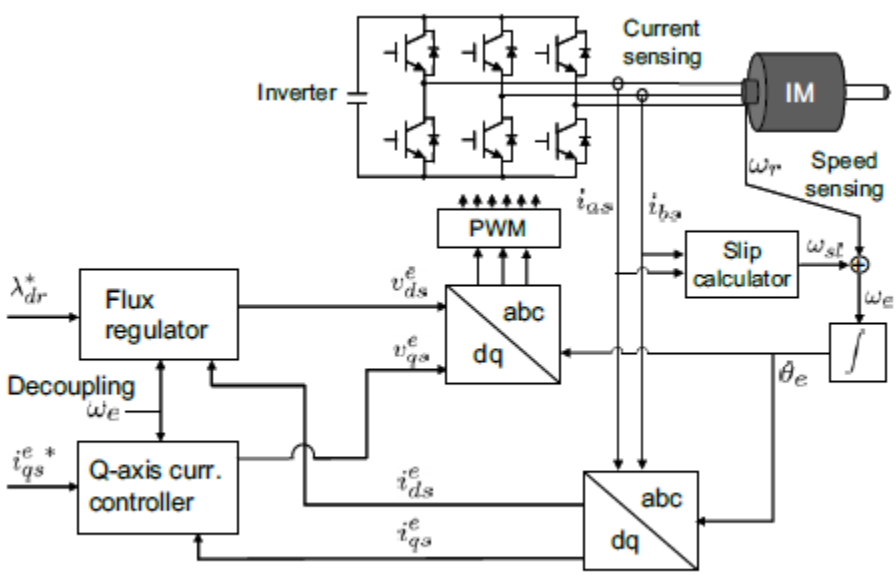

Figure 5.6: Field-oriented control block diagram involving coordinate changes.

Control Block Diagram

Block diagram for a typical field-oriented control is shown in Fig. 5.6. The field-oriented control can be illustrated with following individual steps:

1) Measure phase currents.
2) Estimate the rotor flux angle, θ_e according to (5.20).
3) Transform (i_{as}, i_{bs}) into (i^e_{ds}, i^e_{qs}) using the coordinate transformation map, $\mathbf{T}(\theta_e)$.
4) Construct dq current controllers. Apply decoupling feedback.
5) Transform the voltage vector, (v^e_{ds}, v^e_{qs}), into (v_{as}, v_{bs}, v_{cs}).
6) Convert (v_{as}, v_{bs}, v_{cs}) into on-duties of the PWM.

The above individual steps are described as sub-blocks in Fig. 5.6. Phase currents are measured by utilizing Hall sensor or shunt resistor. Since the phase current sum is equal to zero, it is normal to measure only two-phase currents, for example, (i_{as}, i_{bs}). Step 5) and 6) are practically merged into a single step (e.g. space vector modulation). It should be emphasized that the forward ($abc \rightarrow dq$) and reverse ($dq \rightarrow abc$) transformations are indispensable in the field-oriented control, and that a microcontroller performance needs to be high enough to finish all required computation within the current loop bandwidth.

A detailed control block diagram for the rotor field-oriented scheme is shown in Fig. 5.7. The current control part is based on (5.21) and (5.22), and the slip is calculated according to (5.16).

In the rated speed range, the flux level is maintained constant, but it is reduced as the speed increases (field-weakening). The field reference command, λ^{e*}_{ds} is depicted as a flattened mountain shape.

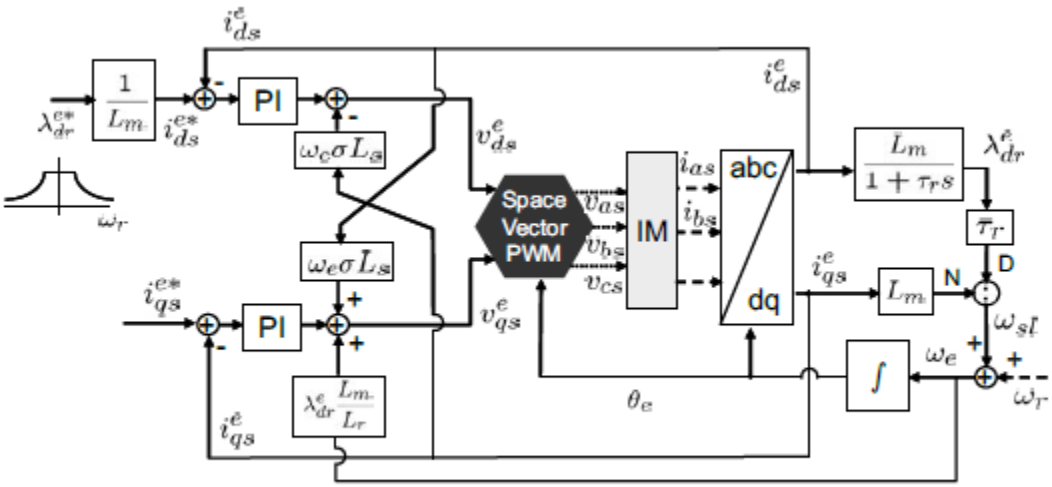

Figure 5.7: Control block based on the rotor field-oriented control scheme.

Appendix D: Simulation Block Diagram

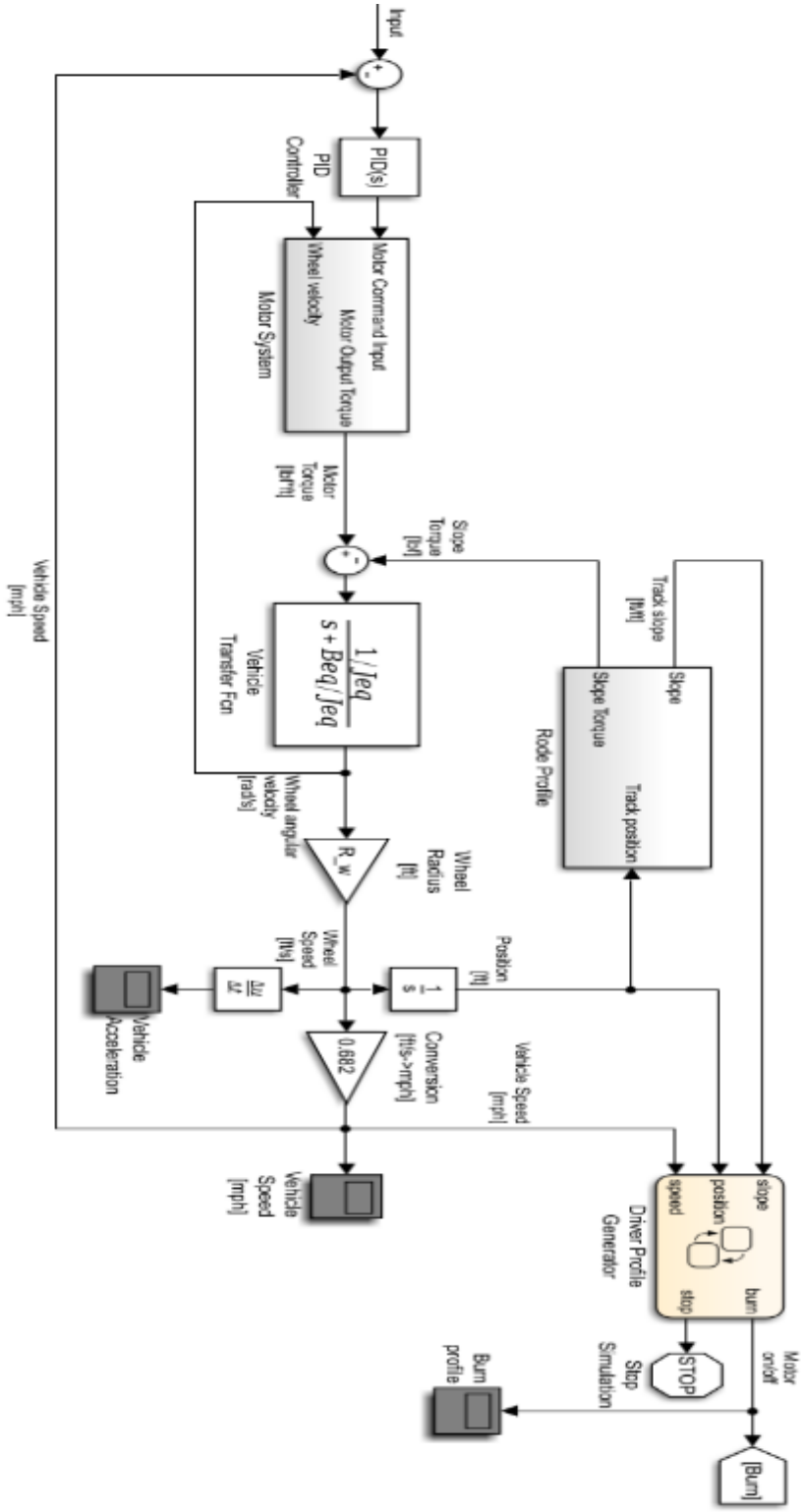

Appendix E: Matlab Script for Simulation and Motor Selection

Table of Contents


```
clear all
clc
close all
```

Supermileage E-car Simulation

March 31, 2018 Chris McLaughlin

Initialize

import road data

```
run = importfile('validrun.xlsx','Sheet1',1,1086);
run_alt = run{:,1};
run_time = run{:,2};
run_dist = run{:,3};
run_slope = run{:,5};

%Create vectors for entire track (6.5 laps)
run_dist = [run_dist; run_dist+1+max(run_dist);...
    run_dist+2+2*max(run_dist);run_dist+3+3*max(run_dist);...
    run_dist+4+4*max(run_dist);run_dist+5+5*max(run_dist);...
    run_dist(1:(length(run_dist)+1)/2,1)+6+6*max(run_dist)];
run_alt = [run_alt; run_alt; run_alt; run_alt; run_alt;...
    run_alt; run_alt(1:ceil(length(run_alt)/2),1)];

%calculate slope of the road
run_slope = [0; diff(run_alt(:))./diff(run_dist(:))];

%Smooth data and plot against original
run_alt2 = smoothdata(run_alt,'loess'); %Smooth altitude
figure
```

```
p1=plot(run_dist,run_alt,'k',run_dist,run_alt2,'b');
legend('Original Data','Smoothed Data')
title('Sonoma Raceway Elevation versus Position')
xlabel('Position [ft]')
ylabel('Elevation [ft]')

dydx =[0; diff(run_alt2(:))./diff(run_dist(:))]; % Smooth Slope
figure
dydx=[smoothdata(dydx,'loess')];
p3=plot(run_dist,run_slope,'k',run_dist,dydx,'b');
legend('Original Data','Smoothed Data')
title('Sonoma Raceway Slope versus Position')
xlabel('Position [ft]')
ylabel('Slope [ft/ft]')
```

Sim Parameters

```
V_Batt = 48; %Maximum Battery Voltage
GRs = 7; %Gear Ratio
D_Wheel = 19.5; %Wheel Diameter [in]
W_t = 220; %Total vehicle weight [lbf]
Beq = 0.065; %Coasting Equivalent viscous damping factor [lbf*ft*s]
% Beq = 0.1;
Beq2 = 0.08; %Power Equivalent viscous damping factor [lbf*ft*s]

R_w = (D_Wheel/2)/12; %Wheel radius [ft]
g = 32.2;
Jeq = (W_t/g)*R_w^2; %Equivalent inertia of the vehicle [lbf*ft*s^2]
```

Motor Selection Calculations

operating point

```
Td = 45; %desired stall torque
r = 19.5/2/12; %wheel radius [in]
GR = 7; %Desired gear ratio
mph = 20; %desired speed [mph]
ft_s = mph/.682;
rad_s = ft_s/r;
op_rpm = rad_s*60/(2*pi)*GR
max_rpm = op_rpm*7/6
```

Motor Selection for Slope

clear all clc

```
mph_slope = 7; %Max speed up a slope
slope_point = .7; %max power to max efficiency 0.5 to 0.86
slope = 6; %road slope [%grade]
GR = 5; %Gear Ratio
```

```
%Vehicle parameters
W = 220; %Vehicle weight [lbf]

T_slope = W*r*sin(atan(slope/100))/0.73756/GR %Motor torque for
 constant speed [N*m]
ft_s = mph_slope/.682;
rad_s = ft_s/r;
rpm_slope = rad_s*60/(2*pi)*GR;
rpm_max = rpm_slope/slope_point
Tstall = rpm_max*T_slope/(rpm_max-rpm_slope)

op_rpm = 6/7*rpm_max;
mph_op = op_rpm*(2*pi)/60*r*.682/GR
```

Motor Selection Flat

clear all clc

```
mph_ss = 20; %Steady state speed of car
ss_point = 0.9; %max power to max efficiency 0.5 to 0.86
GR = 5; %Gear Ratio

%Vehicle parameters
r = (19.5/2)/12; %wheel radius [in]
W = 220; %Vehicle weight [lbf]
b = 0.065; % Viscous Drag coefficient

ft_s = mph_ss/.682;
rad_s = ft_s/r;
rpm_ss = rad_s*60/(2*pi)*GR
rpm_max = rpm_ss/ss_point
T_ss = b*rad_s/GR/.73756
T_stall = rpm_max*T_ss/(rpm_max-rpm_ss)
mph_e = mph_ss/ss_point*6/7

close all;
```

Motor 1 (24 V PMS 080F)

```
Motor1 = "Motor: 24 V PMS 080F";
R = 0.3; % Motor Resistance [Ohm]
L = .1; % Motor inductance [mH];
Kt = 0.064; % Motor Torque constant [N*m/A]
Km = 4.410; % Motor EMF constant [V/kRPM]
M_Volt = 24; % Motor Voltage [V]
Im = 78 ; % Max Current
T_max = 5; % Max Torque

Km = Km/1000;
L = L*10^(-3);
% Approximations
if Kt == 0
    Kt = (200*pi/6)*Km; %Bad Approximation
```

```
end

if R == 0 % Approximate Resistance with Ohms Law at peak current
    R = M_Volt/Im;
end
MotorSim(Motor1);
```

Motor 2 (Heinzmann PMS 066F)

```
Motor2 = "Motor: 48V Heinzmann PMS 066F";
R = 0; % Motor Resistance [Ohm]
L = 0; % Motor inductance [mH];
Kt = 0.111; % Motor Torque constant [N*m/A]
Km = 8.11; % Motor EMF constant [V/kRPM]
M_Volt = 48; % Motor Voltage [V]
Im = 19 ; % Max Current
T_max = 2; % Max Torque

Km = Km/1000;
L = L*10^(-3);
% Approximations
if Kt == 0
    Kt = (200*pi/6)*Km; %Bad Approximation
end

if R == 0 % Approximate Resistance with Ohms Law at peak current
    R = M_Volt/Im;
end
MotorSim(Motor2);
```

Motor 3 (Anaheim Automation BLY34 Series)

```
Motor3 = "Motor: BLY344S-48V-3200";
R = 0.16; % Motor Resistance [Ohm]
L = 0.3; % Motor inductance [mH];
Kt = 0.120; % Motor Torque constant [N*m/A]
Km = 11.5; % Motor EMF constant [V/kRPM]
M_Volt = 48; % Motor Voltage [V]
Im = 55 ; % Max Current [A]
T_max = 6.355; % Max Torque [N*m]

Km = Km/1000;
L = L*10^(-3);
% Approximations
if Kt == 0
    Kt = (200*pi/6)*Km; %Bad Approximation
end

if R == 0 % Approximate Resistance with Ohms Law at peak current
    R = M_Volt/Im;
end
MotorSim(Motor3);
```

Motor 4 (RP34-313V48)

```
Motor4 = "Motor: RP34-313V48";
R = 0.3; % Motor Resistance [Ohm]
L = 1.7; % Motor inductance [mH];
Kt = 0.12993; % Motor Torque constant [N*m/A]
Km = 13.6; % Motor EMF constant [V/kRPM]
M_Volt = 48; % Motor Voltage [V]
Im = 59.6 ; % Max Current [A]
T_max = 0; % Max Torque [N*m]

Km = Km/1000;
L = L*10^(-3);
% Approximations
if Kt == 0
    Kt = (200*pi/6)*Km; %Bad Approximation
end

if R == 0 % Approximate Resistance with Ohms Law at peak current
    R = M_Volt/Im;
end
MotorSim(Motor4);
```

Motor 5 (Anaheim Automation BLY344D Series)

```
Motor3 = "Motor: BLY344D-48V-3200";
R = 0.07; % Motor Resistance [Ohm]
L = 0.1; % Motor inductance [mH];
Kt = 0.118; % Motor Torque constant [N*m/A]
Km = 8.81; % Motor EMF constant [V/kRPM]
M_Volt = 48; % Motor Voltage [V]
Im = 55 ; % Max Current [A]
T_max = 6.355; % Max Torque [N*m]

Km = Km/1000;
L = L*10^(-3);
% Approximations
if Kt == 0
    Kt = (200*pi/6)*Km; %Bad Approximation
end

if R == 0 % Approximate Resistance with Ohms Law at peak current
    R = M_Volt/Im;
end
MotorSim(Motor3);
```

Published with MATLAB® R2018a

Appendix F: Power Loss Model by Anderson and Loewenthal

Power loss model by Anderson and Loewenthal as developed in Design of Spur Gears for Improved Efficiency and Comparison of Spur Gear Efficiency Prediction Methods.

Sliding loss,

$$\overline{P_S} = C_1 f \overline{W}\, \overline{V_S}$$

Rolling loss,

$$\overline{P_R} = C_2 \bar{h}\, \overline{V_T} F \text{ CR}$$

where f, $\overline{V_S}$, $\bar{h}$, and $\overline{V_T}$ are evaluated at a point halfway between the pitch point and the start of engagement along the path of contact. The constants C_1 to C_{14} can be found in table I.

Pinion and gear windage expressions were given as

$$P_{W,p} = C_3\left(1 + 2.3\frac{F}{R_p}\right) n_p^{2.8} R_p^{4.6} (0.028\,\mu + C_4)^{0.2}$$

$$P_{W,g} = C_3\left(1 + 2.3\frac{F}{R_g}\right)\left(\frac{n_p}{m_g}\right)^{2.8} R_g^{4.6} (0.028\,\mu + C_4)^{0.2}$$

Length of path of contact,

$$l_T = 0.5\left\{\left[\left(D_p + \frac{2}{C_5 \mathcal{P}}\right)^2 - (D_p \cos\theta)^2\right]^{1/2} + \left[\left(D_g + \frac{2}{C_5 \mathcal{P}}\right)^2 - (D_g \cos\theta)^2\right]^{1/2} - (D_p + D_g)\sin\theta\right\}$$

Average sliding velocity

$$\overline{V_S} = 0.262\, n_p \frac{1 + m_g}{m_g} l_T$$

Average rolling velocity

$$\overline{V_T} = 0.1047\, n_p \left[D_p \sin\theta - \frac{l_T}{4}\left(\frac{m_g - 1}{m_g}\right)\right]$$

Average normal load,

$$\overline{W} = \frac{T_p}{D_p \cos\theta}$$

Friction coefficient from Benedict and Kelley (ref. 12),

$$f = 0.0127 \log\left(\frac{C_6 \overline{W}}{F\mu \overline{V}_S \overline{V}_T^2}\right)$$

(where f is limited to a minimum of 0.01 and a maximum of 0.2).

Equivalent contact radius,

$$R_{eq} = \frac{\left[D_p(\sin\theta) + \frac{l_T}{2}\right]\left[D_g(\sin\theta) - \frac{l_T}{2}\right]}{2(D_p + D_g)\sin\theta}$$

Central EHD film thickness,

$$\overline{h} = C_7(\overline{V}_T\mu)^{0.67}\overline{W}^{(-0.067)}R_{eq}^{0.464}$$

Contact ratio,

$$\mathrm{CR} = \frac{C_5 l_T \mathcal{P}}{\pi \cos\theta}$$

TABLE I. - CONSTANTS USED IN GEAR POWER LOSS EQUATIONS

Constant	Value for SI unit	Value for U.S. customary unit
C_1	2×10^{-3}	3.03×10^{-4}
C_2	9×10^{4}	1.970
C_3	2.82×10^{-7}	4.05×10^{-13}
C_4	0.019	2.86×10^{-9}
C_5	39.37	1.0
C_6	29.66	45.94
C_7	2.05×10^{-7}	4.34×10^{-3}
C_8	196.9	1.0
C_9	1×10^{-3}	1.515×10^{-4}
C_{10}	1.54×10^{-5}	5.738×10^{-6}
C_{11}	1.0	0.0254
C_{12}	1.43×10^{-3}	1.383×10^{-5}
C_{13}	0.0114	0.180
C_{14}	9.226×10^{8}	1.0

Appendix G: Results Summary Tables from "Effects of Frictional Loss on Bicycle Chain Drive Efficiency"

Table 1 Drive Efficiencies for Different Chain Configurations

	50 RPM 100 W	60 RPM 100 W	70 RPM 100 W	60 RPM 150 W	60 RPM 175 W
52–11	92.5	91.1	88.7	94.6	95.5
52–15	94.7	92.3	90.4	96.2	97.5
52–21	95.2	93.8	92.0	97.4	98.2

Table 2 Chain Drive Efficiencies for Different Drive Rotation Rates and Sprocket Configurations (constant input power 100 W)

	30 RPM	40 RPM	50 RPM	60 RPM	70 RPM	80 RPM	90 RPM
52–11	96.7	95.0	92.8	90.9	89.3	87.5	85.4
52–15	97.8	96.5	94.6	93.0	91.0	89.3	87.2
52–21	-	97.8	95.9	94.4	92.8	91.3	89.8

Table 3 Chain Drive Efficiencies for Different Drive Powers and Sprocket Configurations (constant drive rotation rate 60 RPM)

	50 W	75 W	100 W	125 W	150 W	175 W	200 W
52–11	81.0	87.4	91.0	93.0	94.4	95.3	95.8
52–15	83.2	89.8	93.2	95.1	96.5	97.5	98.0
52–21	85.5	91.1	94.4	96.0	97.2	98.1	98.6

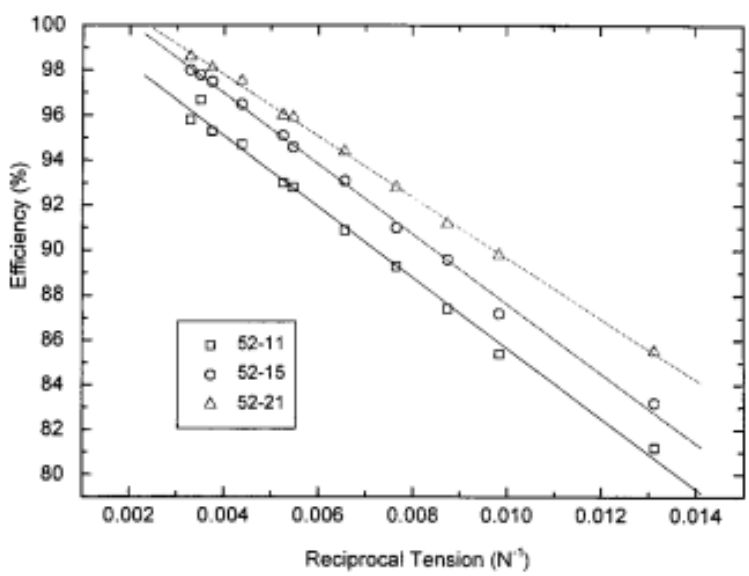

Fig. 4 Variation of chain drive efficiency with the reciprocal of the chain tension. For this graph, chain tension has been calculated using the measured torque values and the radius of the front chain ring.

Table 5 Efficiencies for Different Drive Powers and Sprocket Configurations (input rotation rate 60 RPM)

Sub-Table 5.1: Lubricant 1	50 W	100 W	150 W
52–11	78.1	89.2	92.9
52–15	79.8	90.7	94.3
52–21	83.3	92.3	95.3

Sub-Table 5.2: Lubricant 2	50 W	100 W	150 W
52–11	80.4	89.9	93.5
52–15	83.2	92.5	95.6
52–21	83.0	92.2	95.5

Sub-Table 5.3: Lubricant 3	50 W	100 W	150 W
52–11	-	-	-
52–15	81.2	91.1	94.4
52–21	-	-	-

Appendix H: QFD House of Quality

QFD: House of Quality
Project: SMV E-car
Revision: 1
Date: April 24,2018

Correlations	
Positive	+
Negative	−
No Correlation	

Relationships	
Strong	■
Moderate	□
Weak	▽

Direction of Improvement	
Maximize	▲
Target	◇
Minimize	▼

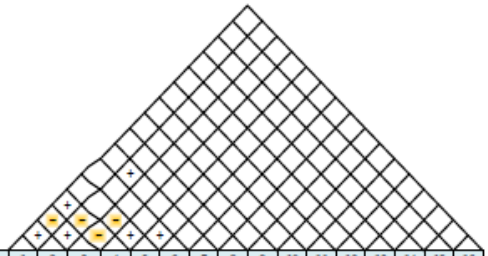

Row #	Weight Chart	Relative Weight	Shell	EE Team	Manufacturing	Driver		Maximum Relationship	WHAT: Customer Requirements (explicit & implicit) / HOW: Engineering Specifications	Energy Use	Efficiency	System Weight	System Cost	Rugged	Reliable	Easy On-Track Maintenance	Speed	Life	Battery Capacity	Our Current Product	Competitor #1: Product Name	Competitor #2: Product Name	Competitor #3: Product Name	Competitor #4: Product Name	0 1 2 3 4 5	Row #
		WHO: Customers							Column #	1	2	3	4	5	6	7	8	9	10	NOW: Current Product Assessment - Customer Requirements						
									Direction of Improvement	◇	▲	◇	▼	▲	▲	◇	◇	▲	◇						
1		6%	0	0	8	8		9	Efficient Drive Train	○	■	■	■	■	■	■	□	■	▽	5						1
2		6%	9	1	2	2		9	Battery and BMS	▽	□	■	□	■	■	■	■	□	■	5						2
3		10%	8	9	8	9		9	Driver Interface	○	■	□	■	■	■	▽	■	▽	▽	5						3
4		6%	0	9	9	8		9	Use of Standard Parts	▽	■	■	■	■	■	■	□	■	▽							4
5		7%	9	0	9	0		9	Fits a rear brake	■	■	▽	■	■	■	▽	▽	▽	▽							5
6		6%	0	7	9	7		9	Easy to assemble and disassemble	▽	■	▽	■	■	■	□	▽	■	▽							6
7		6%	9	9	6	0		9	Purpose built controller	■	■	■	■	▽	■	□	▽	■	□							7
8		3%	0	0	9	0		9	New engine plate	▽	▽	■	□	■	■	▽	▽	■	▽							8
9		3%	0	9	9	0		9	Needs to fit in the old chassis	■	■	▽	■	■	■	■	▽	▽	□							9
10		6%	0	0	8	7		9	Allows easy aiustmentchanges of rear	□	■	▽	■	▽	■	▽	▽	■	▽							10
11		11%	9	8	9	9		9	Follows all Shell Safety regulations	■	□	▽	□	□	□	■	■	□	■							11
12		7%	6	8	0	9		9	Average operating speed 15 mph		□	■	■	■	■	▽	■	■	■							12
13		11%	9	9	9	9		9	Light Weight	▽	■	■	■	■	■	■	□	■	■							13
14		3%	0	7	9	0		9	Can be fabricated/assembled at	▽	■	□	■	■	■	■	▽	■	■							14
15		9%	9	9	3	9		9	Smooth controlable power	▽	■	▽	□	▽	■	▽	■	□	■							15
16		0%						9																		16

HOW MUCH: Target	> 500 mi/kWh	70% system efficiency ^	< 30 lbs	<$4000	220 lb-f	> 95%	< 5 min disassembly/assembly	15 mph average	24 miles	1 kWh and 60V maximum						
Max Relationship	9	9	9	9	9	9	9	9	9	9						
Technical Importance Rating	356	734	487	726	665	833	492									
Relative Weight	8%	17%	11%	17%	15%	19%	11%									
Weight Chart																
Our Product	3	5	5	5	5	5	4									
Competitor #1: *Product Name*																
Competitor #2: *Product Name*																
Competitor #3: *Product Name*																
Competitor #4: *Product Name*																
Current Product Assessment - Engineering Specifications																
Column #	1	2	3	4	5	6	7	8	9	10	11	12	13	14	15	16

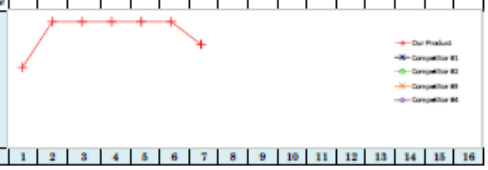

Template Revision: 0.9
Christopher Battles

Appendix I: Preliminary Analyses –Calculation for Wheel Speed

California Polytechnic State University, San Luis Obispo, CA
Date Created: 04/14/2018
Date Modified: 04/17/2019

```
Ve_high = 27; %max velocity of Eventus[mph]
Ve_low = 10; %low speed after coasting [mph]
Ve_avg=15;  %avg velocity of Eventus [mph]
%Velocity of center
V_c_avg=(Ve_avg*5280)/3600; %velocity avg of smv car[ft/s]
V_c_max = (Ve_high*5280)/3600;
V_c_min = (Ve_low*5280)/3600; % mp/hr * 5280 ft/mile *1hr/3600s [ft/s]
D_wheel = 19.5/12; %diameter of tire [ft]

w_wheel_avg = 2*V_c_avg /D_wheel; %w_wheel [rad/s]
w_wheel_avg = w_wheel_avg*60/(2*pi); % [RPM ]
w_wheel_high = 2*V_c_max /D_wheel; %w_wheel [rad/s]
w_wheel_high = w_wheel_high*60/(2*pi); % [RPM ]
w_wheel_low = 2*V_c_min /D_wheel;    %w_wheel [rad/s]
w_wheel_low = w_wheel_low*60/(2*pi); %[RPM ]

display(w_wheel_avg, 'Average RPM')
display(w_wheel_low, 'Minimum RPM')
display(w_wheel_high, 'Maximum RPM')
```

```
Average RPM = 258.5656


Minimum RPM = 172.3770


Maximum RPM = 465.4180
```

Published with MATLAB® R2018b

Appendix J: Weighted Motor Selection Decision Matrix

		Brushed Motor	Brushless DC Motor	PMSM	Hub Motor
Weight	(lightest weight 5)	1	3	4	1
Packaging	(least amount of space 5)	2	3	3	4
Programming and Control	(easiest to program 5)	5	2	1	2
Efficiency	(most efficient 5)	1	3	4	2
Dynamics Response	(most responsive 5)	2	3	5	3
Cost for Position Feedback	(least expensive 5)	3	3	1	3
Sources of Manufracturer	(Easiest to Source 5)	5	4	3	3
	SUM	27	32	34	25

Weight and Programming and control has factor of 2, Efficiency has a factor of 3.

Appendix K: BLY343D Motor Cut Sheet

Model #	Rated Voltage (V)	Rated Speed (RPM)	Rated Torque (oz-in)	Rated Power (W)	Rated Current (A)	Line to Line Resistance (ohms)	Line to Line Inductance (mH)	Torque Constant (oz-in/A)	Back EMF Voltage (V/kRPM)	Rotor Inertia (oz-in-sec²)	Weight (lbs)	"L" Length (in)
BLY343D-48V-3200	48	2700	198.0	440	9.71	0.11	0.17	20.39	10.61	0.022656	6.90	3.86

Dual Shaft:

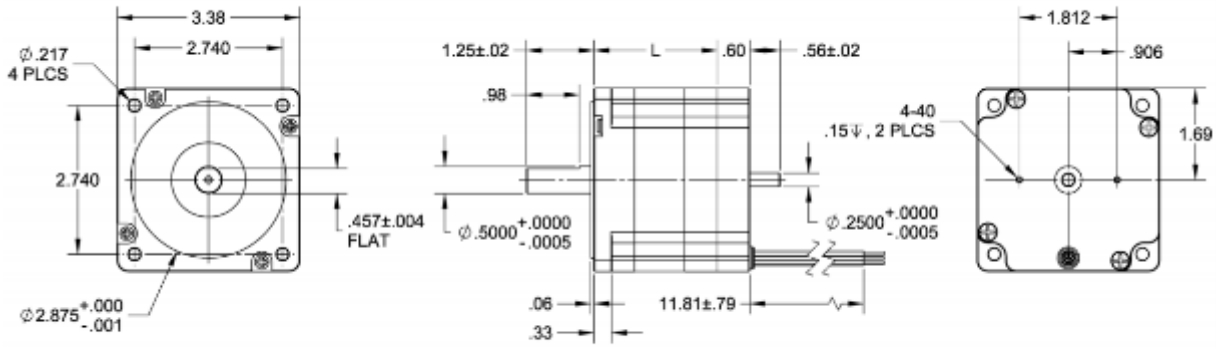

*All units are in (in)

WIRING INFORMATION

Description	Motor Wire Color
Hall Supply	Red
Hall A	Blue
Hall B	Green
Hall C	White
Hall Ground	Black
Phase A	Yellow, Yel/Wht
Phase B	Red, Red/Wht
Phase C	Black, Blk/Wht

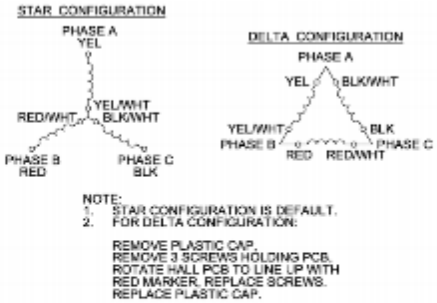

Hall Sensor Specifications
Supply Voltage: 4.5VDC to 28VDC
Current, I_{off}: 10mA max
Current, I_{on}: 11.3mA max
Rated Sinking Current: 20mA
Saturation Voltage: 0.4VDC max @ 25°C
Output Leakage Current: 10µA
Output Switching Time @ 25°C Rise, 10% to 90% 1.5µs Fall, 90% to 10% 1.5µs
Output Type: Open Collector

4985 E. Landon Drive Anaheim, CA 92807 **Tel. (714) 992-6990** Fax. (714) 992-0471 **www.anaheimautomation.com**

Appendix L: MATLAB Script for Bolt Calculations

Plate Force Calculation

Add values but watch for units!!

Known Values

Forces

```
W_veh = 120; % Vehicle weight [lbf] based on 2017 IC competition weight
W_driver = 110; % Driver weight [lbf]
T_Motor_Max = 900*(1/16); % Max motor torque [in.lb] Based on Anaheim Automation BLY peak
Gear_Ratio = 7; % Drivetrain Gear Ratio [GR > 1]
F_Brake = 91; % Braking force [lbf] substitute for decelleration time eventually
R_wheel = 10; % Radius of wheel [in]
V_turn = 15; % Speed at turn [mi/hr]
R_turn = 24; % Turning radius [ft]
```

Dimensions

```
L_Ax = 5; % Distance between wheel dropouts [in]
Lz_Br = 5.64; % Distance between dropout A and Brake disc [in]
Lz_ch = 1.74; % Distance between dropout A and sprocket [in]
R_Sprocket = 10.43; % Large Sprocket radius [in]
L_wheel_z = 3.3; % Distance from wheel center to dropout [in]
% Distances on wheel dropout
```

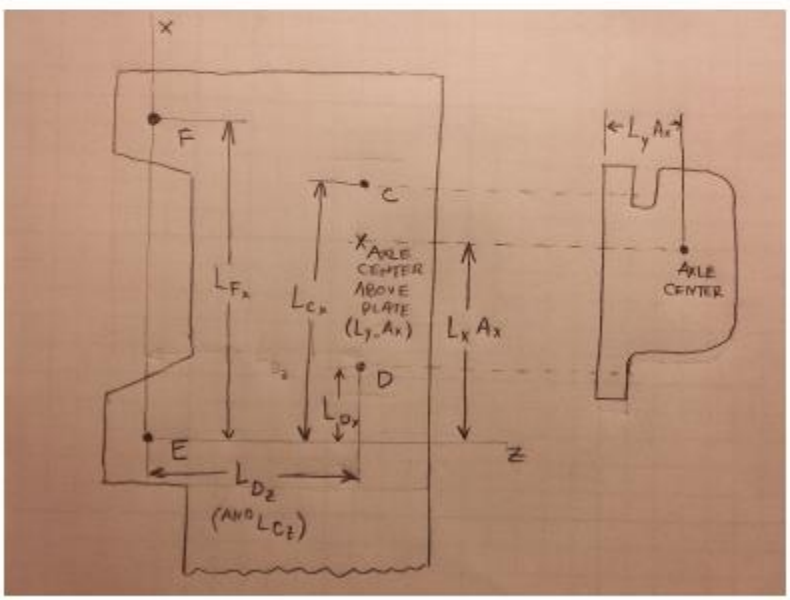


```
Lx_Ax = 0.35; % Distance to center of axle along x axis [in]
Ly_Ax = 1.22 ; % Distance to center of axle along y axis [in]
Lz_Ax = 3.35; % Distance to center of axle along z axis [in]
```

```
% Bolt Patterns
% Dropout
L_Dx = 3.39/2; % Distance from center of dropout to bolt [in]
% Plate mount bracket
L_Mount_x = 1.5; % Distance from center of mount to bolt [in]
L_Mount_z = 1.5;
```

Assumptions

- Screw pattern on mounts and dropouts have the same centerline
- Forces on each bracket are equal in magnitude and direction, otherwise the bracket is elongating

```
% Force from sprocket chain
F_chain = 0; %T_Motor_Max * Gear_Ratio / R_Sprocket % Force of chain on the shaft [lbf]

W_veh_tot = W_veh + W_driver; %Total weight of the vehicle and driver [lbf]
W_rear = W_veh_tot/2; % Weight of the vehicle that rests on the rear axle [lbf]
F_bump = 3*W_rear; % Force on the wheel from hitting a bump [lbf]
m_tot = W_veh_tot/32.2/12; % mass of vehicle [?]
F_turn_z = ((V_turn*17.6)^2*m_tot/(R_turn*12)) % Radial force from turn [lbf]
```

```
F_turn_z = 144.0476
```

```
F_Turn_y = F_turn_z*R_wheel/(L_wheel_z*2) % y-component of force from moment due to turning
```

```
F_Turn_y = 218.2540
```

Intermediate Calculations

Forces on axle from loads

```
F_Rear_y = F_bump + W_rear; % Force on rear wheel
Lz_wh = L_Ax/2; % Wheel is centered between axles
%Forces on axle from loading
F_Axle_x = (F_Brake*Lz_Br - F_chain*Lz_ch)/L_Ax % Force from axle in x direction
```

```
F_Axle_x = 102.6480
```

```
F_Axle_y = (F_Rear_y*Lz_wh + F_turn_z*R_wheel)/L_Ax % Force from axle in y direction
```

```
F_Axle_y = 518.0952
```

```
F_Axle_z = 0 %-F_turn_z
```

```
F_Axle_z = 0
```

Loading transfer to plate at plate mounting point M (Plate to chassis)

```
% Forces at mounting point M [lbf]
F_Mx = -F_Axle_x;
F_My = -F_Axle_y;
F_Mz = -F_Axle_z;

% Moments at mounting point M [in*lbf]
M_Mx = F_Axle_y*Lz_Ax - F_Axle_z*Ly_Ax
```

```
M_Mx = 1.7356e+03
```

```
M_My = F_Axle_z*Lx_Ax - F_Axle_x*Lz_Ax
```

```
M_My = -343.8708
```

```
M_Mz = F_Axle_x*Ly_Ax - F_Axle_y*Lx_Ax
```

```
M_Mz = -56.1028
```

```
% Forces on Bolts
% Bolt Pattern
%  R
%  | \
%  X--M
%  | /
%  F
F_mid_x = F_Mx/3 + M_My/(3*L_Mount_z)
```

```
F_mid_x = -110.6317
```

```
F_mid_y = - M_Mx/L_Mount_z
```

```
F_mid_y = -1.1571e+03
```

```
F_mid_z = F_Mz
```

```
F_mid_z = 0
```

```
F_rear_y = (M_Mz - F_mid_y*L_Mount_x)/(2*L_Mount_x)
```

```
F_rear_y = 559.8388
```

```
F_front_y = F_My - (F_rear_y + F_mid_y)
```

```
F_front_y = 79.1454
```

Loading transfer to plate at dropout point D (Axle to plate)

```
%Forces at point D on plate [lbf]
F_Dx = -F_Axle_x;
F_Dy = -F_Axle_y;
```

```
F_Dz = -F_Axle_z;

% Moments at mounting point D [in*lbf]
M_Dx = - F_Axle_z*Ly_Ax
```

```
M_Dx = 0
```

```
M_Dy = F_Axle_z*Lx_Ax
```

```
M_Dy = 0
```

```
M_Dz = F_Axle_x*Ly_Ax - F_Axle_y*Lx_Ax
```

```
M_Dz = -56.1028
```

Forces on Bolts

```
% F---X---E bolt pattern

F_D_rear_x = -F_Dx/2
```

```
F_D_rear_x = 51.3240
```

```
F_D_rear_y = -(-M_Dz -F_Dy*L_Dx)/(2*L_Dx)
```

```
F_D_rear_y = -275.5971
```

```
F_D_rear_z = -(-M_Dy -F_Dz*L_Dx)/(2*L_Dx)
```

```
F_D_rear_z = 0
```

```
F_D_front_x = F_D_rear_x
```

```
F_D_front_x = 51.3240
```

```
F_D_front_y = -(-F_Dy + F_D_rear_y)
```

```
F_D_front_y = -242.4981
```

```
F_D_front_z = -(-F_Dz + F_D_rear_z)
```

```
F_D_front_z = 0
```

Plot Resulting Forces

```
Force_Ax = [F_Axle_x F_Axle_y F_Axle_z];
Force_Ax = norm(Force_Ax);
line([0 F_Axle_x],[0 F_Axle_y],[0 F_Axle_z],'Color','black')
view(3)
grid on
Flabel = "Axle Force: " + num2str(Force_Ax, 3) + " lbf";
legend(Flabel)
```

```
xlabel('x-component [lbf]')
ylabel('y-component [lbf]')
zlabel('z-component [lbf]')
```

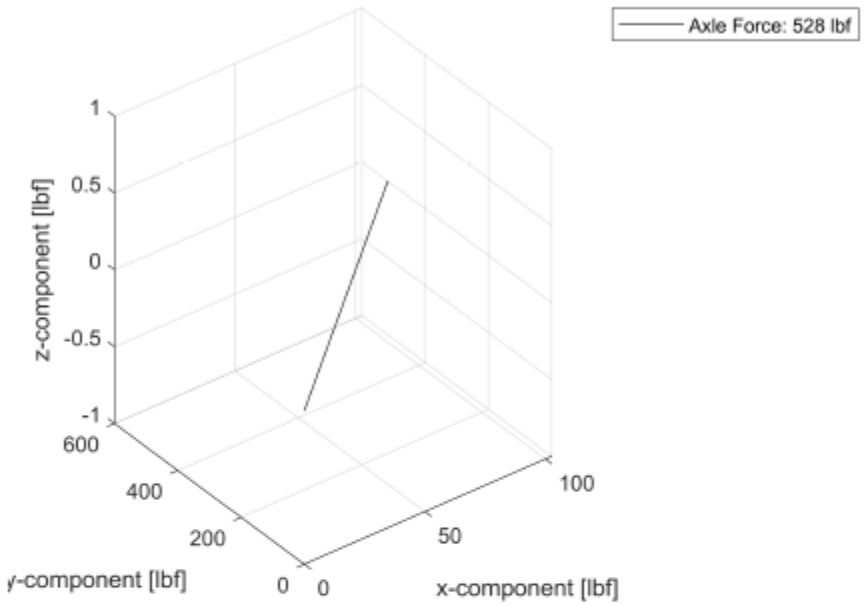

Bolt Forces on plate mount

```
figure
Force_M_Mid = [F_mid_x F_mid_y F_mid_z];
Force_M_Mid = norm(Force_M_Mid);
line([0 F_mid_x],[0 F_mid_y],[0 F_mid_z],'Color','black')

% Force_D_rear = [F_D_rear_x F_D_rear_y F_D_rear_z];
% Force_D_rear = norm(Force_D_rear);
% line([0 F_D_rear_x],[0 F_D_rear_y],[0 F_D_rear_z],'Color','red')
view(3)
grid on
Flabel = "Front Dropout: " + num2str(Force_M_Mid, 4) + " lbf";
% Elabel = "Rear Dropout: " + num2str(Force_D_rear, 3) + "lbf";
legend(Flabel)
xlabel('x-component [lbf]')
ylabel('y-component [lbf]')
zlabel('z-component [lbf]')
```

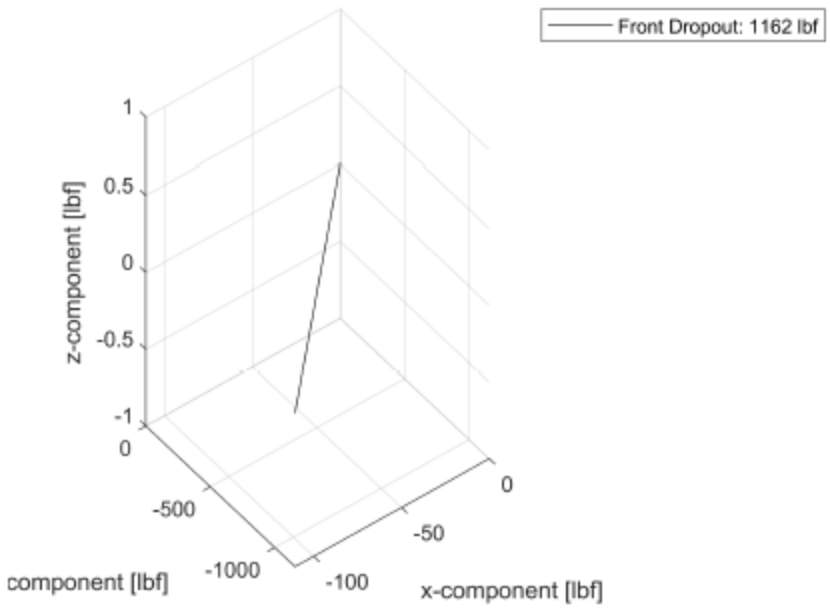

Bolt Forces on Dropout

```
figure
Force_D_Front = [F_D_front_x F_D_front_y F_D_front_z];
Force_D_Front = norm(Force_D_Front);
line([0 F_D_front_x],[0 F_D_front_y],[0 F_D_front_z],'Color','black','LineStyle','--')

Force_D_rear = [F_D_rear_x F_D_rear_y F_D_rear_z];
Force_D_rear = norm(Force_D_rear);
line([0 F_D_rear_x],[0 F_D_rear_y],[0 F_D_rear_z],'Color','red')
view(3)
grid on
Flabel = "Front Dropout: " + num2str(Force_D_Front, 3) + "lbf";
Elabel = "Rear Dropout: " + num2str(Force_D_rear, 3) + "lbf";
legend(Flabel,Elabel)
xlabel('x-component [lbf]')
ylabel('y-component [lbf]')
zlabel('z-component [lbf]')
```

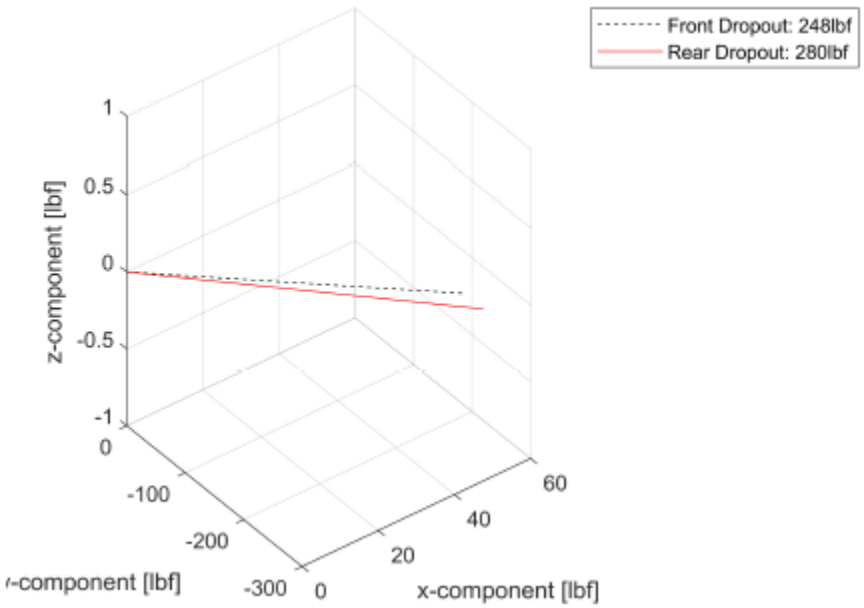
Front Dropout: 248lbf
Rear Dropout: 280lbf
z-component [lbf]
1
0.5
0
-0.5
-1
0
-100
-200
-300
-component [lbf]
0
20
40
60
x-component [lbf]

Aluminum Insert Bolt Calcs (1/4-20)

```
clear
clearvars
```

Insert Dimentions

Based on Shigley's Mechanical Design 10th Edition, Chapter 8 Section 5, Joint-Member Stiffness

```
x=.75+6*.005; % (in) thickness of foam core plus six layers of 5 thou CF
alpha=33; % (degree) upper range of normal alpha for conservative sizing
D=.5; % (in) assumes use of 1/2 in washer
```

The diameter of the frustrum about a bolt. Where x is the thickness of the plate (or 1/2 thickness of total joint if plates are unequal). Alpha ranges from 25 to 33 degrees, and D is the diameter of the washer.

```
D_insert=(x*tand(alpha)+D/2)*2 % (in)
```

```
D_insert = 1.5131
```

Impact Force

The max impact force expected at the wheel drop out bolts is determined to verify that the insert material specifications will be sufficient for loading

Parameters:

```
w_car=220; % (lbf)
S_compressive_G10=35000; % (psi) compressive strength of Gerolite G-10 [source: McMaster]
S_compressive_LE=23800; % (psi) compressive strength of Gerolite LE [source: McMaster]
S_impact_G10= 5.5; % (ft-lbf/in)
S_impact_LE=0.8; % (ft-lbf/in)
F_wheel_load=1157; % (lbf) assumes max wheel load on one bolt
```

Calculations:

Stress from maximum wheel load

```
P_wheel_load=(F_wheel_load/4)/(pi()*(D/2)^2) % (psi) stress per bolt (4 bolts, 2 each side)
```

```
P_wheel_load = 1.4731e+03
```

The impact force from a drop test of 3 ft is found by F=2mah/x where m=mass of car, a=acceleration (gravity), h=drop height, and x=impact distance (crumple zone). Impact pressure assumes all four drop out bolts take the force equally

```
E_impact=w_car*3; % energy of impact (ft-lbf)
F_impact=2*w_car*3/.13 % (lbf) 3 foot drop absorbed by 2 in tire compresson
```

```
F_impact = 1.0154e+04
```

```
P_impact=(F_impact/4)/(pi()*(D/2)^2) % (psi) stress per bolt
```

```
P_impact = 1.2928e+04
```

Safety Factors:

Compression -

```
FS_compression=S_compressive_G10/P_wheel_load % Ratio of rated compressive strength to extimated compression
```

```
FS_compression = 23.7588
```

Impact-

```
FS_impact_G10=(S_impact_G10*.75)/(F_impact/4) % Ratio of rated impact strength to estimated impact per insert
```

```
FS_impact_G10 = 0.0250
```

Chassis Mounting inserts

```
% References
% Aluminum Plates
A_a=.07967; % For aluminim plat from Shigley Table 8-8
B_a=.63816; % For aluminum plate from Shigley Table 8-8
E_a=10.3*10^6; % Elastic Modulus [psi]
v_a=.334; %Poisson Ratio
% Steel Plate
A_s=.78715;
B_s=.62873;
E_s=30.0*10^6; %Elastic Modulus [psi]
v_s=.291; % Possions Ratio
% Gerolite G-10

% General Expression
A_g=.78952;
B_g=.62914;

% Plate Parameters
E_m=10.3*10^6; % Modulus of Elasticity for plate [psi]
t1=.75; % thickness of plates being joined [in]
t2=.75; % thickness of plate being joined [in]


% Bolt Parameters
Thred=20; % Threads threads/inch
D=.25; %nominal diameter [in]
D_t=0 ; % diameter at threads
A_t=.0318; % aread at threads [in^2] found in Shigley Table 8-2
A_d=pi()*(D^2)/4; % Area of unthreaded region [in^2
W_nut=7/16; % thickness of nut [in]
```

```
E_b=29.5*10^6; % Modulus of Elasticity for bolt [psi]
l_t=t1+t2+W_nut; % Length of threaded region engaged [in]
l_d=.75; % Lenght of unthreaded region [in]
N=2; % number of bolts
%Gade 8
Sp=120000; % Proof Strength of bolt [psi]
St=150000; % min Tensile Strenth [psi]
Sy=130000; %min Yield Strenth [psi]

%Loading on Bolt
P=1157; %[lbf]


%Calculations
kb=(A_d*A_t*E_s)/(A_d*l_t+A_t*l_d); % Spring constant of bolt
km=E_m*D*A_a*exp(B_a*D/(t1+t2)); % spring constant of plate if both peices are same material
C=kb/(kb+km)
```

```
C = 0.6331
```

```
Fi=150 % Preload [lbf]
```

```
Fi = 150
```

```
%Load Factor Shigley Eq 8-29
n_L=Sp*A_t-Fi
```

```
n_L = 3666
```

```
% Yield Factor Shigley Eq 8-28
```

```
n_p=Sp*A_t/(C*(P/N)+Fi)
```

```
n_p = 7.3921
```

```
% Load Factor against Separation SHigley Eq 8-30
n_o=Fi/((P/N)*(1-C))
```

```
n_o = 0.7066
```

Motor Mount Bolt Calcs

```
clearvars
clc
clear

% References
% Aluminum Plates
A_a=.07967; % For aluminim plat from Shigley Table 8-8
B_a=.63816; % For aluminum plate from Shigley Table 8-8
E_a=10.3*10^6; % Elastic Modulus [psi]
v_a=.334; %Poisson Ratio
% Steel Plate
A_s=.78715;
B_s=.62873;
E_s=30.0*10^6; %Elastic Modulus [psi]
v_s=.291; % Possions Ratio
% General Expression
A_g=.78952;
B_g=.62914;

% Plate Parameters

t1=.15; % thickness of plates being joined [in]
t2=.75; % thickness of plate being joined [in]
E_G10=18.8*145000; % Youngs Mod. Compressive for plate [psi]

% Bolt Parameters
Thred=20; % Threads threads/inch
D=.25; %nominal diameter [in]
D_t=0 ; % diameter at threads
A_t=.0318; % aread at threads [in^2] found in Shigley Table 8-2
A_d=pi()*(D^2)/4; % Area of unthreaded region [in^2
W_nut=7/16; % thickness of nut [in]
E_b=29.5*10^6; % Modulus of Elasticity for bolt [psi]
l_t=t1+t2+W_nut % Length of threaded region engaged [in]
```

```
l_t = 1.3375
```

```
l_d=0; % Lenght of unthreaded region [in]
N=4; % number of bolts
%Gade 8
Sp=120000; % Proof Strength of bolt [psi]
St=150000; % min Tensile Strenth [psi]
Sy=130000; %min Yield Strenth [psi]

%Loading on Bolt
P=147.2; %[lbf]
```

```
%Calculations
kb=(A_d*A_t*E_s)/(A_d*l_t+A_t*l_d); % Spring constant of bolt
k_a=.5774*pi()*E_a*D/(log((1.155*t1+.5*D)*(2.5*D)/((1.155*t1+2.5*D)*(.5*D))));
k_p=.5774*pi()*E_G10*D/(log((1.155*t2+.5*D)*(2.5*D)/((1.155*t2+2.5*D)*(.5*D))));
km=((1/k_a)+(1/k_p))^-1; % spring constant of plate if both peices are same material
C=kb/(kb+km)
```

```
C = 0.4408
```

```
%Fi=.75*A_t*Sp % Preload [lbf]
Fi=35;%[lbf]
%Load Factor Shigley Eq 8-29
n_L=(Sp*A_t-Fi)/(C*P)
```

```
n_L = 58.2659
```

```
% Yield Factor Shigley Eq 8-28
n_p=Sp*A_t/(C*(P/N)+Fi)
```

```
n_p = 74.4977
```

```
% Load Factor against Separation SHigley Eq 8-30
n_o=Fi/((P/N)*(1-C))
```

```
n_o = 1.7009
```

$T_{stall} = 4.5\ lbf.ft$

BOLT SHEAR
MOTOR MOUNT.

$S.F. = 2$

$T_{chain} = S.F \times T_{stall} = 9\ lbf.ft$

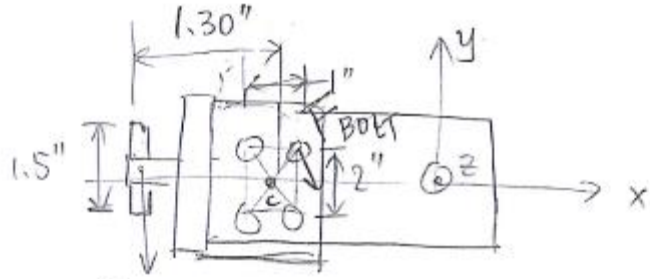

$$F_{CH} = \frac{T_{CHAIN}}{r_{SPROCKET}} = \frac{9\ lbf.ft}{1.5/2 \times \frac{1ft}{12in}}$$

ASSUME ALL 4 BOLTS TAKE EQUAL AMOUNT FORCE.

$F_{CH} = \underline{144\ lbf.}$

$$\Sigma M_C = 4 F_{BOLT} \sqrt{0.5^2 + 1^2} - F_{CH}\ 1.30'' = 0$$

$$F_{BOLT} = \frac{144\ lbf.\ 1.3\ in.}{4(1.118)}$$

$$F_{BOLT} = 41.86\ lbf.$$

1/4-20 BOLT

$$\tau = \frac{F}{A} = \frac{41.86\ lbf}{\pi(\frac{D}{2})^2} = \frac{41.86\ lbf}{\pi(\frac{0.25}{2})^2 in^2}$$

$$\tau_{BR.} = \boxed{852.76\ psi}$$

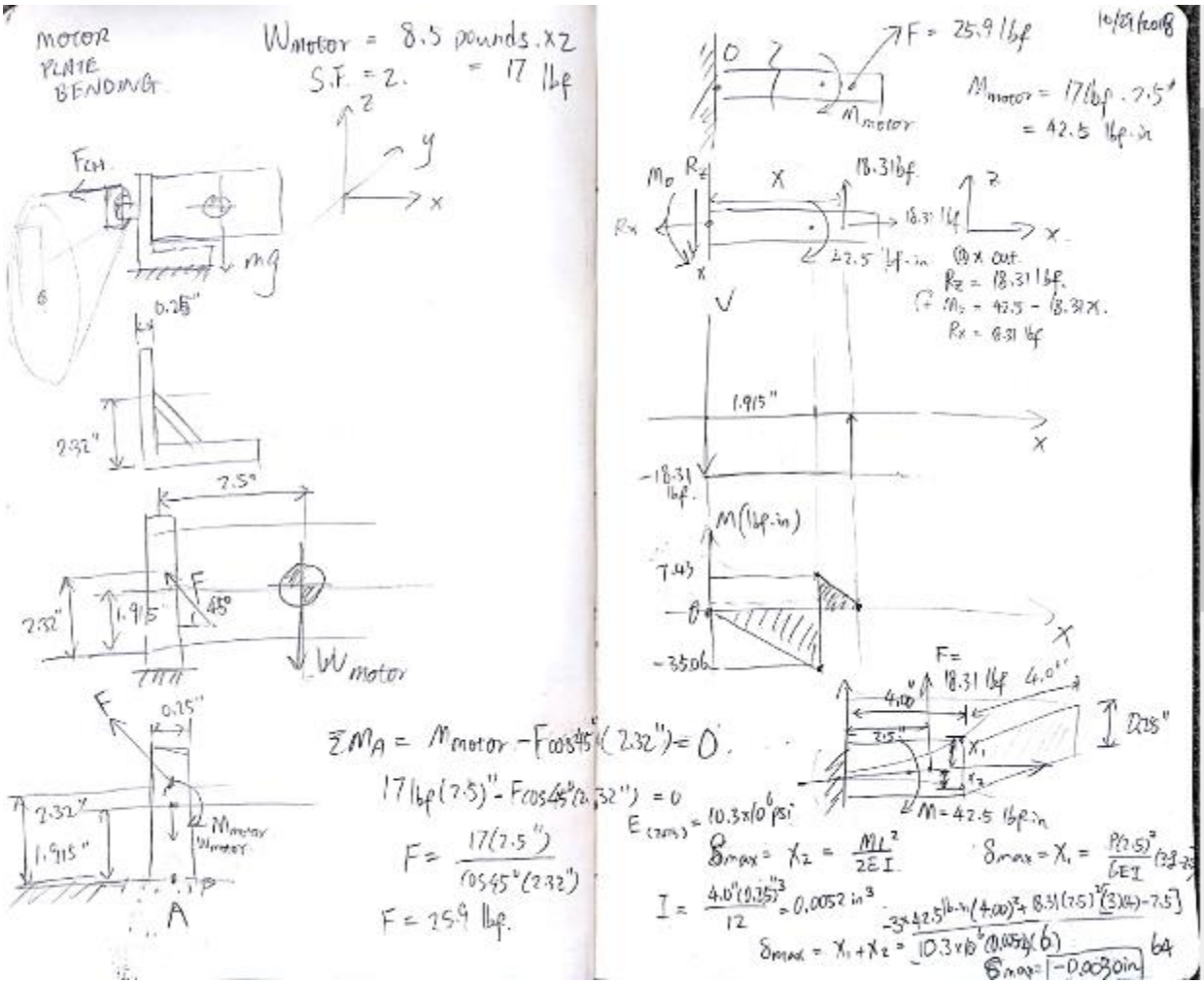

if $t = 0.35"$

$I = \frac{bt^3}{12} = 0.0143\,in^3$

$\delta_{max} = -0.001"$

if $t = 0.45"$

$I = 0.0304\,in^3$

$\delta_{max} = -0.0005"$

Appendix M: Motor Mount Detailed Drawing

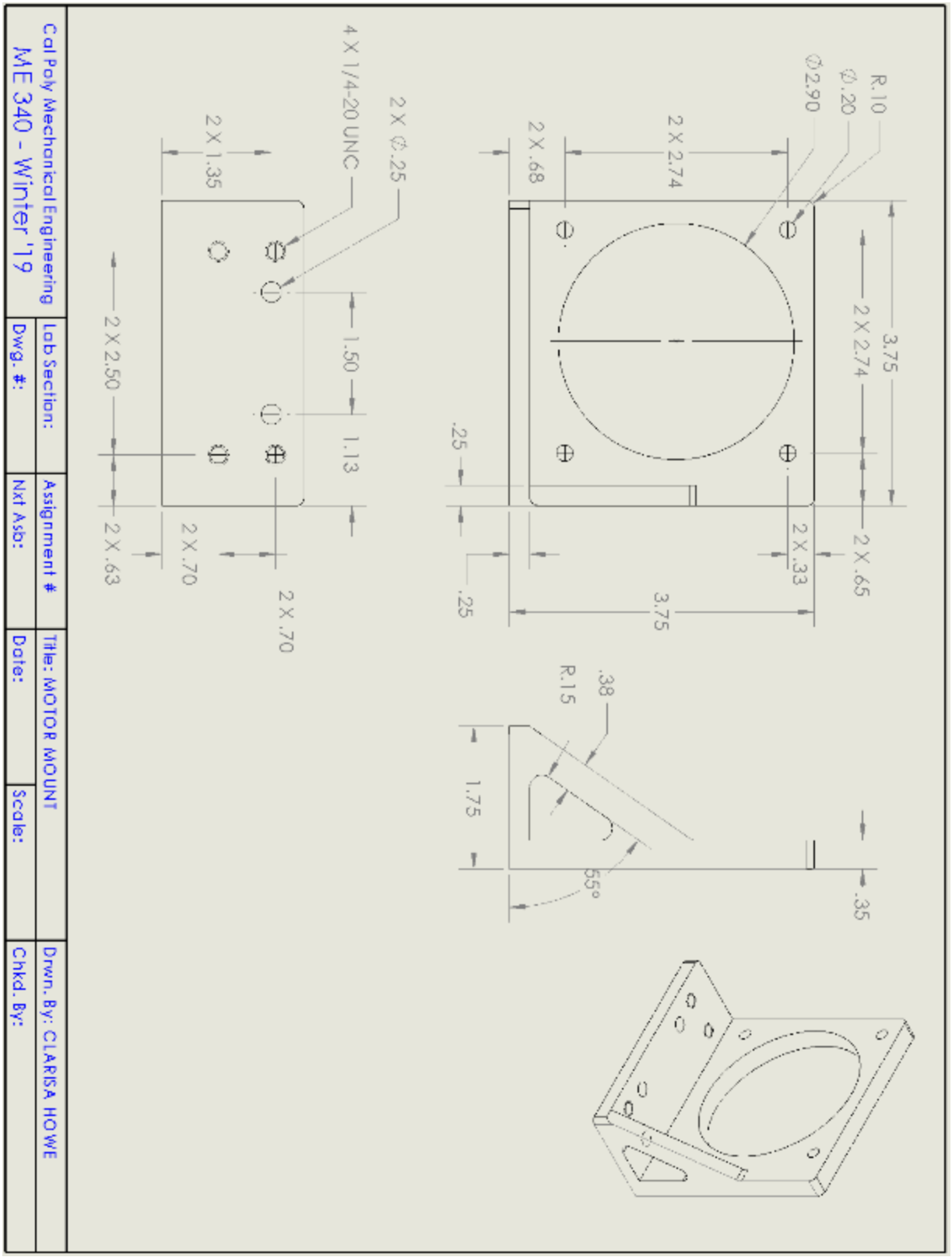

Appendix N: Roller Chain Drive Excel Design Calculations

Spreadsheet created by John Andrew. Parameters for the E-Ventus Supermileage vehicle were entered in to determine that chain sizing and loads.

Step-1 Sprocket Pitch Circle Diameter	Input	
Driver sprocket number of teeth, Ts =	17	teeth
Driver sprocket revolutions per minute, n =	3000	rpm
Driver sprocket teeth / Driven sprocket teeth, r =	7	-
ANSI chain pitch, P =	0.25	**in. from standard chain chart below.**
	Calculations	
Driver sprocket angle, A =	**180 / Ts**	
=	**10.588**	**deg**
Driver sprocket pitch circle diameter, D =	**P / Sin (A)**	
=	**1.361**	**in**
Driven sprocket number of teeth, T_L =	**r * Ts**	
=	**119**	**teeth**
Driven sprocket angle, B =	**180 / T_L**	
=	**1.5126**	**deg**
Driven sprocket pitch circle diameter, D =	**P / Sin (B)**	
=	**9.471**	**in**

Step-2 Minimum Drive to Driven Sprocket Centers	Input	
Small sprocket pitch circle diameter, **d** =	1.361	in
Driver sprocket teeth / Driven sprocket teeth, **r** =	6	-
	Calculations	
Minimum drive to driven sprocket centers, L =	**D + (d / 2)**	
=	**10.151**	**in**

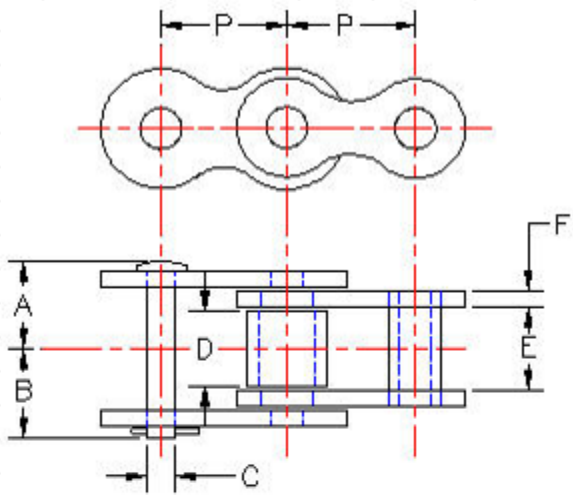

ANSI Standard Roller Chain

Chain No.	Pitch in	Ultimate Strength lbs	Weight lbs/ft	Limiting Speed ft/min	A	B	C	D	E	F
25	1/4	875	0.09	3500	0.155	0.190	0.091	0.130	0.125	0.030
35	3/8	2100	0.21	2800	0.231	0.283	0.141	0.200	0.188	0.050
41	1/2	2000	0.26	2300	0.260	0.370	0.141	0.306	0.250	0.050
40	1/2	3700	0.42	2300	0.314	0.357	0.156	0.313	0.313	0.060
50	5/8	6100	0.68	2000	0.398	0.434	0.200	0.400	0.375	0.080
60	3/4	8500	1.00	1800	0.489	0.574	0.234	0.469	0.500	0.094
80	1	14500	1.73	1500	0.615	0.741	0.312	0.625	0.625	0.125
100	1 1/4	24000	2.50	1300	0.754	0.882	0.375	0.750	0.750	0.156
120	1 1/2	34000	3.69	1200	0.940	1.116	0.438	0.875	1.000	0.187
140	1 3/4	46000	5.00	1100	1.022	1.210	0.500	1.000	1.000	0.219
160	2	58000	6.50	1000	1.228	1.383	0.562	1.250	1.250	0.250
180	2 1/4	76000	9.06	950	1.362	1.718	0.687	1.406	1.406	0.281
200	2 1/2	95000	10.65	900	1.546	1.827	0.781	1.563	1.500	0.312

Step-3 Chain Power Rating

PITCH 5/8 IN AND 3/4 IN ONLY

		Input	
Smaller sprocket number of teeth,	T =	17	-
Smaller sprocket revolutions per minute,	n =	3000	rpm
Chain pitch,	P =	0.250	in
Constant for chain numbers: 40 to 240,	K =	29	-

Chain Constant K

Chain No.	K
40 to 240	17
41	3.4
25 & 35	29

Calculations

Link Plate Fatigue Limited Strength

HP = 1.35*.004 * T^1.08 * n^0.9 * P^(3 - 0.07P)

= 2.48 hp

Roller Bushing Impact Limited Strength

HP = K * P^0.8 * ((100* T) / n)^1.5

= 4.08 hp

Step-4 Chain Service Design Power		
	Input	
Connected Motor power, HP =	1.61	hp
Service factor from table above, F =	1.2	-
	Calculations	
Chain design horse power, HPd =	**HP x F**	
	1.9	**hp**

Step-8 Chain Length		
	Input	
Distance, drive to driven sprocket centers, L =	10.151	in
Chain Pitch, P =	0.250	in
Number of teeth in the large sprocket, T =	119	-
Number of teeth in the small sprocket, t =	17	-
See above input data:	Calculations	
Sprocket center distance in chain pitches, C =	**L / P**	
=	**40.604**	**pitches**
Chain length in number of pitches, NP =	**2C + (T + t) / 2 + 0.1013 x (T – t)^2 / (4C)**	
=	**156**	**pitches**
Chain length in inches, CL =	**P x NP**	
	38.924	**in**

Spreadsheet values were checked with hand calculations:

5/30 <u>SIZING CHAIN</u> : USING ROLLER CHAIN DRIVE EXCEL DESIGN CALCULATIONS BY JOHN ANDREW

$RPM_{@motor} = 3000$ RPM

@ 16 teeth driver and #25 chain sprocket size is $D = 1.28$ in

finding chain speed using $S\ ft/min = \frac{Rev}{min}\left(\frac{\pi D\ ft}{1\ rev}\right)$

$$S = \frac{3000\ rev}{min}\left(\frac{\pi\left(\frac{1.28}{12}\ ft\right)}{rev}\right)$$

$$S = 1005.31\ ft/min$$

Based on minimizing chordal action for $300\ ft/min < S < 1300\ ft/min$ a tooth # of 17 is <u>suggested</u>

This yeilds $D = 1.361$ in

$S = 1068.14\ ft/min$

which is still within the interval

So <u>17 teeth</u> is the minimum suggested tooth count for the driving sprocket.

CONSIDERING POSSIBLE RATIOS FROM 1:4 to 1:7

1:4	$n_d = 17$ teeth $d = 1.361$ in	$n_D = 68$ teeth $D = 5.413$ in	<u>min</u> center distance $L = 6.094$ in
1:5	$n_d = 17$ teeth $d = 1.361$ in	$n_D = 85$ teeth $D = 6.766$ in	$L = 7.446$ in
1:6	$n_d = 17$ teeth $d = 1.361$ in	$n_D = 102$ teeth $D = 8.118$ in	$L = 8.799$ in
1:7	$n_d = 17$ teeth $d = 1.361$ in	$n_D = 119$ teeth $D = 9.471$ in	$L = 10.151$ in

5/30 CHAIN SIZING: Continued

#25 Chain Limiting Ultimate strength is 875 lbs

According to Shigley Table 17-20 based on #25 chain and 3000 $\frac{rev}{min}$ sprocket speed Rated Horse power capacity is 1.84 Hp.

#25 chain 17 tooth sprocket

$H_{p_{rated}} = 1.84\ H_p$

suggested bath or disk lubrication

According to the H_1 and H_2 equations

$$H_1 = 0.004\ N_1^{1.08}\ n_1^{0.9}\ p^{(3-0.07p)} = 1.84\ H_p$$

$$H_2 = \frac{1000\ K_r\ N_1^{1.5}\ p^{0.8}}{n_1^{1.5}} = 4.08\ H_p$$

Which agrees with spreadsheet (removing 1.35 factor from Link plate limited strength H_p)

COMPARING TO 24V Heinzmann PMS 080F electric motor

Rated Power = 0.55 kW

Rated H_p = 0.737 H_p using 1 kW = 1.341 hp

Max Power = 1.2 kW

Max H_p = 1.609 H_p

A #25 chain will suffice for the motor power provided with a safety factor of 0.87

5/30 CHAIN SIZING CONT:

see "#25 and #35 chain sizing" on One drive Drive train folder for all calculations

using a # 35 chain provides a 2.96 factor of safety for the rated and design hp (5.69/1.9)

However weight/ft increases by 233% from 0.09 lb/ft to 0.21 lb/ft.

Rotational kinetic energy for chain increase for 1:7 ratio for #25 and #35 chain comparison

$KE = \frac{1}{2} I \omega^2$

$\omega = 3000 \frac{rev}{min} \left(\frac{2\pi}{rev}\right)\left(\frac{1 min}{60 sec}\right) = 314 \frac{rad}{s}$ for both

$I_{\#25} = \frac{1}{2} m r^2 = \frac{1}{2}\left(0.21 \, lb/ft \left(\frac{56.5}{12} ft\right)\right)\left(\frac{56.5 ft}{12} / 2\pi\right)^2$

$= \frac{1}{2}\left(0.0307 \frac{lbf \, s^2}{ft}\right)(0.749 ft)^2$

$= 0.00862 \, lbf \, s^2 \, ft \, (32.2 \, ft/s^2)$

Appendix O: McMaster Car Product Cut Sheets

Roller Chain Sprocket

for ANSI 25 Chain, 17 Teeth, for 1/2" Shaft Diameter

1 Each

ADD TO ORDER

In stock
$12.19 Each
2737T117

Sprocket Type	Standard
Bore Type	Finished
For Roller Chain Strand Type	Single
For Roller Chain Standard	ANSI
For Roller Chain Trade Size	25
Pitch	1/4"
Number of Teeth	17
For Shaft Diameter	1/2"
Shaft Mount Type	Set Screw
For Shaft Type	Round
ID	1/2"
OD	1.49"
Overall Width	1/2"
Hub Diameter	1 1/32"
Material	Steel
Includes	Two Set Screws
RoHS	Compliant

Mount these sprockets onto your shaft and secure with a set screw—no machining necessary.

Locating Pin

with 1/4" Diameter Round Head

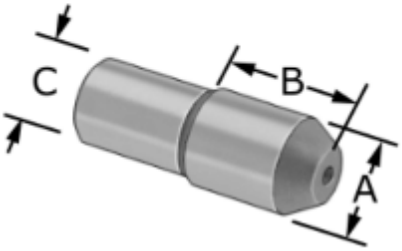

1 Each

ADD TO ORDER

In stock
$2.70 Each
8472A11

System of Measurement	Inch
Head	
Style	Round
Diameter (A)	1/4"
Height (B)	11/32"
End Height	3/32"
Shank Diameter (C)	3/16"
Overall Height	3/4"
Tolerance	
Head Diameter	-0.0008" to -0.0005"
Shank Diameter	0.0001" to 0.0003"
Installation Type	Permanent
Mount Type	Press Fit
Material	Steel
Hardness	Rockwell C60
RoHS	Compliant

Install these pins in a plate or table and mate with holes in a workpiece for precise alignment. Press the shank into a drilled hole for permanent installation.

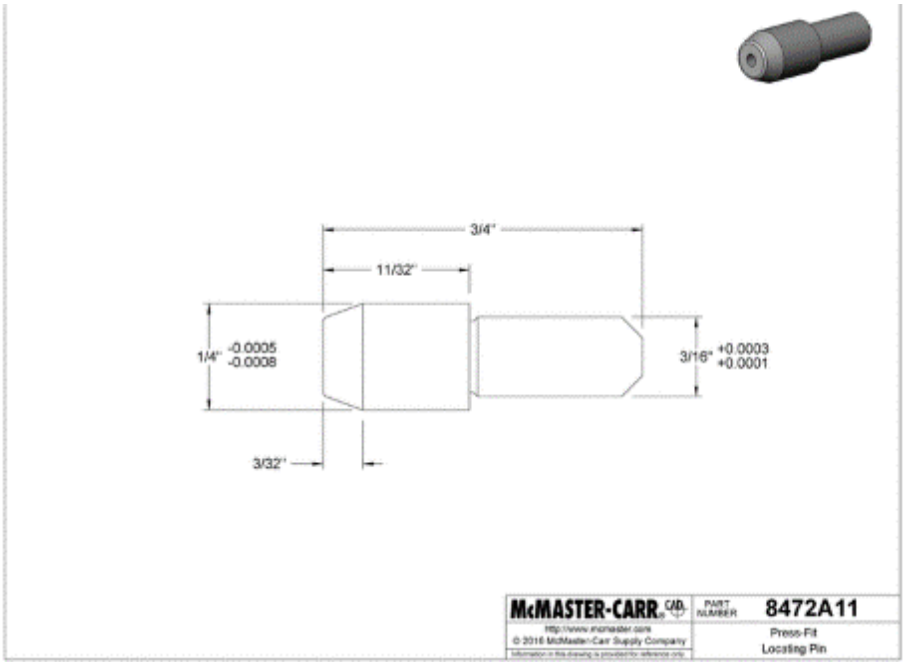

Locating Pin

with 1/4" Diameter Diamond Head

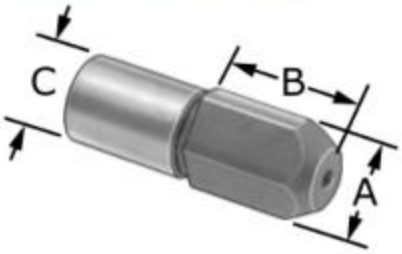

1 Each

ADD TO ORDER

In stock
$4.23 Each
8472A19

System of Measurement	Inch
Head	
Style	Diamond
Diameter (A)	1/4"
Height (B)	11/32"
End Height	3/32"
Shank Diameter (C)	3/16"
Overall Height	3/4"
Tolerance	
Head Diameter	-0.001" to -0.0007"
Shank Diameter	0.0001" to 0.0003"
Installation Type	Permanent
Mount Type	Press Fit
Material	Steel
Hardness	Rockwell C60
RoHS	Compliant

Install these pins in a plate or table and mate with holes in a workpiece for precise alignment. Press the shank into a drilled hole for permanent installation.

Diamond-head pins make less contact with the inside of a hole than round-head pins to reduce sticking and jamming.

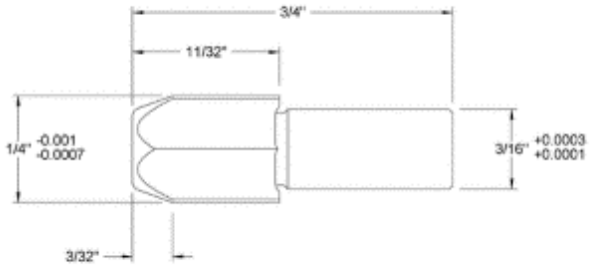

McMASTER-CARR CAD
http://www.mcmaster.com
© 2016 McMaster-Carr Supply Company
Information in this drawing is provided for reference only.

PART NUMBER 8472A19

Press-Fit
Locating Pin

Wing Nut

Zinc-Plated Steel, 1/4"-20 Thread Size, 1/2" Base Diameter

1 Packs of 5

ADD TO ORDER

In stock
$9.87 per pack of 5
90876A560

Material	Zinc-Plated Steel
Thread Size	1/4"-20
Thread Type	UNC
Thread Spacing	Coarse
Thread Fit	Class 2B
Thread Direction	Right Hand
Base Diameter	1/2"
Width	1 3/8"
Height	5/8"
Nut Type	Thumb
Thumb Nut Head Shape	Wing
Wing Nut Profile	Standard
System of Measurement	Inch
RoHS	Compliant

Wings provide more leverage for greater torque while tightening than knurled-head thumb nuts.

Zinc-plated wing nuts are corrosion resistant in wet environment.

High-Strength Steel Threaded Rod

1/4"-20 Thread Size, 3" Long

Each

ADD TO ORDER

In stock
$4.99 Each
90322A650

Material	Steel
Fastener Strength Grade/Class	Grade 8
Thread Size	1/4"-20
Length	3"
Tensile Strength	150,000 psi
Hardness	Rockwell C33
Thread	
Direction	Right Hand
Type	UNC
Spacing	Coarse
Fit (External)	Class 2A
Threading	Fully Threaded
System of Measurement	Inch

Grade 8 steel threaded rods are about 25% stronger than medium-strength steel rods.

Medium-Strength Steel Hex Nut

Grade 5, Black-Oxide, 3/4"-16 Thread Size

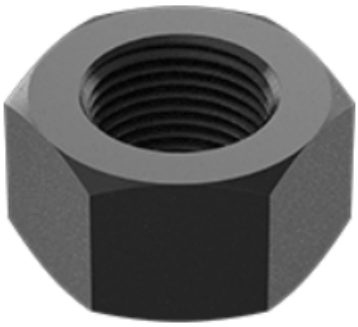

1 Packs of 10

ADD TO ORDER

In stock
$12.72 per pack of 10
95479A129

Material	Black-Oxide Steel
Fastener Strength Grade/Class	Grade 5
Thread Size	3/4"-16
Thread Type	UNF
Thread Spacing	Fine
Thread Fit	Class 2B
Thread Direction	Right Hand
Width	1 1/8"
Height	41/64"
Drive Style	External Hex
Nut Type	Hex
Hex Nut Profile	Standard
System of Measurement	Inch
RoHS	Compliant

These nuts are suitable for fastening most machinery and equipment.

Black-oxide steel nuts have a dark surface color and are mildly corrosion resistant in dry

Easy-to-Machine Garolite Sheet

6" Wide x 6" Long, 3/4" Thick

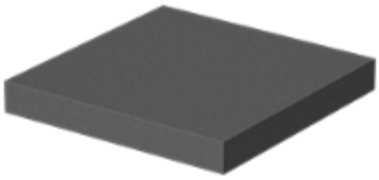

Each

ADD TO ORDER

In stock
$26.60 Each
6842K22

Material	Garolite
Grade	LE
Reinforcement Material	Cotton Fabric
Resin Material	Phenolic
Cross Section Shape	Rectangle
Construction	Solid
Texture	Smooth
Color	Brown
Clarity	Opaque
Thickness	3/4"
Thickness Tolerance	-0.027" to +0.027"
Tolerance Rating	Standard
Width	6"
Width Tolerance	-1" to +1"
Length	6"
Length Tolerance	-1" to +1"
Backing Type	Plain
Hardness	Rockwell M100
Hardness Rating	Extra Hard
For Use Outdoors	No
Min. Temperature	Not Rated
Maximum Temperature	235° F
Impact Strength	0.80 ft.-lbs./in.
Impact Strength Rating	Poor
Tensile Strength	11,700 psi
Tensile Strength Rating	Excellent
Specifications Met	MIL-I-24768/13, UL 94HB
Flatness Tolerance	Not Rated
Density	0.050 lbs./cu. in.
Water Absorption	1.20%
Compressive Strength	23,800 psi
Flexural Strength	15,400 psi
RoHS	Compliant

A fine-weave cotton fabric reinforces a phenolic resin to give these Garolite LE sheets and strips good machinability and wear resistance. They're sometimes referred to as industrial laminate, phenolic, and Bakelite.

Black-Oxide Alloy Steel Socket Head Screw

1/4"-20 | Thread Size | 1/2" Long

Packs of 100

[illegible]

[illegible] per pack of 100

91251A537

Head Type	Socket
Socket Head Profile	Standard
Drive Style	Hex
System of Measurement	Inch
Thread Direction	Right-Hand
Thread Size	1/4-20
Screw Size Decimal Equivalent	[illegible]
Thread Type	UNC
Thread Fit	Class 2A
Length	[illegible]
Threading	Fully Threaded
Thread Rounding	[illegible]
Head	
Diameter	[illegible]
Height	[illegible]
Drive Size	[illegible]
Material	Black-Oxide Alloy Steel
Tensile Strength	170,000 psi
Hardness	Rockwell C37
Specification No.	[illegible]
RoHS	Compliant

[illegible] of 1/2" [illegible] these alloy steel screws are stronger than [illegible] steel screws. Length is measured from [illegible] the head.

Black-oxide [illegible] screws are mildly corrosion resistant in dry environments.

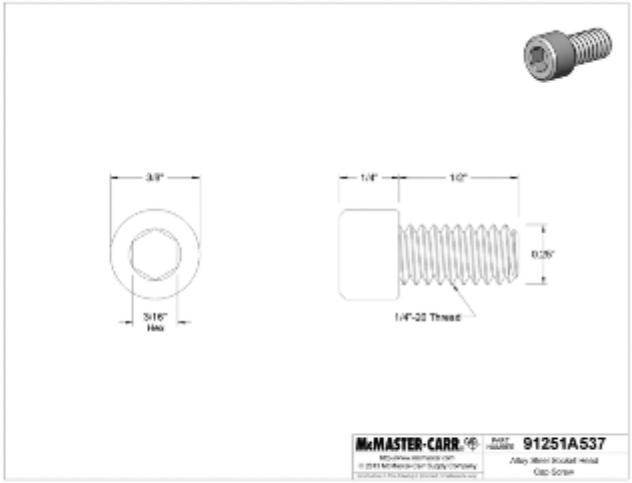

The information in the 3-D model is provided for reference only. Details

Medium-Strength Steel Hex Nut

Grade 5, Zinc-Plated, 1/4"-20 Thread Size

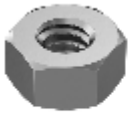

Pack of 100

In Stock

24.40 per pack of 100

Material	[illegible]
Minimum Strength	[illegible]
Coating/Plating	[illegible]
Nominal Size	[illegible]
Thread Type	[illegible]
Thread Series	UNRF
Thread Fit	Class 2B
Thread Direction	Right Hand
Width	[illegible]
Height	[illegible]
Drive Style	[illegible]
Nut Type	Hex
Hex Nut Profile	Standard
System of Measurement	Inch
RoHS	Compliant

[illegible] machinery and equipment.

[illegible] structures.

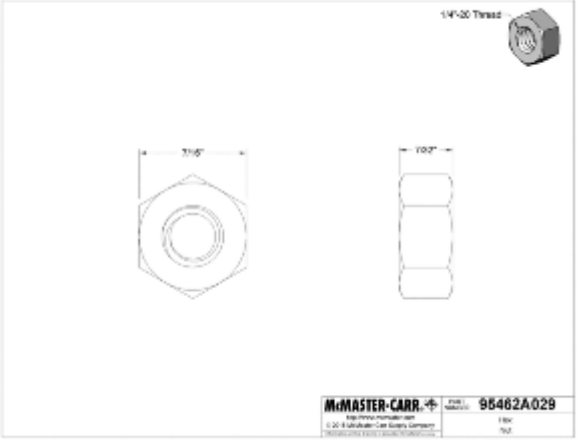

Fine-Thread Alloy Steel Socket Head Screw

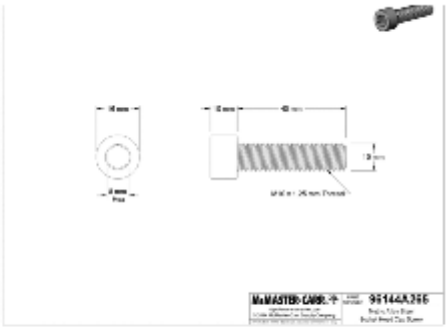

Appendix P: Sprocket Spline Tolerances from Oynx Hub

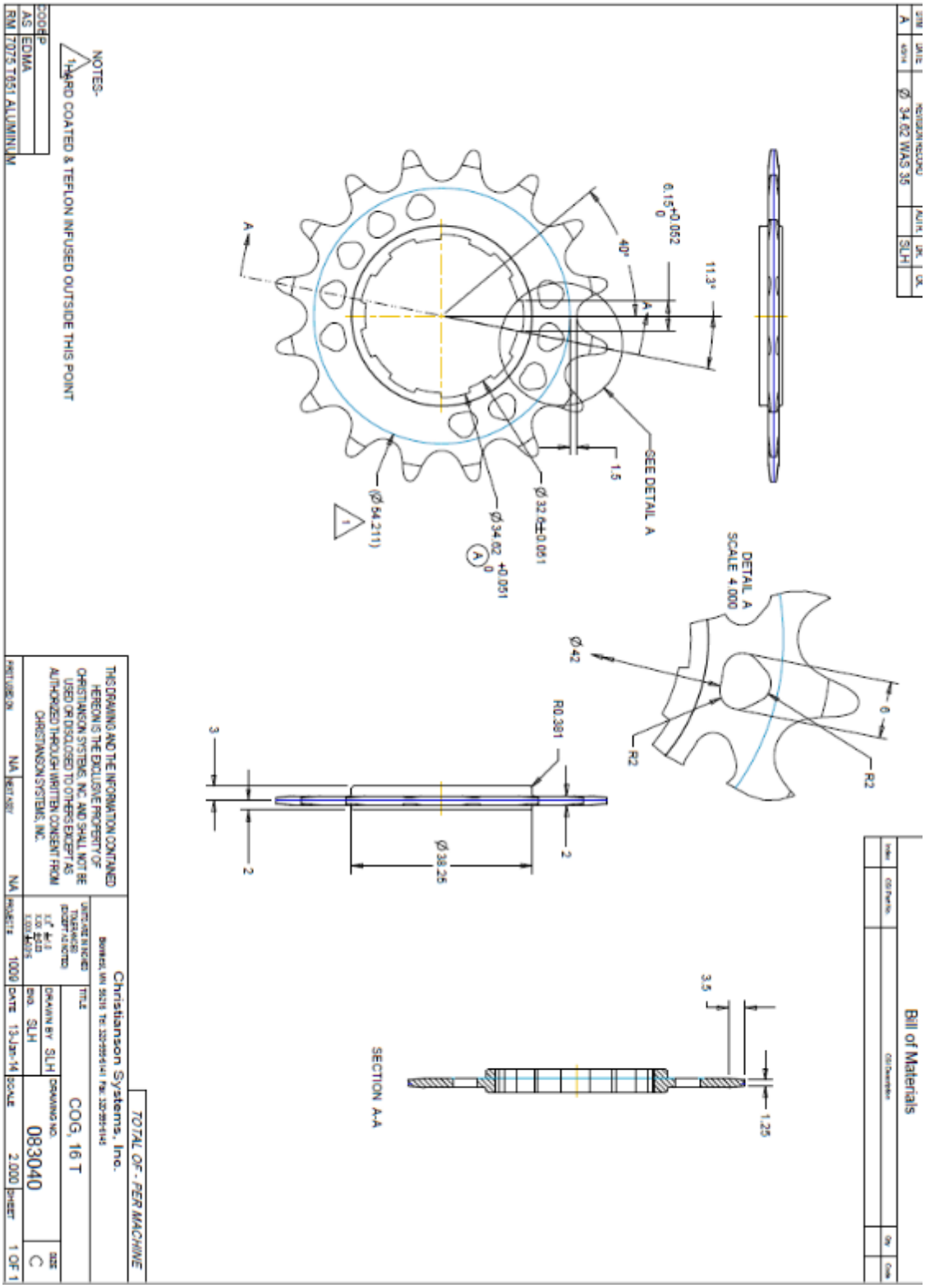

Appendix Q: Large Sprocket Specification Drawing

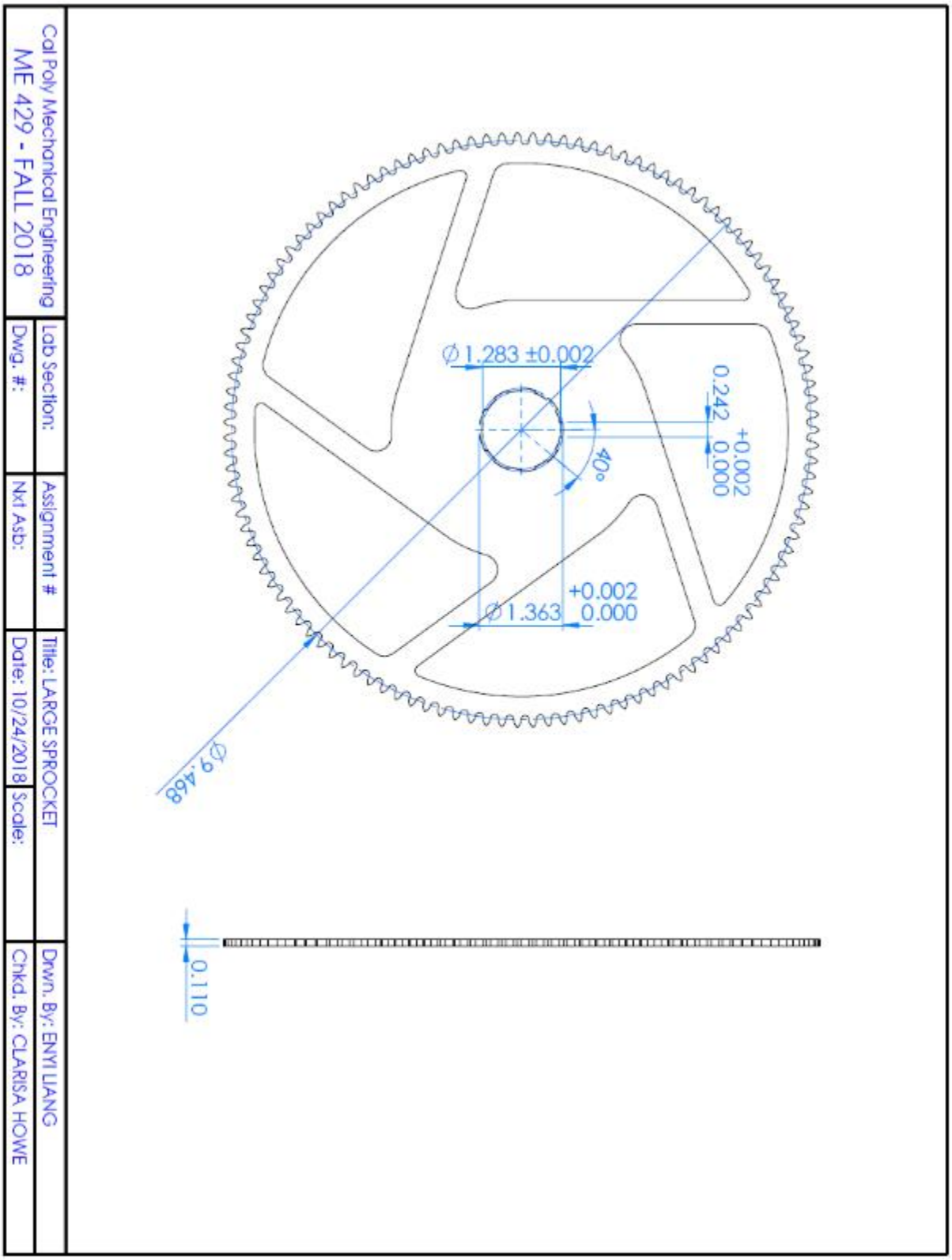

Appendix R: Chain drive center distance calculations with EES

Equations from Shigley's Mechanical Engineering Design, Chapter 17, Tenth Edition. Equations 17-34, 17-35, and 17-36.

Chain Length and Center to Center Calculation:

For a #25 chain with driver sprocket variation from 14 to 19 teeth

$p = 0.25$ *pitch*

$N_{driven} = 135$ *number of teeth on driven sprocket*

$$gr = \frac{N_{driven}}{N_{driver}}$$ *gear ratio*

$$A = \frac{N_{driver} + N_{driven}}{2} - \frac{L}{p}$$

$$L = p \cdot \left[2 \cdot \frac{C}{p} + \frac{N_{driven} + N_{driver}}{2} + \frac{(N_{driven} - N_{driver})^2}{4 \cdot \pi^2 \cdot \frac{C}{p}} \right]$$ *Change length in inches*

$$C = p \cdot \left[\frac{-A + \sqrt{A^2 - 8 \cdot \left[\frac{N_{driven} - N_{driver}}{2 \cdot \pi} \right]^2}}{4} \right]$$ *Center to center distance for sprockets*

Initial Guesses: A=-80, C=15, L=40

Parametric Table: Table 1

	N_{driver}	gr	L [in]	C [in]
Run 1	21	6.429	43.53	11.09
Run 2	19	7.105	43.31	11.07
Run 3	17	7.941	43.1	11.05
Run 4	15	9	42.88	11.03
Run 5	14	9.643	42.77	11.02

Appendix S: Dropout Mount Drawing

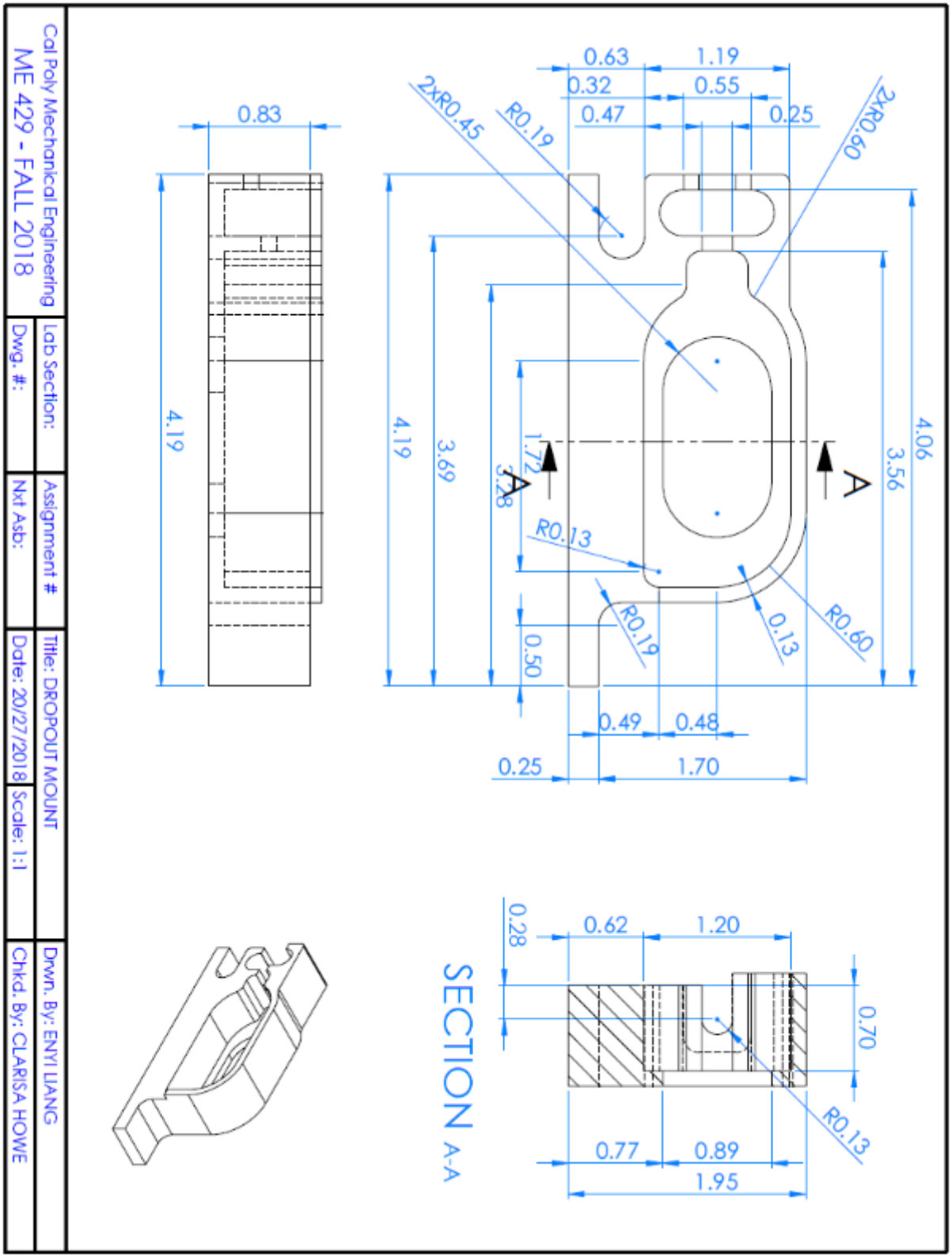

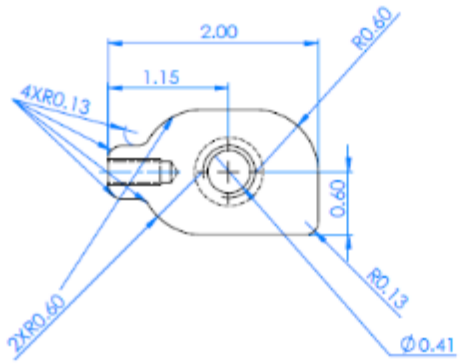

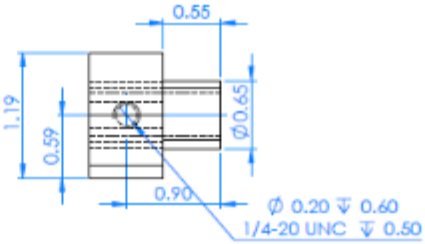

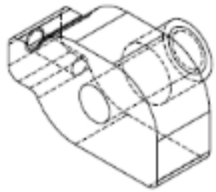

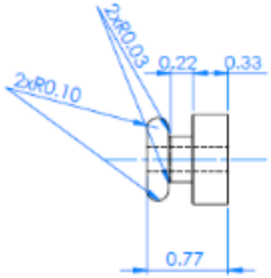

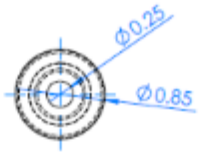

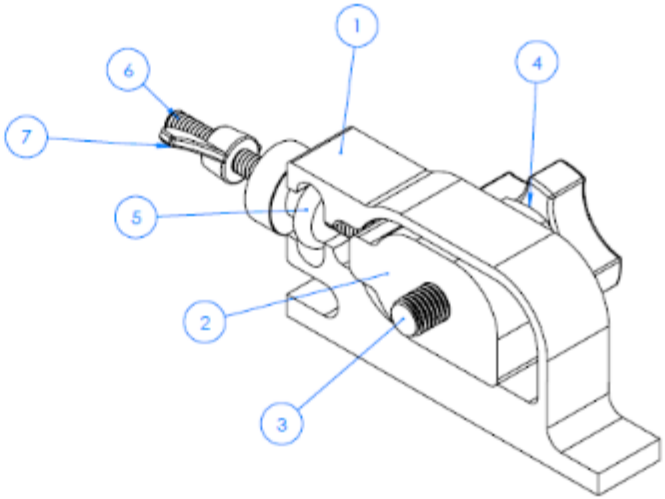

ITEM NO.	PART NUMBER	DESCRIPTION	QTY.
1	Dropout_Mount_Redesign	CNC	1
2	Dropout_Redesign	CNC	1
3	4384K64	M10 Thread Four-Arm Knob	1
4	91935A150	5/8-11 Hex Nut	1
5	Adjustment_Nut_small	CNC	1
6	90322A650	1/4-20 Threaded Rod 3"	1
7	90876A560	1/4-20 Wing Nut	1

Cal Poly Mechanical Engineering ME 429 - Fall 208	Lab Section:	Assignment #	Title: Dropout Mount Assembly		Drwn. By: Enyi Liang
	Dwg. #:	Nxt Asb:	Date: 10/27/2018	Scale:	Chkd. By: Clarisa Howe

Appendix T: Solution Ideas and Decision matrix for Motor Plate

Eight configurations ideas for the motor plate.

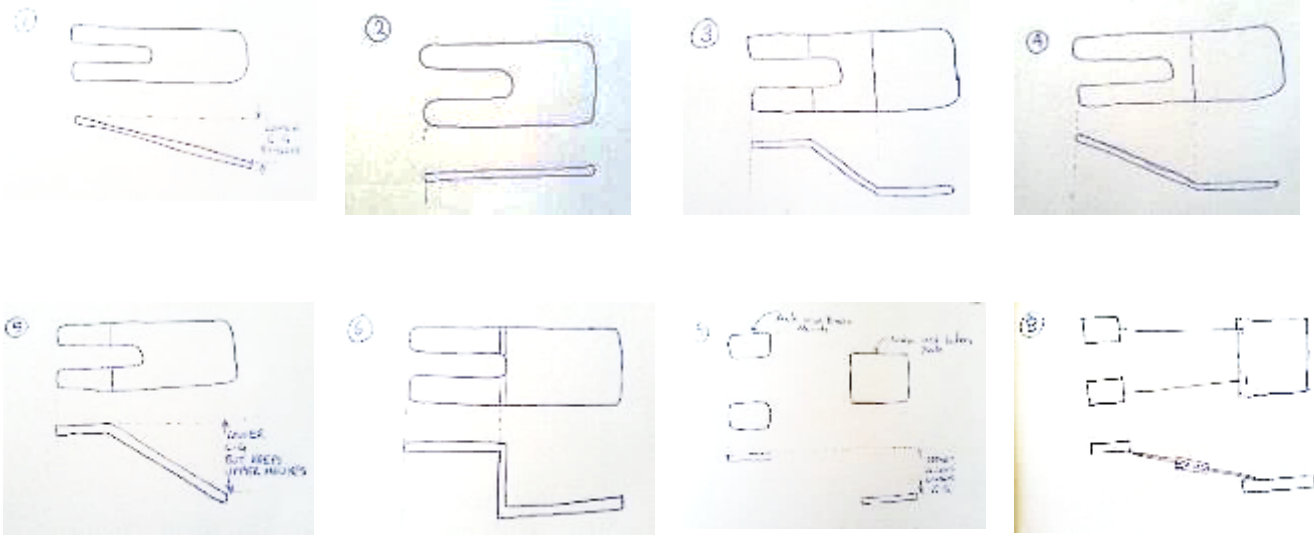

Motor Plate	Lightweight	Manufacturing difficulty	Assmebly Difficulty	Reliability	Allignment	Center of Gravity Height	Structural Strength	Requires Chassis Mount Changes	Ease of use with Dyno (Testing)	Totals
Importance Multiplier (8=Most Important, 1=Least Important)	6	3	5	8	4	7	6	1	2	
Percent Weight	14	7	12	19	10	17	14	2	5	100
(1) Slanted (1 piece)	3	2	2	3	5	4	4	1	4	139
(2) Flat (1 piece)	3	5	4	5	5	1	4	5	5	159
(3) Staggered (1 piece) -_	1	1	3	4	5	4	3	3	4	133
(4) Slanted-Flat (1 piece) _	4	3	3	4	5	5	3	1	4	162
(5) Flat-Slanted (1 piece) -\	4	3	3	3	5	4	3	3	4	149
(6) Drop then flat (1 piece) - |_	3	2	3	2	5	4	2	3	4	126
(7) Flat - offset elevation (2 Piece) - _	5	4	1	4	2	5	1	3	1	133
(8) Flat 2 Piece with connecting rods	5	2	2	4	3	5	3	3	1	148
Notes: Numbers in parenthesis above corresponds to attached pictures	5 = lightweight	5 = Easy to Manufacture	5 = Easy to Assemble	5 = Reliable	5 = Easy to Allign	5= Low CG	5 = Strong	5= no change, 3=Change 1, 1=Change both		Highest Wins

Appendix U: Motor Plate Foam Core Drawing

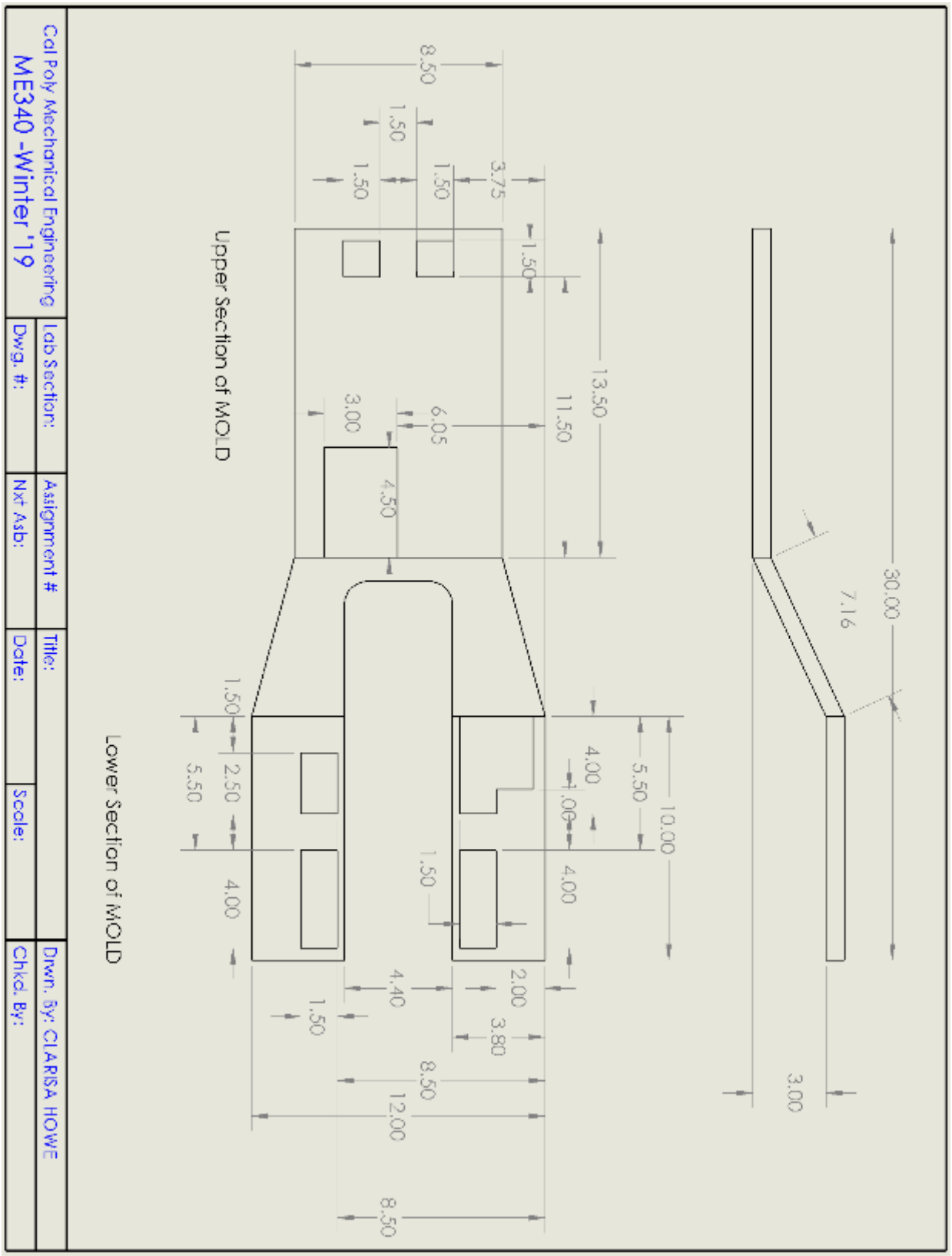

Appendix V: Design Hazard Checklist

DESIGN HAZARD CHECKLIST

Team: Juventas Advisor: Fabijanic Date: May 29, 2018

Y N

✕ ☐ 1. Will the system include hazardous revolving, running, rolling, or mixing actions?

☐ ✕ 2. Will the system include hazardous reciprocating, shearing, punching, pressing, squeezing, drawing, or cutting actions?

✕ ☐ 3. Will any part of the design undergo high accelerations/decelerations?

✕ ☐ 4. Will the system have any large (>5 kg) moving masses or large (>250 N) forces?

☐ ✕ 5. Could the system produce a projectile?

☐ ✕ 6. Could the system fall (due to gravity), creating injury?

☐ ✕ 7. Will a user be exposed to overhanging weights as part of the design?

☐ ✕ 8. Will the system have any burrs, sharp edges, shear points, or pinch points?

☐ ✕ 9. Will any part of the electrical systems not be grounded?

✕ ☐ 10. Will there be any large batteries (over 30 V)?

☐ ✕ 11. Will there be any exposed electrical connections in the system (over 40 V)?

☐ ✕ 12. Will there be any stored energy in the system such as flywheels, hanging weights or pressurized fluids/gases?

☐ ✕ 13. Will there be any explosive or flammable liquids, gases, or small particle fuel as part of the system?

☐ ✕ 14. Will the user be required to exert any abnormal effort or experience any abnormal physical posture during the use of the design?

☐ ✕ 15. Will there be any materials known to be hazardous to humans involved in either the design or its manufacturing?

☐ ✕ 16. Could the system generate high levels (>90 dBA) of noise?

☐ ✕ 17. Will the device/system be exposed to extreme environmental conditions such as fog, humidity, or cold/high temperatures, during normal use?

✕ ☐ 18. Is it possible for the system to be used in an unsafe manner?

✕ ☐ 19. For powered systems, is there an emergency stop button?

☐ ✕ 20. Will there be any other potential hazards not listed above? If yes, please explain on reverse.

For any “Y” responses, add (1) a complete description, (2) a list of corrective actions to be taken, and (3) date to be completed on the reverse side.

Description of Hazard	Planned Corrective Action	Planned Date	Actual Date
There will be sprockets and chains running while vehicle is on.	Chain guard is implemented to prevent hands or other things to be caught in the drivetrain while working around it.	October 2018	March 2019
The wheel will undergo fast acceleration and deacceleration.	Brakes have been installed in the rear wheel to assure timely and safe stops.	October 2018	March 2019
The vehicle itself will be a large moving mass.	All the components are secured inside the vehicle in case of a collision.	October 2018	March 2019
The battery being used is 48V.	An appropriate battery management system is in place as well as a 15 amp circuit breaker at the battery. A firewall between the driver and rear compartment provides protection from exposure to the battery in case of malfunction.	December 2018	March 2019
The system can be used in an unsafe manner depending on the driver.	Drivers will be trained to operate the vehicle safely.	February 2019	March 2019
There will be an emergency stop button located on the top of the vehicle.	A button on top of the vehicle will be installed in case the vehicle malfunctions and needs to be stopped.	October 2018	March 2019

Appendix W: System Schematics

Connections to Launchpad microcontroller and peripherals:

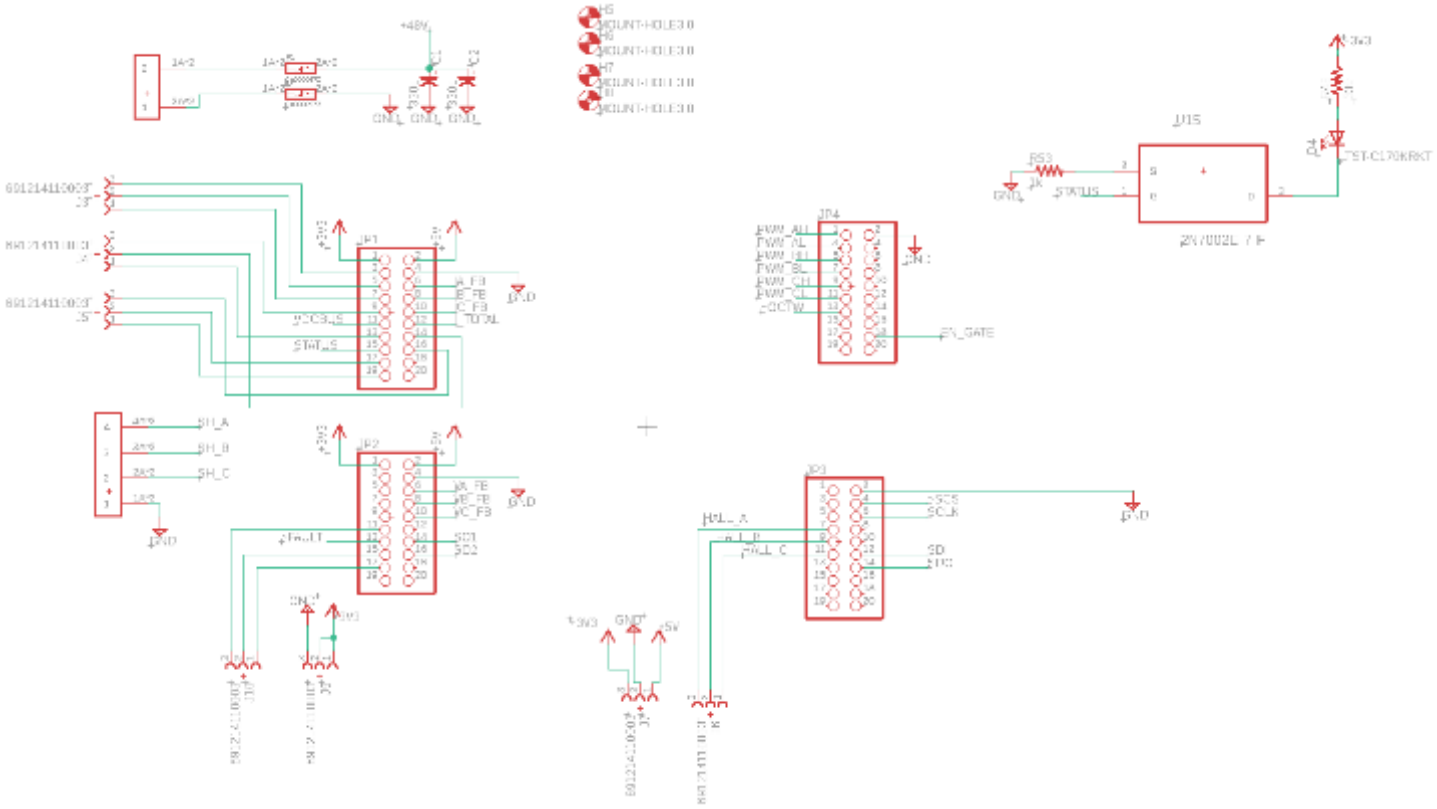

DRV8301 Connections (Note: The GH and GL pins go to the high and low side MOSFETS)

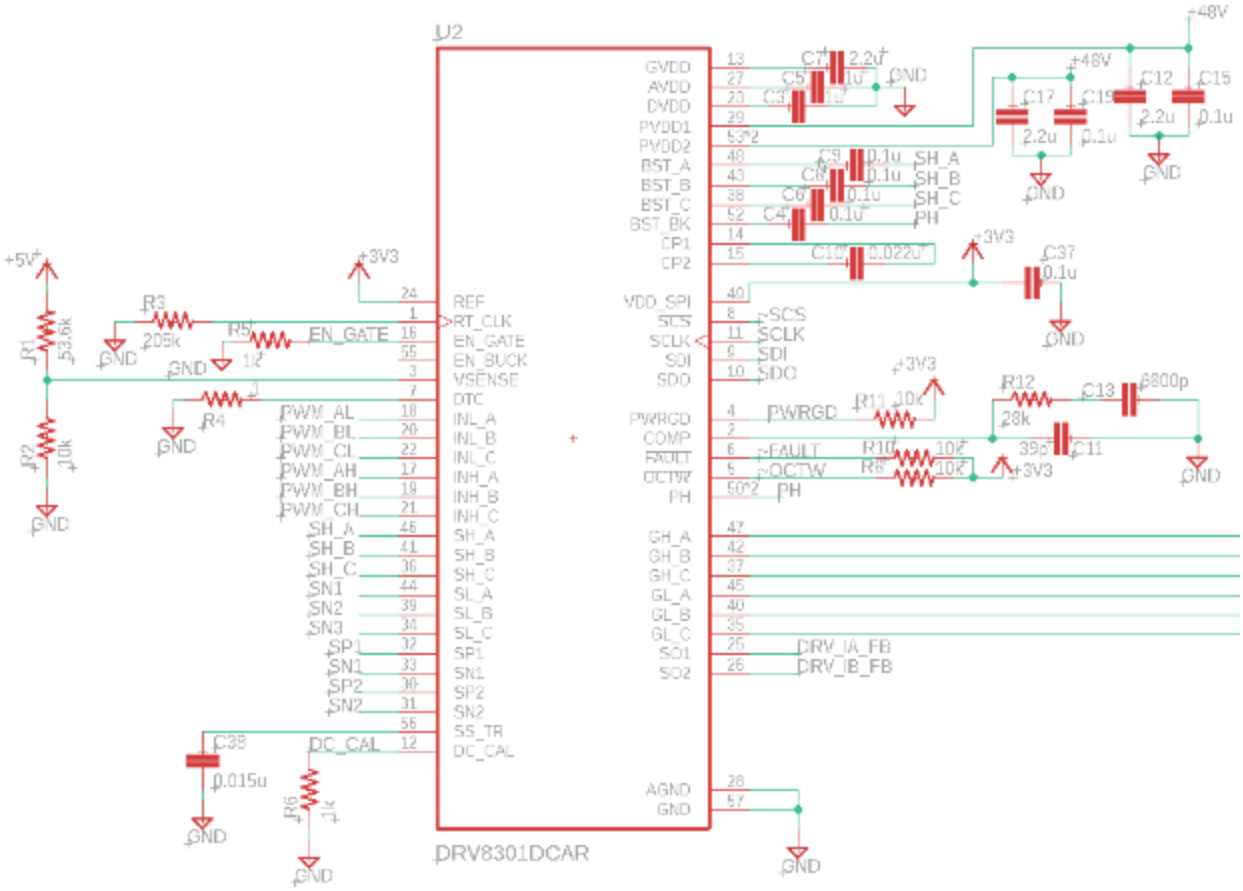

High and Low Side MOSFETs with Voltage Sensors

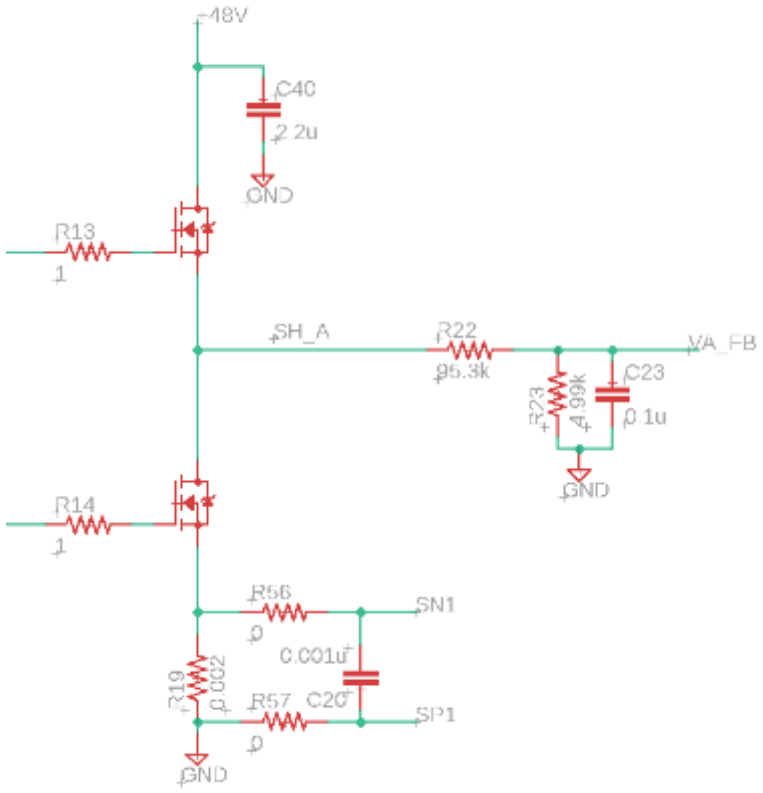

Voltage Reference Circuit:

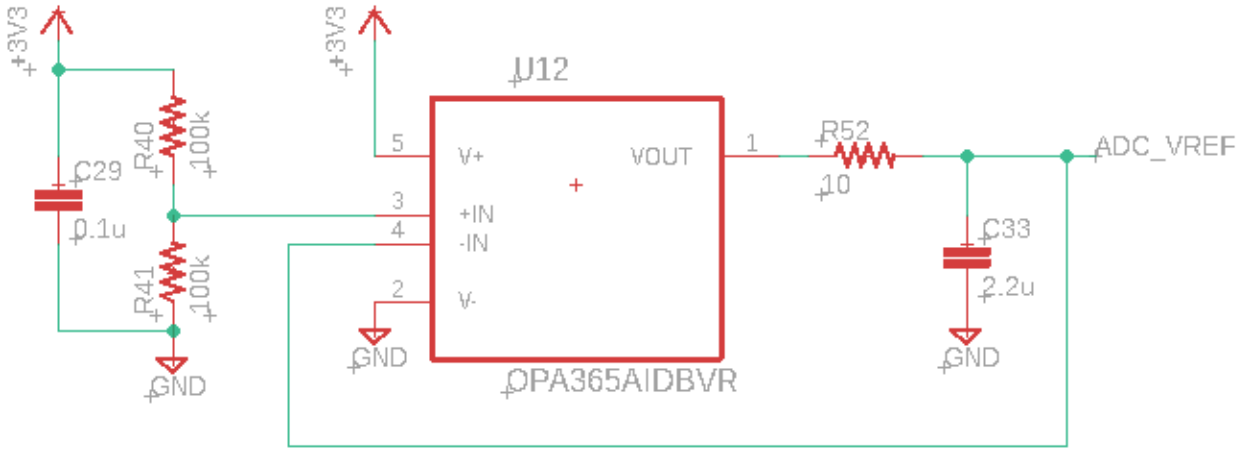

External Current Sensing Circuits (Note: replicated three times):

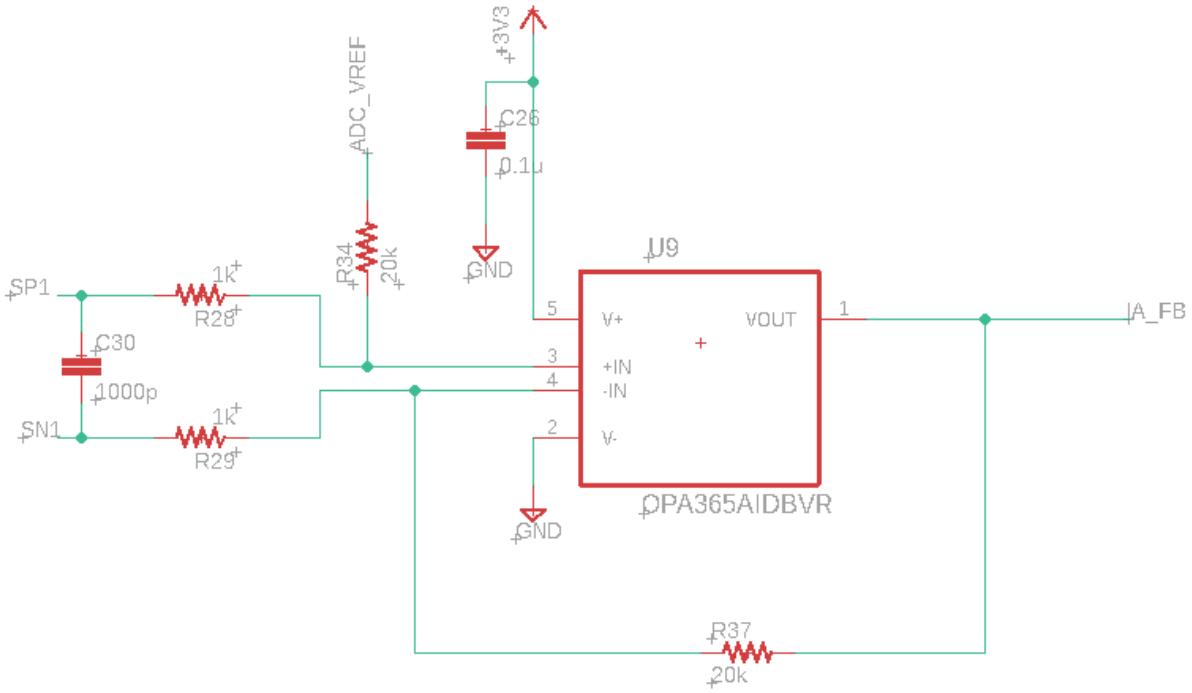

Appendix X. Chassis Dyno Test Procedure

- mount the motor/engine plate to the dyno
- connect DAQ to the pc and open the Labjack LJLogM application
    - Ensure that the data is being written to a file
    - 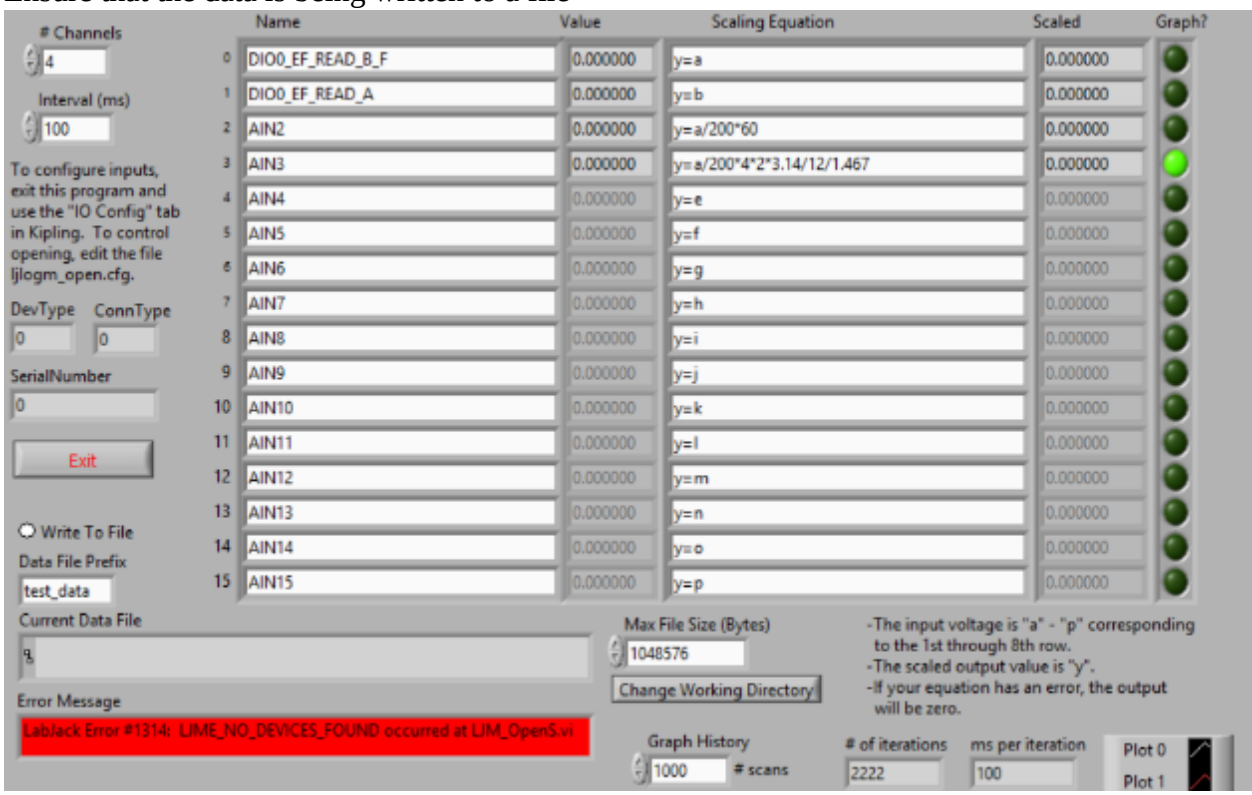

- Run motor and collect data

Appendix Y: Mechanical Bill of Material and Components Budget

	Description	MFG Notes	Vendor	Part Number	QTY	Unit Cost	Total Cost	Notes	Material
Motor									
	BLY344S-48V-3200, rated at 3200, 660W	Double shaft Hall Effect Sensor	Anaheim Automation	BLY344S-48-3200V	1		$ 623.00		
	Rotary Encoder		Anaheim Automation	ENC-AMT11Q	1		$ 36.00		
	Motor Controller		Anaheim Automation	MDC151-050601	1		$ 339.00		
Motor Mount Assembly									
	Motor Mount	Custom Manufactured			1		$ -	Stock supply by SMV	Al 6061-T6
	1/4"-20 x 1-3/4" SHCS		McMaster Carr	90044A124	4	$ 0.19	$ 0.78		Alloy Steel
	1/4"-20 x 1/2 " SHCS		McMaster Carr	91251A537	4	$ 0.11	$ 0.43		Alloy Steel
	1/4"-20 nuts		McMaster Carr	95462A029	4	$ 0.04	$ 0.18		Alloy Steel
	Daimond Head Locating Pin		McMaster Carr	8472A19	1	$ 4.23	$ 4.23		Steel
	Round Head Locating Pin		McMaster Carr	8472A11	1	$ 2.70	$ 2.70		Steel
Motor Plate Assembly									
	Nomex Honeycomb	Custom cut per drawing							
	Carbon Prepreg	Custom cut per drawing						Material supply by SMV	Carbon Fiber
	Mounting Hardware	CNC from 6061 aluminum stock from SMV	McMaster Carr				$ -	Material supply by SMV	Al 6061-T6
	Flim Adheresive	Custom cut per drawing					$ -	Material supply by SMV	
	2lb high temp foam 3/4" thick	Custom cut per drawing	fibre glast	440-C	1	$ 64.95	$ 64.95		
	1/4"-20 x 1-3/4" SHCS		McMaster Carr	90044A124	4	$ 0.19	$ 0.78		Alloy Steel
	1/4"-20 nuts		McMaster Carr	95462A029	4	$ 0.04	$ 0.18		
	Aluminum inserts	CNC from 6061 aluminum stock from SMV							
	Garolite inserts 3/4" thick	Milled		6842K22	1	$ 26.60	$ 26.60		Plastic
	Daimond Head Locating Pin		McMaster Carr	8472A19	4	$ 4.23	$ 16.92		Steel
	Round Head Locating Pin		McMaster Carr	8472A11	4	$ 2.70	$ 10.80		Steel
Rear Drop Out Assembly									
	Rear Drop Out Housing	CNC from 2"x2"x6" 6061 aluminum stock	Cal Poly SMV			---	---	Stock supply by SMV	Al 6061-T6
	Rear Drop Out Slide	CNC from 2"x2"x6" 7075 aluminum stock	Cal Poly SMV			--	---	Stock supply by SMV	Aluminum 7075
	5/8"-11 Hex Nut		McMaster Carr	91935a150	1	$ 11.76	$ 11.76		Steel
	1/4"-20x2 1/2"" SHCS		McMaster Carr	90044A127	4	$ 10.22	$ 40.88		Alloy Steel
	1/4"-20 nuts		McMaster Carr	95462A029	4	$ 0.04	$ 0.18		
	1/4"-20 threaded rod 3''		McMaster Carr	9032A650	2	$ 4.99	$ 9.98		Steel
	1/4"-20 Wing Nut		McMaster Carr	90876a560	1	$ 9.87	$ 9.87		Zinc-plated ste
Rear Hub Assembly									
	Hub	Onyx BMX PRO ISO HG-110/10mm Bolt-on Rear Hub	Onyx	BMX PRO ISO HG-110/10 Bolt on	1	$ 260.00	$ 260.00	discounted from $400	
	Hub Adapter	CNC'd from 6061 aluminum stock					$ -	Stock supply by SMV	Al 6061-T6
	M10 bolts		McMaster Carr	96144A265	2	$ 0.62	$ 1.24		Steel
	M5 bolts		McMaster Carr		1	$ 10.00	$ 10.00		
Sprokect									
	Rear Sprocket	lasercut					$ 200.00	need quote for service	Carbon Steel
	Drive Sprocket, 17 teeth, 1/4" dia		McMasterCarr	273T7117	1	$ 12.19	$ 50.00	need quote for service	
Chain									
	#25 Chain		McMaster Carr	6261K171	1	$ 35.98	$ 35.98		
							$ 1,720.44		

Appendix Z: Electrical Components BOM

Index	Quantity	Part Number	Manufacturer Part Number	Description	Unit Price	Extended Price
1	14	732-2748-ND	691214110003	TERM BLK 3POS SIDE ENT 3.5MM PCB	1.042	$14.59
2	5	2N7002E-FDICT-ND	2N7002E-7-F	MOSFET N-CH 60V 0.25A SOT23-3	0.31	$1.55
3	3	641-1109-1-ND	CDBB2100-G	DIODE SCHOTTKY 100V 2A DO214AA	0.5	$1.50
4	10	732-12189-1-ND	885012207123	CAP CER 15000PF 100V X7R 0805	0.047	$0.47
5	10	732-8076-1-ND	885012207094	CAP CER 0.022UF 50V X7R 0805	0.041	$0.41
6	30	732-12244-1-ND	885012207128	CAP CER 0.1UF 100V X7R 0805	0.082	$2.46
7	10	732-7672-1-ND	885012207078	CAP CER 1UF 25V X7R 0805	0.08	$0.80
8	6	732-7618-1-ND	885012107007	CAP CER 2.2UF 10V X5R 0805	0.15	$0.90
9	5	1276-6687-1-ND	CL21A226KQCLRNC	CAP CER 22UF 6.3V X5R 0805	0.17	$0.85
10	5	311-1106-1-ND	CC0805JRNPO9BN390	CAP CER 39PF 50V C0G/NPO 0805	0.14	$0.70
11	5	490-9954-1-ND	GRM21BC80G476ME15L	CAP CER 47UF 4V X6S 0805	0.48	$2.40
12	10	732-8038-1-ND	885012207038	CAP CER 6800PF 16V X7R 0805	0.04	$0.40
13	10	1276-1810-1-ND	CL32B104KCFNNNE	CAP CER 0.1UF 100V X7R 1210	0.242	$2.42
14	12	478-11403-1-ND	12101C225KAZ2A	CAP CER 2.2UF 100V X7R 1210	0.58	$6.96
15	6	P5584-ND	ECA-1JHG331	CAP ALUM 330UF 20% 63V RADIAL	0.77	$4.62
16	3	513-1141-1-ND	DR74-330-R	FIXED IND 33UH 1.41A 143 MOHM	1.91	$5.73
17	5	160-1415-1-ND	LTST-C170KRKT	LED RED CLEAR SMD	0.36	$1.80
18	10	609-3243-ND	67997-410HLF	CONN HEADER VERT 10POS 2.54MM	0.274	$2.74
19	5	RNCP0805FTD10R0CT-ND	RNCP0805FTD10R0	RES 10 OHM 1% 1/4W 0805	0.1	$0.50
20	10	A126417CT-ND	CRGH0805F10K	RES SMD 10K OHM 1% 1/3W 0805	0.094	$0.94
21	10	A126415CT-ND	CRGH0805F100K	RES SMD 100K OHM 1% 1/3W 0805	0.07	$0.70
22	10	RMCF0805FT16K5CT-ND	RMCF0805FT16K5	RES 16.5K OHM 1% 1/8W 0805	0.027	$0.27

23	10	311-205KCRCT-ND	RC0805FR-07205KL	RES SMD 205K OHM 1% 1/8W 0805	0.043	$0.43
24	10	P20.0KCCT-ND	ERJ-6ENF2002V	RES SMD 20K OHM 1% 1/8W 0805	0.082	$0.82
25	10	311-28.0KCRCT-ND	RC0805FR-0728KL	RES SMD 28K OHM 1% 1/8W 0805	0.042	$0.42
26	25	311-4.99KCRCT-ND	RC0805FR-074K99L	RES SMD 4.99K OHM 1% 1/8W 0805	0.043	$1.08
27	10	RMCF0805FT49K9CT-ND	RMCF0805FT49K9	RES 49.9K OHM 1% 1/8W 0805	0.027	$0.27
28	10	311-330CRCT-ND	RC0805FR-07330RL	RES SMD 330 OHM 1% 1/8W 0805	0.042	$0.42
29	10	311-53.6KCRCT-ND	RC0805FR-0753K6L	RES SMD 53.6K OHM 1% 1/8W 0805	0.043	$0.43
30	10	P95.3KCCT-ND	ERJ-6ENF9532V	RES SMD 95.3K OHM 1% 1/8W 0805	0.081	$0.81
31	6	CSS4527FT2L00CT-ND	CSS4527FT2L00	RES 0.002 OHM 1% 5W 4527	3.07	$18.42
32	6	SI2325DS-T1-E3CT-ND	SI2325DS-T1-E3	MOSFET P-CH 150V 0.53A SOT23-3	1.18	$7.08
33	25	732-12102-1-ND	885012207116	CAP CER 1000PF 100V X7R 0805	0.039	$0.98
34	25	RMCF0805ZT0R00CT-ND	RMCF0805ZT0R00	RES 0 OHM JUMPER 1/8W 0805	0.0152	$0.38
35	25	RNCP0805FTD1R00CT-ND	RNCP0805FTD1R00	RES 1 OHM 1% 1/4W 0805	0.072	$1.80
36	25	RMCF0805FT1K00CT-ND	RMCF0805FT1K00	RES 1K OHM 1% 1/8W 0805	0.027	$0.68
37	2	WM7473-ND	0399100302	TERM BLK 2P SIDE ENT 10.16MM PCB	7.38	$14.76
38	4	36-3544-2-ND	3544-2	FUSE BLOCK BLADE 500V 20A PCB	0.94	$3.76
39	2	WM5966-ND	0399100104	TERM BLK 4P SIDE ENT 10.16MM PCB	11.74	$23.48
40	6	RFD3055LE-ND	RFD3055LE	MOSFET N-CH 60V 11A I-PAK	0.89	$5.34
41	3	Z6234-ND	G2R-1A-T DC48	RELAY GEN PURPOSE SPST 10A 48V	6.69	$20.07
42	4	F1875-ND	0997015.WXN	FUSE AUTO 15A 58VDC BLADE MINI	0.67	$2.68
					Subtotal	**158.99**

Appendix AA: Design Verification and Testing Plan

Cal Poly Supermileage Testing Plan							
Phase Abbreviations: CT (Component Testing) PT (Powertrain Testing) VT (Vehicle Testing)							
Test #	**Specification**	**Description**	**Acceptance Criteria**	**Test Phase**	**Subsystem**	**Planned Start**	**Planned End**
1	Composite Insert Strength	Apply force to insert until failure	SF > 1.25*P_max	CT	Composites	11/8/2018	11/30/2018
2	Motor Mount Perpendicular	Measure perpendicularity of motor mount	Perpendicularity <0.0125”	CT	Manufacturing	1/11/2019	2/1/2019
3	Sprocket Flatness	Test flatness of the sprockets	Variance < 0.0125"	CT	Manufacturing	1/11/2019	2/1/2019
4	Nominal Battery Voltage	Test the charged battery voltage	V_charged ~54V	CT	Electrical	1/11/2019	2/1/2019
5	Motor Property Validation	Compare experimental and specified motor properties	Consider variance from specified values	CT	Electrical	1/11/2019	2/1/2019
6	Motor Control	Actuate BLDC motor with controller	Actuate motor for 30 minutes at nominal power rating	CT	Electrical	1/11/2019	2/1/2019
7	Grade Climb	Ability to maintain speed up a 5% grade	Output torque enough to climb 5% grade	CT	Electrical	1/11/2019	2/1/2019
8	Motor Controller Heat Distribution	Monitor temperature distribution on board during nominal operation	Temperature distribution characterized	CT	Electrical	1/11/2019	2/1/2019

Cal Poly Supermileage Testing Plan							
Phase Abbreviations: CT (Component Testing) PT (Powertrain Testing) VT (Vehicle Testing)							
Test #	**Specification**	**Description**	**Acceptance Criteria**	**Test Phase**	**Subsystem**	**Planned Start**	**Planned End**
9	Powertrain Weight	Calculate weight of vehicle	Weight < 30lbs	PT	Powertrain	2/1/2019	3/1/2019
10	Drivetrain Alignment	Measure sprocket planar alignment on motor plate	Planar Alignment: +- 0.05"	PT	Manufacturing	2/1/2019	3/1/2019
11	Dyno speed test	Approximate speed of vehicle	Average speed > 15 mi/hr	PT	Testing	2/1/2019	3/1/2019
12	Battery Capacity	Measure battery capacity	Max < 1kWh	PT	Electrical	2/1/2019	3/1/2019
13	Dyno Acceleration	Log acceleration data and energy consumption for reaching nominal speed on dyno	Efficient acceleration profile identified	PT	Powertrain	2/1/2019	3/1/2019
14	Drivetrain Damping Coefficient	Estimate drivetrain damping with coast down test	Match experimental profile with simulated	PT	Powertrain	2/1/2019	3/1/2019

Cal Poly Supermileage Testing Plan							
Phase Abbreviations: CT (Component Testing) PT (Powertrain Testing) VT (Vehicle Testing)							
Test #	**Specification**	**Description**	**Acceptance Criteria**	**Test Phase**	**Subsystem**	**Planned Start**	**Planned End**
15	Ruggedness Impact	Mounts can sustain force from dropped vehicle	sustain force >220 lbf	VT	Testing	3/1/2019	3/15/2019
16	Ruggedness Weather	Protect electrical components from water	Check for water on electrical components	VT	Testing	3/1/2019	3/15/2019
17	Rear Hatch Packaging Space	Measure space inside rear hatch	Rear hatch closes	VT	Testing	3/1/2019	3/15/2019
18	Vehicle speed test	Measure speed of vehicle	Average speed > 15 mi/hr Finish track in under 26 minutes	VT	Testing	3/1/2019	3/15/2019
19	Vehicle System Efficiency	Measure miles per kW hour for 6.5 miles	Finish track in under 26 minutes mi/kWh > 250	VT	Testing	3/1/2019	3/15/2019
20	Vehicle Damping Coefficient	Estimate vehicle damping with coast down test	Match experimental profile with simulation	VT	Testing	3/1/2019	3/15/2019

Appendix BB. Sprocket Flatness Results

pc-dmis	PART NAME : 135T_Sprocket		February 06, 2019	09:59
	REV NUMBER :	SER NUMBER :	STATS COUNT : 1	

//	IN	PARL1 - PLN3 TO PLN1				
AX	NOMINAL	+TOL	-TOL	MEAS	DEV	OUTTOL
M	0	0.0200	0	0.0095	0.0095	0.0000

//	IN	PARL2 - PLN4 TO PLN1				
AX	NOMINAL	+TOL	-TOL	MEAS	DEV	OUTTOL
M	0	0.0200	0	0.0075	0.0075	0.0000

//	IN	PARL3 - PLN5 TO PLN1				
AX	NOMINAL	+TOL	-TOL	MEAS	DEV	OUTTOL
M	0	0.0200	0	0.0102	0.0102	0.0000

//	IN	PARL4 - PLN2 TO PLN1				
AX	NOMINAL	+TOL	-TOL	MEAS	DEV	OUTTOL
M	0	0.0200	0	0.0044	0.0044	0.0000

Appendix CC: Sprocket Alignment Results

Data output from MicroVu CMM –

Program: Untitled
Units: in, dec deg

Date: Thu Mar 21 2019 Time: 18:04:17

Feature	Actual	Nominal	Upper	Lower	Dev/Nom	Out/Tol
Plane 135T	[MCS]					
Direction	92.1516	92.1516			0.0000	
Pitch	83.3929	83.3929			0.0000	
Flatness	0.0004					
Plane 15T	[MCS]					
Direction	88.5381	88.5381			0.0000	
Pitch	83.1774	83.1774			0.0000	
Flatness	0.0004					
Parallelism	0.0074			[Plane 135T]		
Angularity				[Plane 135T]		
Distance 135T to 15T	[MCS]					
Distance X	0.0002	0.0002			0.0000	
Distance Y	0.0044	0.0044			0.0000	
Distance XY	0.0044	0.0044			0.0000	
Angle 135 to 15	[MCS]					
Vertex X	2.4817	2.4817			0.0000	
Vertex Y	3.3405	3.3405			0.0000	
Angle	0.4742	0.4742			0.0000	
Form of Fit			1.0000			
Distance 15T to 135T	[MCS]					
Distance X	0.0002	0.0002			0.0000	
Distance Y	0.0073	0.0073			0.0000	
Distance XY	0.0073	0.0073			0.0000	
Angle 15 to 135	[MCS]					
Vertex X	2.4817	2.4817			0.0000	
Vertex Y	3.3405	3.3405			0.0000	
Angle	0.4742	0.4742			0.0000	